# Synthesis and Dielectric Behavior of Various Novel Metal Oxide Decorated Reduced-Graphene Oxide Composites

A thesis

submitted by

# Rama Krishna Jammula

in partial fulfilment of the requirement for the award of the degree of

# **Doctor of Philosophy**

in

# Nano Science and Technology

Under the supervision of

Dr.-Ing. V. V. S. S. Srikanth

# **School of Engineering Sciences and Technology**



**April 2017** 

**DECLARATION** 

I, Rama Krishna Jammula, declare that this thesis work entitled "Synthesis and Dielectric

Behavior of Various Novel Metal Oxide Decorated Reduced-Graphene Oxide

Composites", submitted in partial fulfilment of the requirements for the award of Doctor of

Philosophy (in Nano Science and Technology) in the School of Engineering Sciences and

Technology (SEST), University of Hyderabad is completely my own work except for those

referenced. This work was done under the supervision of Dr.-Ing. V. V. S. S. Srikanth. This

report is a record of the bonafide research work carried out by me and the results incorporated

in it have not been reproduced/copied from any source. This work has not been submitted to

any other University or Institute for the award of any other degree or equivalent.

Rama Krishna Jammula

Registered Number: 11ENPT06

School of Engineering Sciences and Technology

University of Hyderabad



# **CERTIFICATE**

This is to certify that the thesis entitled <u>Synthesis and Dielectric Behavior of Various Novel Metal Oxide Decorated Reduced-Graphene Oxide Composites</u> Submitted by <u>Rama Krishna Jammula</u> bearing registration number <u>11ENPT06</u> (Int. M.Tech./Ph.D.) in partial fulfillment of the requirements for award of Doctor of Philosophy in the School of <u>School of Engineering Sciences and Technology</u> is a bonafide work carried out by him/her under my supervision and guidance.

This thesis is free from plagiarism and has not been submitted previously in part or in full to this or any other University or Institution for award of any degree or diploma.

Parts of this thesis have been:

A. published in the following publications:

- 1. Carbon 78, 374-383 (2014) (ISSN number: 0008-6223), Chapter 4
- 2. Phys. Chem. Chem. Phys. 17, 17237-17245 (2015) (ISSN number: 1463-9076), Chapter 4
- 3. Materials & Design 110, 311-316 (2016) (ISSN number: 0261-3069), Chapter 4

and

B. presented in the following conferences:

- 1. IUMRS-ICA 2013 (International)
- 2. ISRS-2014 (International)
- 3. Aligarh Nano IV International Conference 2014 (International)
- 4. Int. Conference on Nano science, Nanotechnology & Advanced Materials 2015 (International)

Further, the student has passed the following courses towards fulfilment of coursework requirement for Ph.D.

Course Code	Name	Credits	Pass/Fail
MT801	Research Methodology	4	Pass

and was exempted from doing coursework (recommended by Doctoral Committee) on the basis of the following courses passed during his M.Tech. program (in Int. M.Tech./Ph.D. program) and the M.Tech. degree was awarded:

Course Code	Name	Credits	Pass/Fail
NT401	Thermodynamics and Phase Equilibria	4	Pass
NT402	Concepts of Materials Science	4	Pass
NT403	Characterization of Materials	4	Pass
NT404	Seminar	2	Pass
NT405	Advanced Engineering Mathematics	2	Pass
NT406	Materials Processing and Characterization Laboratory	4	Pass
NT407	Concepts of Nano Science and Technology	4	Pass
NT408	Synthesis and Applications of Nanomaterials	4	Pass
NT451	Nano Biotechnology	4	Pass
NT452	Mechanical Behavior of Nanomaterials	4	Pass
NT453	Modeling and Simulation	4	Pass
NT454	MEMS AND NEMS Nanofabrication Technologies	4	Pass
NT455	Surface Engineering	4	Pass
NT456	Polymer Science and Technology	2	Pass
NT457	Laboratory	4	Pass
NT458	Seminar	2	Pass
NT550	Dissertation	18	Pass

Supervisor Dean of School

# **ACKNOWLEDGEMENTS**

I offer deep regards to my thesis supervisor Dr.-Ing. Vadali V. S. S. Srikanth, who has given liberty in my research work, incredible suggestions, encouragement, constant support and smart guidance. Apart from research he taught me how to be moral. I also owe thanks to Prof. M. Ghanashyam Krishna, Dean, Prof. K. Bhanu Sankara Rao, former Dean and all other faculty members, School of Engineering Sciences and Technology (SEST), University of Hyderabad (UoH) for all the support and teaching subjects during my M.Tech. course work.

Next, I would like to thank my doctoral review committee members namely Prof. M. Ghanashyam Krishna and Dr. A. Rajanikanth (School of Physics (SoP), UoH) for their valuable suggestions and thought provoking discussions whenever needed. I would like to extend my regards to Prof. S. Srinath and Prof. K. C. James Raju for allowing me to use the experimental facilities at SoP, UoH.

I owe special thanks to Mr. H. Binoy Krishna, Ph.D. scholar SoP, Dr. T. Anil Kumar (ACHREM), Dr. P. Suresh (SoP) for helping me in dielectric measurements which are an important part of my thesis work. Special thanks also to Mr. Santanu (Ph.D. scholar, ACHREM) for his help in sonication experiments, and Dr. Ahmed and Mr. M. Durga Prasad (Center for Nanotechnology, UoH) for their help in Raman and TEM experimentation, respectively. Thanks to lab technicians and non-teaching staff of SEST for their kind help.

On personal front, I owe special thanks to Dr. K. Mohan Kumar, Mr. M. Sandeep Kumar, Mr. K. V. Sreenivasulu and Mr. Md. Azamthulla (Ph.D. scholar, SoP) for their invaluable friendship and for always maintaining joyful mood and for their support during the research work. Thanks also to Dr. D. Sanjeev Kumar (SoP), Mr. M. Venkateswara Rao (Ph.D. scholar, IIT Madras), Mrs. M. Prasanna Lakshmi (Research Associate, DMRL, Hyderabad) and Dr. Kishore Gade (IISc Bangalore) for their truthful friendship, help, suggestions and support. I extend my regards to my lab mates for their help whenever needed.

Next, I would like to thank Mr. Shashidhar Gollagari (Bharat Dynamics Limited, Hyderabad), Mr. P. Krishna Yadav and Mr. P. Jaya Krishna for their genuine friendship, precious affection, and support.

There are no words to express my infinite gratitude towards my beloved parents Mr. Ankamma Rao Jammula and Mrs. Venkata Ratnam Jammula for their boundless love and affection. There are also no words to express my gratitude towards my brother Mr. Mallikharjuna Rao Jammula who took all the responsibilities of the family and always set conditions which enabled me to freely pursue research; moreover he supported and guided me in each and every stage of my life and sisters Mrs. Sesha Ratnam and Mrs. Vijaya Lakshmi for their genuine love and boundless affection without which I could not have come to the finishing stage of my Ph.D. degree. Finally, I dedicate this work to my beloved parents.

#### Rama Krishna Jammula

# Contents

Abstract	i
Chapter 1 Introduction	1
1.1 General background	1
1.2 Problem definition	3
1.3 Overview of the thesis	5
References	5
Chapter 2 Literature Review	7
2.1 Dielectric behavior of graphene and its analogues	7
2.2 Dielectric behavior of graphene/polymer composites	8
2.3 Dielectric behavior graphene/metal oxide composites	9
References	10
Chapter 3 Experimental Work	13
3.1 Synthesis of materials	13
3.1.1 Reduced graphene oxide	13
3.1.2 Metal oxide (CuO, ZnO, MgO and NiO)/r-GO nanocomposite	<b>s</b> 15
3.2 Characterization of materials	19
3.2.1 X-ray diffraction	19
3.2.2 Electron microscopy	19
3.2.3 Spectroscopy	20
3.3 Dielectric measurements	20
References	21
Chapter 4 Results and Discussion	23
4.1 CuO decked FLG	23
4.1.1 Structural, morphological, and phase analysis	23
4.1.2 Dielectric properties	31
4.2 ZnO decorated r-GO	36
4.2.1 General comments	36
4.2.2 Structural, morphological, and phase analysis	37
4.2.3 Dielectric behavior	42
4.2.4 Unique polarization and ionic conductivity	48
4.3 MgO decorated r-GO	60
4.3.1 General comments	60

4.3.2	Structural, morphological, and phase analysis	61
4.3.3	Non-Debye relaxation	64
4.4 N	IiO decorated r-GO	72
4.4.1	General comments	72
4.4.2	Structural, morphological, and phase analysis	73
4.4.3	Giant dielectric permittivity and percolation effect	77
Referenc	es	81
Chapter 5	Conclusions and Future Aspects	92
Referenc	es	95

# **Abstract**

Developing novel dielectric materials has always been an interesting area in material's research owing to their importance especially in capacitive energy storage. In this context, at the time of problem formulation for this thesis work (i.e., during the year 2012), the dielectric behavior of graphene filled polymers has attracted good attention. However, at that time there were no reported works on "dielectric behavior" of metal oxides (time tested dielectric materials) and graphene containing nanocomposites. Therefore in this thesis work elucidation of various aspects of dielectric behavior of reduced-graphene oxide (r-GO) and metal oxide containing nanocomposites has been taken up. Owing to the presence of residual oxygen functional groups and defects in r-GO, it is hypothesized that it will have a unique influence on the dielectric behavior of metal oxides and r-GO containing nanocomposites. As anticipated, a unique and strong interfacial polarization (Maxwell-Wagner polarization) was observed in metal oxide decorated r-GO nanocomposites synthesized by molecular level mixing technique which resulted in homogenous distribution of metal oxide particles on the surfaces of r-GO sheets. In this thesis work, CuO/r-GO, ZnO/r-GO, MgO/r-GO and NiO/r-GO nanocomposites were synthesized and their dielectric behavior in correlation with their morphology, crystallinity/phase and composition has been elucidated. This thesis also provides a comprehensive treatment to understand the dielectric behavior, especially the dielectric relaxation in metal oxide and r-GO containing nanocomposites. The treatment involves fitting experimental results with suitable theoretical models (for example, Havriliak-Negami relaxation model) that enable the intricate examination of physical mechanisms that controlled the dielectric behavior of the nanocomposites under consideration. Percolation effect on the dielectric permittivity was elucidated in the case of NiO/r-GO nanocomposite which exhibited a giant dielectric permittivity of 3688. This work will pave a way to understand and control the possible physical mechanisms that might take place at a very small length scales and in turn will be useful to control the dielectric behavior of graphene based nanocomposites in particular and nanocomposites, in general.

# **Chapter 1 Introduction**

## 1.1 General background

A dielectric material is an electrically insulating material that can be polarized by an applied external electric field. The electric charges in dielectric materials are typically restricted to migrate only locally (i.e., the charges slightly shift from their equilibrium positions) under the influence of an external electric field which creates induced dipole moments (in other words polarization takes place). Therefore it can be comprehended that the dielectric properties namely dielectric constant, dielectric break down and tangent loss strongly depend on polarization, in particular, the type of polarization mechanism. The major polarization mechanisms are electronic (due to the migration of outer electron cloud to an opposite direction of the applied electric field), ionic (due to the small displacement of ions), dipolar (due to the orientation of molecular dipoles) and space charge (due to the restricted migration of free electrons by barriers such as grain boundaries) in nature. Electronic and ionic polarizations usually occur at high frequencies (i.e., optical and infrared frequencies) while orientation polarization occurs at lower frequencies (i.e., frequencies up to microwave region). It should also be noted that electronic and ionic polarizations are induced polarizations (i.e., the polarization is observed only in presence of external electric field) while orientation polarization is not an induced one (i.e., it is due to the existence of permanent diploes). Polar molecules (which exhibit dipolar polarization which is also referred to as orientation polarization) also exhibit characteristic relaxation times (delayed response to the changing electric field direction) for orienting themselves in the applied field direction. If more polar molecules are present in the system at a given temperature, then at equilibrium the resultant polarization will be more.

For a material, the electric displacement (D) is directly proportional to the applied electric field (E) in the following manner:

$$D = \varepsilon_0 \varepsilon_r E$$
 ..... (Equation 1.1)

where  $\epsilon_0$  is the permittivity of free space and  $\epsilon_r$  is the relative permittivity of the material. For a dielectric material with a polarization P under the applied electric field E, D and P can be can be written as

$$D=\epsilon_o E+P ..... ( \mbox{Equation 1.2})$$
 
$$P=\ \epsilon_o\ (\epsilon_r-1)E=\alpha E\ ..... ( \mbox{Equation 1.3})$$

where  $\alpha = \epsilon_o (\epsilon_r - 1)$  is polarizability, a true material parameter.

For a system having N dipoles, Eq. 1.3 can be written as

$$P = N\alpha E$$
 ..... (**Equation 1.4**)

where  $\alpha = \alpha_e + \alpha_i + \alpha_o + \alpha_s$  is the sum of electronic  $(\alpha_e)$ , ionic  $(\alpha_i)$ , orientation  $(\alpha_o)$  and space charge  $(\alpha_s)$  polarizabilities which are mostly dependent on the material's composition. The electronic and ionic polarizations are nearly frequency independent for most of the dielectric materials and marginally affected by temperature. On the other hand, orientation polarization depends on both frequency and temperature. Depending on the polarization mechanisms, the dielectric materials may exhibit high dielectric constant values and hence useful in various applications. For a simple parallel plate capacitor configuration, the static dielectric constant  $(\epsilon^s)$  value of the dielectric medium between the conducting plates is obtained using the relations

$$C=\epsilon_0\epsilon_r(A/d)$$
 ...... (Equation 1.5) 
$$\label{eq:epsilon}$$
 and 
$$\epsilon^s=\epsilon_0\epsilon_r \ .....$$
 (Equation 1.6)

where C, A and d are capacitance, area and thickness of the sample, respectively. More specifically, in the case of alternating external electric field, P and D vary periodically with time. Here, it should be noted that the permittivity of the dielectric medium is a complex quantity whose real part  $(\epsilon')$  is obtained from the value of the capacitance while the imaginary part  $(\epsilon'')$  is obtained from the dielectric loss factor (tan  $\delta$ ) given by

$$\tan \delta = \frac{\epsilon''}{\epsilon'}$$
.....(Equation 1.7)

and the AC conductivity ( $\sigma$ ) of the medium given by

$$\sigma = \omega \epsilon_0 \epsilon_r \tan \delta$$
 ..... (Equation 1.8)

where  $\omega$  is the angular frequency of the alternating external electric field. It should be also noted that both  $\epsilon'$  and  $\epsilon''$  are frequency dependent. The charge stored (Q) in the capacitor is

$$Q = CVe^{i\omega t}$$
 ..... (Equation 1.9)

where V is the Voltage and t represents the time. The current flow (I) as the capacitor discharges in time t is given by

$$I = \frac{dQ}{dt} = i\omega CV = i\omega C_0 \varepsilon_r V \dots (Equation 1.10)$$

where  $\epsilon_r=\,\epsilon'-i\epsilon''$  and  $\,C_o$  is the initial capacitance. Here, I has two components namely  $I_C$ 

and  $I_R$ , the capacitive current proportional to charge stored in the capacitor and the resistive component representing energy loss or power dissipation in the dielectric medium, respectively.  $I_C$  leads Voltage by  $90^\circ$  while  $I_R$  is in phase with the voltage. I can be written as

$$I = I_C + I_R = i\omega C_o(\epsilon' - i\epsilon'')V \dots (Equation 1.11)$$

With regards to applications of dielectric materials, devices such as rectifiers, transducers, amplifiers etc., are fabricated using dielectric materials. Of late, development of novel and advanced dielectric materials has gained a lot of prominence owing to their usefulness in capacitive energy storage [1]. At the time of problem formulation for this thesis work (i.e., during the year 2012), the use of metal oxide and graphene containing advanced nanocomposites as energy storage materials (especially as electrode materials in lithium ion batteries (LIBs) and electrochemical capacitors (ECs) [2,3]) was gaining prominence. It was elucidated that the synergistic effect between graphene and metal oxides played an important role in the enhancement of the performance of LIBs and ECs. However, at that time there were no reported research works on dielectric behavior of metal oxide and graphene containing nanocomposites which could be of potential use in capacitive energy storage. There were only reported research works on the enhanced dielectric behavior of graphene filled polymer nanocomposites [4-6] owing the inclusion of graphene. However, due to the presence of stable residual oxygen functional groups in reduced graphene oxide (r-GO, a family member of graphene), it is expected to be a better dielectric material than monolayered and bi-layered graphene. Therefore, the motivation was to check the possibility to synthesize novel nanocomposites constituted by r-GO and well-known dielectric metal oxides with an aim to enhance the dielectric constant and lower the dielectric loss. If so, the motivation was also to check for the possible polarization mechanisms that could contribute (at small length scale) to the enhanced dielectric behavior of nanocomposites constituted by r-GO and metal oxides?

#### 1.2 Problem definition

Graphene (owing to its large aspect ratio) was used as a filler material to synthesize polymer matrix nanocomposites with enhanced dielectric performance [4-6] in comparison to the constituents. r-GO also comes under the same category (high surface to volume ratio) along with the presence of polar functional groups (PFGs) namely -OH, -CHO, -CO, and -COOH on its surfaces and edges and owing to these PFGs, r-GO is expected to be a better dielectric material than mono-layered and bi-layered graphene and if used as constituent in an

nanocomposite, it can provide many possibilities to control the dielectric behavior. On the other hand, there are many dielectric metal oxides; however, their dielectric constant values are very low. As mentioned before, dielectric constant is a material property and it mainly depends on polarization at a specified external electric field frequency. In this context, it was hypothesized that when metal oxides are decorated on r-GO there can be a synergistic effect between them (through PFGs) and as a consequence, unique dielectric behavior can be expected. This hypothesis had a strong support in the literature (details are in Chapter 2) that was available till the year 2012. Moreover, the oxygen vacancies and interstitials in metal oxides have often been useful as sources to control the polarization and hence the dielectric behavior of metal oxides. Due to the oxygen vacancies, a slightly off-stoichiometric metal oxide possess a partial positive charge and thereby creating possibilities to make suitable bonds with the negatively charged oxygenated PFGs attached to r-GO and a consequence forming stable metal oxide decorated r-GO nanocomposites constituted by unique materials (r-GO and nano-sized metal oxide particles), PFGs, defects (both in r-GO and metal oxide particles), and numerous interfaces (between r-GO and metal oxide particles). This gives a great opportunity to control the dielectric behavior of the nanocomposites and if possible. enhance the dielectric properties of the nanocomposites. For this thesis work, low dielectric constant possessing metal oxides namely CuO [7,8], ZnO [9,10], MgO [11,12] and NiO [13,14] were chosen in order to clearly observe any enhancement in dielectric constant of the nanocomposites in which the respective metal oxide will be a constituent along with r-GO. Bulk CuO, ZnO, MgO and NiO have low dielectric constant values typically in the range 10-25. However, by various manipulations, the dielectric constant values have been enhanced. For instance, bulk CuO when annealed at 950 °C exhibited an enhanced dielectric constant of 10<sup>4</sup> owing to the presence of trace amounts of Cu<sup>3+</sup> ions [15]. It was explained that the conduction mechanism in CuO is mainly governed by hopping of holes between Cu2+ and Cu<sup>3+</sup> which results in CuO grains (enriched with Cu<sup>3+</sup>) to exhibit p-type semi-conductance. But the grain boundaries might consist of only Cu<sup>2+</sup> and they behave as insulating walls. As a result, formation of an array of boundary barriers and grains takes places and as a consequence the annealed CuO exhibits a high dielectric constant.

In view of the above, the problems for this thesis work were defined as follows:

i) to synthesize metal oxide and r-GO containing nanocomposites using a simple, yet an effective method: at the time of the formulation of the problem, there were several synthesis

methods that could be used to synthesize metal oxide and r-GO containing nanocomposites. However, these methods were cumbersome.

- ii) to find out if the dielectric constant of the nanocomposites could be enhanced.
- iii) to explore, understand and elucidate the dielectric behavior of the nanocomposites in correlation with their microstructure, crystallinity and composition.
- iv) to elucidate any uniqueness (for example: the contribution from the interfaces between the metal oxide and r-GO to the overall dielectric behavior of the nanocomposite) found in the dielectric behavior of the nanocomposites with the aid of suitable theoretical models.
- v) to study the influence of percolation on the dielectric behaviour.

#### 1.3 Overview of the thesis

Structure of the remaining part of this thesis is as follows: In Chapter 2, the relevant literature that was reviewed while formulating the problem for this thesis work is presented. Other relevant works that were published by different research groups while this work was in progress have been discussed along with the results of this thesis work in Chapter 4. Chapter 3 covers the experimental work which includes the synthesis details of various materials, explanation of basic characterization experiments carried out to obtain structural, morphological and compositional details of the materials synthesized and explanation of the dielectric measurements on various materials considered in this thesis work. In Chapter 4, the discussion on all the experimental observations regarding structural, morphological, phase and dielectric characteristics of CuO/r-GO, ZnO/r-GO, MgO/r-GO and NiO/r-GO nanocomposites is presented. All the theoretical models used to understand the experimental dielectric observations are also presented in Chapter 4 at appropriate places in the thesis work. Conclusions and immediate future scope of this thesis work are given in Chapter 5.

## References

- [1] Scott JF. Applications of modern ferroelectrics. Science 2007;315(5814):954-9.
- [2] Wu ZS, Wang DW, Ren W, Zhao J, Zhou G, Li F, Cheng HM. Anchoring hydrous RuO<sub>2</sub> on graphene sheets for high performance electrochemical capacitors. Adv Fun Mat 2010;20(20):3595-602.
- [3] Wu ZS, Zhou G, Yin LC, Ren W, Li F, Cheng HM. Graphene/metal oxide composite electrode materials for energy storage. Nano Energy 2012;1(1):107-31.
- [4] Kim H, Abdala AA, Macosko CW. Graphene/polymer nanocomposites. Macromolecules 2010;43(16):6515-30.

- [5] Romasanta LJ, Hernández M, Lopez-Manchado MA, Verdejo R. Functionalised graphene sheets as effective high dielectric constant fillers. Nano Scale Res Lett 2011;6(1):508-6.
- [6] Verdejo R, Bernal MM, Romasanta LJ, Lopez-Manchado MA. Graphene filled polymer nanocomposites. J Mater Chem 2011;21(10):3301-10.
- [7] Collins BT, Desisto W, Kershaw R, Dwight K, Wold A. Preparation and characterization of Cu(II) oxide. J Less-Common Met 1989;156(1):341-346.
- [8] Zheng XG, Sakurai Y, Okayama Y, Yang TQ, Zhang LY, Nonaka K, Xu CN. Dielectric measurement to probe electron ordering and electron-spin interaction. J Appl Phys 2002;92(5):2703-2708.
- [9] Look DC, Reynolds DC, Sizelove JR, Jones RL, Litton CW, Cantwell G, Harsch WC. Electrical properties of bulk ZnO. Solid State Commun 1998;105(6):399-401.
- [10] Velayutham TS, Abd Majid WH, Gan WC, Zak AK, Gan SN. Theoretical and experimental approach on dielectric properties of ZnO nanoparticles and polyurethane/ZnO nanocomposites. J Appl Phys 2012;112:054106.
- [11] Bartels RA, Smith PA. Pressure and temperature dependence of the static dielectric constants of KC1, NaC1, LiF, and MgO. Phy Rev B 1973;7:3885.
- [12] Subramanian MA, Shannon RD, B.H.T. Chai, M.M. Abraham, Wintersgill MC, Dielectric constants of BeO, MgO, and CaO using the two-terminal method. Phys Chem Minerals 1989;16:741-6.
- [13] Rao KV, Smakula A. Dielectric properties of cobalt oxide, nickel oxide, and their mixed crystals. J Appl Phys 1965;36(6):2031-8.
- [14] Lin Y, Jiang L, Zhao R, Nan CW. High-permittivity core/shell structured NiO-based ceramics and their dielectric response mechanism. Phys Rev B 2005;72(1):014103-6.
- [15] Sarkar S, Jana PK, Chaudhuri BK. Copper (II) oxide as a giant dielectric material. Appl Phys Lett. 2006;89:212905.

# **Chapter 2** Literature Review

## 2.1 Dielectric behavior of graphene and its analogues

Before presenting the review on the dielectric behavior of graphene and its analogues, it is important to understand the concerned nomenclature [1] and the constitution of graphene analogues. Graphene is a monolayer of sp2 hybridized carbon atoms bonded) into a 2D honeycomb lattice. The term graphene was devised by combining the words 'graphite' (indicative of the parent material) and the suffix '-ene' (indicative of the presence of double bonds). A stack (along the axis perpendicular to the thickness of graphene sheets) of multiple layers of graphene held by van der Waals's interactions is known as multi-layered graphene (MLG). Similarly, a stack of only few (2-10) layers of graphene held by van der Waals's interactions is known as few-layered graphene (FLG). Graphene oxide (GO) is analogous to multi-layered graphene but attached with numerous oxygen containing functional groups namely, hydroxyl (-OH), carbonyls (C=O), carboxylic (-COOH) etc., groups on the basal planes and edges of the graphene layers that are stacked together. Due to the presence of these functional groups the inter-layer distance in GO is greater than that of MLG. Reduced graphene oxide (r-GO) has only few oxygen functional groups attached to the basal planes and edges of the graphene layers stacked together. r-GO is obtained by chemically reducing and exfoliating GO. If the reduction is ideal, one would obtain FLG (which has no functional groups attached to it). By controlling the reduction process, the type and number of residual oxygen functional groups can be controlled. This is where the motivation of this thesis work subsists i.e., to use these functional groups to control the dielectric behavior of nanocomposites in which r-GO will be one constituent. In this work, in section 4.1, the term FLG is used for r-GO while is all other sections i.e., 4.2-4.4 the term r-GO is used.

Graphene exhibits low dielectric constant ( $\epsilon'$ ) values in the range 2-16 [2-8], depending on the number of graphene layers staked along its c-axis. The dielectric constant of graphene (or staked few layers of graphene) is dependent on the strength of the Columbic interactions in the system. It was found that that the type of substrate on which graphene is grown and the applied electric field (whether it is applied to parallel or perpendicular to the graphene layer) also influence the dielectric constant of graphene [9].  $\epsilon'$  value of mono-layer graphene is lower in comparison to bi-layered graphene while that of bi-layered graphene's  $\epsilon'$  value is lower than that of MLG's  $\epsilon'$  value suggesting that the polarization behavior is different in each case [10]. The non-linear nature of strength of the Columbic interactions in MLG was

attributed to the enhanced dielectric behavior with increase in number of layers [11,12]. Additionally, the finite thickness of graphene layer and its polarizability might increase the interlayer capacitance in the multi-layered system [13]. On the other hand, it is well known that the dielectric constant decreases as the frequency of the applied electric field increases; this is owing to the out-of-phase response of dipoles in the system. In this context, in the Giga range frequencies, mono-layered graphene exhibits an effective dielectric permittivity value of 3.3. All in all, it is clear that graphene is an intrinsically low dielectric constant exhibiting material owing to its  $\pi$ -electron delocalization while the dielectric constant value can be enhanced by synthesizing FLG or r-GO.

GO and r-GO, the above described analogues of MLG, have also exhibited dielectric behavior attributed mainly to the presence of oxygen functional groups [14,15]. In a unique case, when the carbon vacancy sites in r-GO were filled with Co atoms, unusual dielectric response (i.e., a huge enhancement in dielectric constant) was recorded for the Co doped r-GO. The unusual dielectric response was explained by using a trap induced capacitance model [15]. Unlike in the case of typical dielectric materials, the permittivity values increased instead of decreasing with frequency. The permittivity was observed to increase up to certain frequency at which all the trap states were filled with conduction electrons. After reaching the characteristic frequency (above the resonance condition) the permittivity values decreased due to out of phase response of the trapped charge carriers [16].

# 2.2 Dielectric behavior of graphene/polymer composites

In pursuit of enhancing the dielectric constant which directly influences the charge storage capacity of a material, FLG (or r-GO) filled polymer nanocomposites [17-26] were also synthesized. In this class of materials with enhanced dielectric constants, FLG (or r-GO) filled polycarbonate, polyimide, polystyrene, polymethylmethacrylate, polyvinylidene fluoride, polypyrole, polyvinyl alcohol and polyaniline nanocomposites are the significant ones. By virtue of the microstructure of these nanocomposites, there will be induced space charge polarization between the interfaces of the polymer and FLG (or r-GO) and results in the enhancement of the dielectric constant and capacitance of the system. The negative charges are accumulated on the surfaces of FLG (or r-GO) while positive charges are accumulated on the polymer surfaces resulting in the increment in local electric field and thereby enhancing the charge accumulation probability in such nanocomposites [23]. In a unique work [27] it was shown that the use of chlorinate r-GO as a filler, increases the

dielectric constant of Cl-r-GO/N,N- dimethylformamide/ cyanoethyl pullulan polymer nanocomposite. When typical r-GO was used as the filler, a dielectric constant of ~24 and a dielectric loss of ~0.051 at 10 Hz were measured for r-GO/N,N- dimethylformamide/ cyanoethyl pullulan polymer nanocomposite. On the other hand, when Cl-r-GO was used instead of r-GO, the nanocomposite exhibited a dielectric constant of ~169 and a dielectric loss of ~0.05 at 10 Hz. This large enhancement in the dielectric constant was attributed to the interfacial polarization between the Cl-rGO platelets and the polymer.

In an interesting work, it was shown that aspect ratio and oxidation degree of r-GO strongly effected the dielectric constant of the r-GO/poly(dimethyl siloxane) nanocomposites [24]. Alignment of r-GO in the polymer matrix has also shown a strong influence on the dielectric behavior of r-GO/epoxy nanocomposites [28]. Highly aligned r-GO in r-GO/epoxy nanocomposite exhibited a dielectric constant as high as 14000 at 1 k Hz frequency. This was attributed to the accumulation of charge carriers at the highly-aligned conductive filler/insulating polymer interface on account of Maxwell-Wagner-Sillars polarization.

#### 2.3 Dielectric behavior graphene/metal oxide composites

As stated in Chapter 1, when this work was started, there were only no reports on dielectric behavior of graphene/metal-oxide composites. However, there are contemporary works which are briefly reviewed here. When graphene was combined with ceramics, effects similar to trap induced capacitance [15,16] have been observed as in graphene/ZnCo<sub>2</sub>O<sub>4</sub> nanocomposite [29]. All other dielectric nanocomposites that are constituted by graphene and metal oxide, also contained polymer in them [30-34]. Some of these [31,32] have exhibited extremely high (as high as 45000 at 1 kHz) dielectric constant values. However, there were no works that elucidated the dielectric behavior of graphene/metal-oxide composites at small length scales. Compared with their individual constituents, graphene/metal oxide composites exhibit unique microstructural variables in the form of anchored, wrapped, encapsulated, sandwich, layered and mixed microstructure models. These structures form due to oxygen containing groups on graphene and ensure good bonding, interfacial interactions and electrical contacts between graphene and metal oxide. At the same time, metal oxide prevents the restacking of graphene sheets and enhances performance of the composite. Graphene supported metal oxide can form a perfect integrated structure with a suitable electron conductive network and shortened charge transport paths. Significant synergistic effects often occur due to size effects and interfacial interactions of metal oxides with graphene.

#### References

- [1] Bianco A. All in the graphene family—a recommended nomenclature for two-dimensional carbon materials, Carbon 2013;65:1-6.
- [2] Siegel DA, Park CH, Hwang C, Deslippe J, Fedorov AV, Louie SG, Lanzara A. Manybody interactions in quasifreestanding graphene. Proc Natl Acad Sci 2011;108(28):11365-9.
- [3] Hwang C, Siegel DA, Mo SK, Regan W, Ismach A, Zhang Y, Zettl A, Lanzara A. Fermi velocity engineering in graphene by substrate modification. Sci Rep 2012;2:590-4.
- [4] Bostwick A, Speck F, Seyller T, Horn K, Polini M, Asgari R, MacDonald AH, Rotenberg E. Observation of plasmarons in quasi-freestanding doped graphene. Science 2010;328(5981):999-1002.
- [5] Wang Y, Brar VW, Shytov AV, Wu Q, Regan W, Tsai HZ, Zettl A, Levitov LS, Crommie MF. Mapping Dirac quasiparticles near a single coulomb impurity on graphene. Nat Phys 2012;8(9):653-7.
- [6] Sanchez-Yamagishi JD, Taychatanapat T, Watanabe K, Taniguchi T, Yacoby A, Jarillo-Herrero P. Quantum hall effect, screening, and layer-polarized insulating states in twisted bilayer graphene. Phys Rev Lett 2012;108(7):076601-6.
- [7] Fallahazad B, Hao Y, Lee K, Kim S, Ruoff RS, Tutuc E. Quantum hall effect in bernal stacked and twisted bilayer graphene grown on Cu by chemical vapour deposition. Phys Rev B 2012;85(20):201408-5.
- [8] Reed JP, Uchoa B, Joe YI, Gan Y, Casa D, Fradkin E, Abbamonte P. The effective fine-structure constant of freestanding graphene measured in graphite. Science 2010;330(6005):805-8.
- [9] Santos EJG, Kaxiras E. Electric-field dependence of the effective dielectric constant in graphene. Nano Lett 2013;13(3):898-902.
- [10] Jellison GE, Hunn JD, Lee HN. Measurement of optical functions of highly oriented pyrolytic graphite in the visible. Phys Rev B 2007;76(8):085125-33.
- [11] Jang C, Adam S, Chen JH, Williams ED, Das Sarma S, Fuhrer MS. Tuning the effective fine structure constant in graphene: Opposing effects of dielectric screening on short-and long-range potential scattering. Phys Rev Lett 2008;101(14):146805-9.
- [12] Kuroda MA, Tersoff J, Martyna GJ. Nonlinear screening in multilayer graphene systems. Phys Rev Lett 2011;106(11):116804-8.
- [13] Hwang EH, Sarma SD. Dielectric function, screening, and plasmons in two-dimensional graphene. Phys Rev B 2007;75(20):205418-23.

- [14] Saloma FC, Lanzoni EM, Costa CA, Deneke C, Barros EB. Determination of high-frequency dielectric constant and surface potential of graphene oxide and influence of humidity by kelvin probe force microscopy. Langmuir 2015;31(41):11339-43.
- [15] Akhtar AJ, Gupta A, Shaw BK, Saha SK. Unusual dielectric response in cobalt doped reduced graphene oxide. Appl Phys Lett 2013;103(24):242902-5.
- [16] Bisquert J. Beyond the quasistatic approximation: Impedance and capacitance of an exponential distribution of traps. Phys Rev B 2008;77(23):235203-15.
- [17] Compton OC, Kim S, Pierre C, Torkelson JM, Nguyen ST. Crumpled graphene nanosheets as highly effective barrier property enhancers. Adv Mater 2010;22(42):4759-63.
- [18] Higginbotham AL, Lomeda JR, Morgan AB, Tour JM. Graphite oxide flame-retardant polymer nanocomposites. ACS Appl Mater Inter 2009;1(10): 2256-61.
- [19] Kim H, Abdala AA, Macosko CW. Graphene/polymer nanocomposites. Macromolecules 2010;43(16):6515-30.
- [20] Stankovich S, Dikin DA, Dommett GH, Kohlhaas KM, Zimney EJ, Stach EA, Piner RD, Nguyen ST, Ruoff RS. Graphene-based composite materials. Nature 2006;442(7100):282-6.
- [21] Fang M, Wang K, Lu H, Yang Y, Nutt S. Covalent polymer functionalization of graphene nanosheets and mechanical properties of composites. J Mater Chem 2009;19:7098-105.
- [22] Chen D, Zhu H, Liu T. In situ thermal preparation of polyimide nanocomposite films containing functionalized graphene sheets. ACS Appl Mater Inter 2010;2(12):3702-8.
- [23] Chen Q, Du PY, Jin L, Weng WJ, Han GR. Percolative conductor/polymer composite films with significant dielectric properties. Appl Phys Lett 2007;91:022912-3.
- [24] Wang Z, Nelson JK, Hillborg H, Zhao S, Schadler LS. Graphene oxide filled nanocomposite with novel electrical and dielectric properties. Adv Mater 2012;24:3134-7.
- [25] Deshmukh K, Ahamed MB, Khadheer Pasha SK, Deshmukh RR, Bhagat PR. Highly dispersible graphene oxide reinforced polypyrrole/polyvinyl alcohol blend nanocomposites with high dielectric constant and low dielectric loss. RSC Adv 2015;5(76):61933-45.
- [26] Yu L, Zhang YH, Tong WS, Shang JW, Lv FZ, Chu PK, Guo W. Hierarchical composites of conductivity controllable polyaniline layers on the exfoliated graphite for dielectric application. Compos Part A Appl Sci Manuf 2012;43(11):2039-45.
- [27] Kim JY, Lee WH, Suk JW, Potts JR, Chou H, Kholmanov IN, Piner RD, Lee J, Akinwande D, Ruoff RS. Chlorination of reduced graphene oxide enhances the dielectric constant of reduced graphene oxide/polymer composites. Adv Mater 2013;25(16):2308-13.

- [28] Yousefi N, Sun Xi, Lin Xi, Shen Xi, Jia J, Zhang B, Tang B, Chan M, Kim JK. Highly aligned graphene/polymer nanocomposites with excellent dielectric properties for high-performance electromagnetic interference shielding. Adv Mater 2014;26(31):5480-5487.
- [29] Baskey M, Maiti R, Saha SK, Chakravorty D. Superior magnetic, dielectric, and magneto dielectric effects in graphene/ZnCo<sub>2</sub>O<sub>4</sub> nanocomposites. J Appl Phys 2014;115(9):094306-7.
- [30] Wang D, Zhou T, Zha JW, Zhao J, Shi CY, Dang ZM. Functionalized graphene-BaTiO<sub>3</sub>/ferroelectric polymer nanodielectric composites with high permittivity, low dielectric loss, and low percolation threshold. J Mater Chem A 2013;1:6162-8.
- [31] Sun J, Xue Q, Guo Q, Tao Y, Xing W. Excellent dielectric properties of polyvinylidene fluoride composites based on sandwich structured MnO<sub>2</sub>/graphene nanosheets/MnO<sub>2</sub>. Compos Part A Appl Sci Manuf 2014;67:252-258.
- [32] Fernandez-Garcia L, Suarez M, Menendez JL, Pecharroman C, Menendez R, Santamaria R. Dielectric behavior of ceramic graphene composites around the percolation threshold. Nanoscale Res Lett 2015;10:216.
- [33] He F, Lam K, Ma D, Fan J, Chan LH, Zhang L. Fabrication of graphene nanosheet (GNS)–Fe<sub>3</sub>O<sub>4</sub> hybrids and GNS–Fe<sub>3</sub>O<sub>4</sub>/syndiotactic polystyrene composites with high dielectric permittivity. Carbon 2013;58:175-184.
- [34] Bindu Sharmila TK, Antony JV, Jayakrishnan MP, Beegum PMS, Thachil ET. Mechanical, thermal and dielectric properties of hybrid composites of epoxy and reduced graphene oxide/iron oxide. Mater Des 2016;90(15):66-75.

# **Chapter 3** Experimental Work

## 3.1 Synthesis of materials

#### 3.1.1 Reduced graphene oxide

In this work, reduced graphene oxide (r-GO) samples were synthesized from graphene oxide (GO) which was prior synthesized by using Hummers Method (HM) [1] and Improved Hummers Method (IHM). In these methods, the staring material was graphite ( $\sim$ 325 mesh, flake/particle size  $\sim$ 44  $\mu$ m, Alfa Acer make). Each synthesis method has been elaborated in the following paragraphs:

Hummers method: 9 g of graphite flakes are added to 225 ml of Conc. H<sub>2</sub>SO<sub>4</sub> (98%, Fisher Scientific make) and stirred for 2 h. To this mixture, 4.5 g of NaNO<sub>3</sub> (98%, Fisher Scientific make) was added and stirred for 15 min. These steps are carried out under room conditions. The idea behind oxidation of graphite (i.e., making GO) is to increase the inter-planar spacing (to > 0.3 nm) between the basal plans. For further oxidation, in the next step 27 g of KMnO<sub>4</sub> was added to above mixture. During this step, temperature of the reaction mixture was maintained at 0 °C using an ice bath because the process of KMnO<sub>4</sub> addition is highly exothermic [1]. The reaction mixture was then stirred at room temperature for 45 min. In the next step, 225 ml of distilled water was added slowly to the reaction mixture and during this time temperature of the solution was raised to 98 °C. For the next 1 h the reaction mixture was maintained at 98 °C. Thereafter the mixture was allowed to cool down to room temperature. For further oxidization, 7.5 ml of H<sub>2</sub>O<sub>2</sub> was added to the mixture. Finally the mixture was diluted with distilled water (by adding 2 to 2.5 l of it). The resultant solution was pale yellow in colour as shown in Fig. 3.1(a).

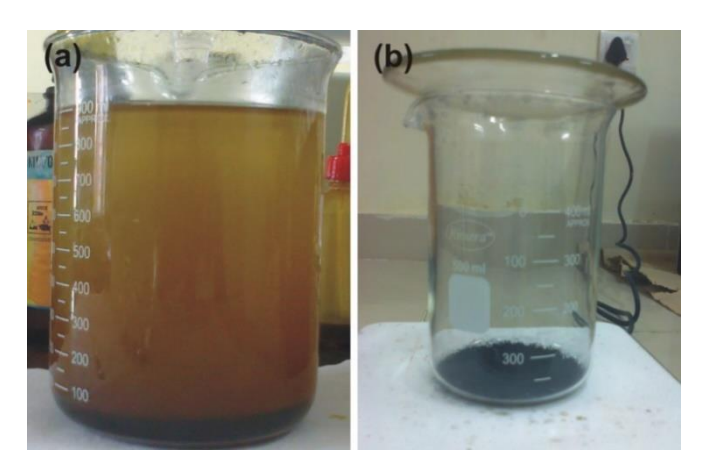


**Figure 3.1.** Photographs of (a) GO suspension prepared by HM. (Capacity of the beaker is 1 l) and (b) thermally exfoliated r-GO from GO prepared by HM (300 ml beaker).

After sometime, the oxidized material that settled at the bottom of the beaker was filtered. The filtrate was then subjected to multiple washes with distilled water until the suspension of the filtrate attained a pH of ~7. The filtrate was finally collected and kept overnight in a hot oven at 100 °C to obtain GO powder. The dried GO powder was placed on a borosilicate glass and introduced into a hot oven at temperature 400 °C in air atmosphere for few minutes. This resulted in exfoliation of GO to r-GO. The reason for such an exfoliation has been attributed to vaporization of intercalated water molecules and oxide groups of hydroxyl, carboxyl groups etc. [2]. **Fig. 3.1(b)** shows the photograph of r-GO in a beaker. So-obtained r-GO was used in the synthesis of ZnO decorated r-GO, MgO decorated r-GO and NiO decorated r-GO nanocomposites.

Improved Hummers method: Here, 3 g of graphite flakes are added to a mixture of 9:1 Conc. H<sub>2</sub>SO<sub>4</sub>/H<sub>3</sub>PO<sub>4</sub> (360:40 ml). This reaction is an exothermic reaction and produces a slight increase in temperature (~35 to 40 °C). After 30 min of stirring, 18 g KMnO<sub>4</sub> was added to the reaction mixture and maintained at a temperature of 50 °C while stirring for 12 h. The reaction mixture was then cooled to room temperature and subsequently kept on an ice bath at 0 °C. Then 400 ml of distilled water was poured into the mixture along with 3 ml of H<sub>2</sub>O<sub>2</sub> [3]. The resultant solution was pink in color (**Fig. 3.2(a**)) and acidic in nature. The solution was subjected to multiple washes with distilled water such that it attains a pH of about 7. Finally the filtrate was collected and kept in a hot oven at 100 °C overnight to obtain GO fine powder. FLG was then synthesized from GO by thermal exfoliation at 400 °C in air atmosphere as mentioned in the above section. So-obtained FLG was used in the synthesis of CuO decked FLG. **Fig. 3.2(b**) shows the photograph of FLG in a beaker.

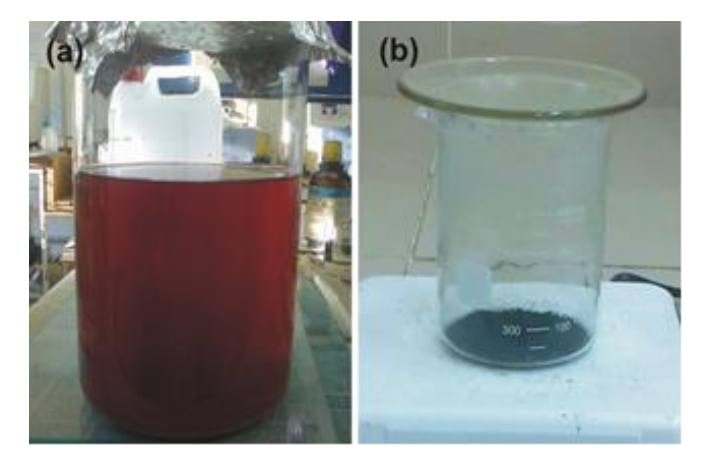


**Figure 3.2.** Photographs of (a) GO suspension prepared by IHM (capacity of the beaker is 1 liter) and (b) thermally exfoliated FLG from GO prepared by IHM (300 ml beaker).

### 3.1.2 Metal oxide (CuO, ZnO, MgO and NiO)/r-GO nanocomposites

As mentioned in Chapter 1, when this work was planned, there were already established synthesis methods that could be used to synthesize metal oxide and graphene containing nanocomposites [4-6]. However, these methods were cumbersome. Therefore in the pursuit of an easy synthesis method, molecular mixing (MLM) technique [7-10] was found out. This technique was used in the case of synthesizing nanocomposites consisting of functionalized carbon nanotubes (CNTs) and metal oxides. In this method the metal ions get attached to the surfaces of the carbon nanostructures through functional groups and a subsequent calcination process allows the formation of metal oxides on the surfaces of carbon nanostructures. In this thesis work, MLM technique was improvised to synthesize CuO decked FLG, ZnO decorated r-GO, MgO decorated r-GO and NiO decorated r-GO nanocomposites.

In this work, for synthesizing nanocomposites direct sonication method (i.e., inserting a sonication probe directly into a sample vessel) was used. In this method the energy is transmitted from the probe directly into the sample with high intensity and the sample is processed quickly. In the present work the probe sonicator was operated at 700 W power, 20 kHz frequency and wave amplitude of 60 to 70% of the maximum in a continuous pulse mode. Every half hour, 10 minutes break time was also given. During the sonication process, the glass beaker (1 l) was kept in an ice bath at 0 °C for minimising heat that would be generated inside the beaker during the process. The photograph of the probe sonicator used in this thesis work is shown in **Fig. 3.3**.



Figure 3.3. Photograph of the probe sonicator used in this thesis work.

Once the process starts, high power ultrasound waves enter the liquid medium (precursors + solvent in 1 l glass beaker) and create compression and rarefaction cycles depending on the applied frequency. During these cycles high-intensity ultrasonic waves will create small vacuum bubbles or voids in the liquid medium. During the process, any solute undergoes thermolysis along with the formation of highly reactive radicals and reagents. When the bubbles attain a certain volume at which they can no longer absorb the energy. The bubbles then collapse violently during high-pressure cycles. This phenomenon is termed as cavitation. During this disintegration process very high temperatures around 5000 K and high pressures of around 2000 atm are created locally [11,12]. In addition to the dependency on input energy, the cavitation also depends up on the type of precursors which are used in the reaction. When non-volatile precursors (such as r-GO and metal salts in this work) dispersed in volatile solvents (such as ethanol) undergo cavitation process, free metal cations are formed on account of bond dissociation and weak metal bonds are formed finally resulting in the formation of functional nanomaterials [13-16]. Besides this, inter-particle collisions can also bring changes in particle size distributions, particle morphology and composition [17,18]. If the reaction solution contains metal salts and oxygen (or chalcogen) source sonication process results in the formation of reactive species such as reactive radicals of oxygen or chalcogen and these will react with metal ions in the solution to form metal oxides or metal chalcogenides.

Based on the above mentioned concepts and the existing literature [7-10], MLM technique was tried to synthesize CuO decked FLG, ZnO decorated r-GO, MgO decorated r-GO and NiO decorated r-GO nanocomposites as explained separately in the following paragraphs. Here it should be noted that the calcination temperature in each case was decided based on the metal oxide to be formed.

Synthesis of CuO decked FLG nanocomposite: In the synthesis of CuO decked FLG nanocomposite, FLG that has been synthesized from GO prepared by IHM was used. CuO decked FLG nanocomposite synthesis involved mainly four steps. In the first step, 0.1 gm of FLG powder is dispersed in 250 ml ethanol by sonication for 30 min and obtains a stable suspension by attaching the functional groups onto FLG surfaces. In this situation sonication helps in preventing the particle agglomeration and in maintaining uniform dispersion of FLG sheets in the solvent [8,9,19]. In the second step, 0.9 gm of copper acetate monohydrate (Cu(CH<sub>3</sub>COO)<sub>2</sub>·H<sub>2</sub>O) was added to the FLG suspension, which was again sonicated for 2 h. Sonication assists the dispersion of copper ions among the suspended FLG sheets and

promotes the reaction between copper ions and functional groups on FLG sheets. In the third step, the solution was vaporized while stirring it at 100 °C in air atmosphere. During this process, solvent and ligands are expected to be removed while the Cu ions on FLG surfaces are oxidized. The fourth and final step involves calcination process to obtain stable crystalline powders. The outcome of the third step might result in a mixture of FLG, CuO, and Cu<sub>2</sub>O. Heating the product at 400 °C for 8 h in ambient atmosphere yields CuO decked FLG. Two CuO decked FLG samples have been prepared in this manner. The one prepared following the procedure described above has been named as CuO-0.1G. Another sample is named as CuO-0.2G. This sample was prepared by considering 0.2 gm of FLG and 0.8 gm of Cu(CH<sub>3</sub>COO)<sub>2</sub>·H<sub>2</sub>O. For comparison purposes, CuO was also prepared following the procedure described above but without the presence of FLG.

Synthesis of ZnO decorated r-GO nanocomposite: Here, firstly, 0.1 g of r-GO powder was dispersed in 250 ml of ethanol by sonication for 30 min to obtain a stable suspension by attaching the functional groups onto r-GO surfaces. Next, 0.9 g of zinc acetate dehydrate (Zn(CH<sub>3</sub>COO)<sub>2</sub>·2H<sub>2</sub>O) was added to the r-GO suspension and the mixture was then sonicated for 2 h. Sonication assists the dispersion of Zn ions among the suspended r-GO sheets and promotes the reaction between Zn ions and functional groups on the r-GO sheets. Next, the solution was vaporized while stirring it at 100 °C in air. During this process, solvent and ligands are expected to be removed, while the Zn ions on r-GO surfaces are expected to form ZnO similar to the case of CuO decked FLG. The final step involved heating (calcination process to obtain stable crystalline powders) the product at 500 °C for 8 h in ambient atmosphere to obtain ZnO decorated r-GO named as ZnO-0.1G. Two other ZnO decorated r-GO samples were similarly prepared in this study. They are named as ZnO-0.2G and ZnO-0.3G in the order of increasing r-GO content. The ZnO-0.2G sample was prepared by 0.2 g of r-GO and 0.8 g of Zn(CH<sub>3</sub>COO)<sub>2</sub>·2H<sub>2</sub>O, whilst the ZnO-0.3G sample was prepared by 0.3 g of r-GO and 0.7 g of Zn(CH<sub>3</sub>COO)<sub>2</sub>·2H<sub>2</sub>O. For comparison purposes, ZnO nanoparticles were also synthesized by a typical wet chemical method using zinc chloride (ZnCl<sub>2</sub>) and sodium hydroxide (NaOH) as precursors. 0.8 M NaOH solution was added dropwise to a 0.4 M ZnCl<sub>2</sub> solution under constant stirring, which was continued for 2 h even after the complete addition of NaOH solution. The beaker containing the resultant white coloured solution was then sealed and allowed to precipitate overnight. The obtained precipitate was washed 5 times with deionized water to remove any by-products and obtain zinc hydroxide, which was then heated in air at 500 °C to obtain ZnO. Another set of synthesis experiments

were conducted in order to induce a change in polarization behavior of ZnO decorated r-GO nanocomposites, if any. These experiments are presented in section 4.4.3.

Synthesis of MgO decorated r-GO nanocomposite: Here, firstly 0.05 g of r-GO was dispersed in 200 ml of ethanol by sonication for 30 min to obtain a solution with homogeneously dispersed r-GO. Then, 0.95 g of magnesium acetate tetrahydrate Mg(CH<sub>3</sub>COO)<sub>2</sub>.4H<sub>2</sub>O was added to the r-GO solution and sonicated for 2 h anticipating the attachment of Mg ions onto the surfaces of r-GO particles. The resultant solution was then kept at 80 °C under stirring until the evaporation of ethanol. So-obtained product was heated at 600 °C for 8 h under atmospheric conditions (thermal oxidation and for stabilized MgO phase) resulting in MgO decked r-GO composite which is named as MgO-0.05G. The above described synthesis procedure was used to prepare two other MgO decorated r-GO composites named MgO-0.1G and MgO-0.15G. These composites are prepared by varying the r-GO content in the synthesis procedure. MgO-0.1G and MgO-0.15G are synthesized by considering 0.1 g of r-GO and 0.9 g of Mg(CH<sub>3</sub>COO)<sub>2</sub>.4H<sub>2</sub>O and 0.15 g of r-GO and 0.85 g of Mg(CH<sub>3</sub>COO)<sub>2</sub>.4H<sub>2</sub>O, respectively, in the above synthesis procedure.

Synthesis of NiO decorated r-GO nanocomposite: Here, in the first step, 0.004 gm of r-GO powder was dispersed in 200 ml ethanol by sonication for 30 min to obtain a stable suspension of r-GO. In the second step, 0.996 gm of nickel acetate tetrahydrate (Ni(CH<sub>3</sub>COO)<sub>2</sub>.4H<sub>2</sub>O) was added to the r-GO suspension, which was again sonicated for 3.5 h. Sonication assists the dispersion of nickel ions among the suspended r-GO sheets and promotes the reaction between nickel ions and functional groups on r-GO sheets. In the third step, the solution was vaporized while stirring it at 70 °C in air atmosphere. During this process, solvent and ligands are expected to be removed while the Ni ions on r-GO surfaces are oxidized. The fourth and final step involves calcination process to obtain stable crystalline powders. By heating the product at 500 °C for 8 h in ambient atmosphere yielded NiO decked r-GO named as NiO-0.004G (with 0.4 weight % of r-GO). The above described synthesis procedure was used to prepare other NiO decorated r-GO nanocomposites named as NiO-0.008G, NiO-0.012G, NiO-0.016G, NiO-0.024G and NiO-0.028G by varying the percentage of r-GO as 0.8, 1.2, 1.6, 2.4 and 2.8% by weight, respectively. These samples were prepared by considering 0.008 g of r-GO and 0.992 g of Ni(CH<sub>3</sub>COO)<sub>2</sub>.4H<sub>2</sub>O, 0.012 g of r-GO and 0.988 g of Ni(CH<sub>3</sub>COO)<sub>2</sub>.4H<sub>2</sub>O, 0.016 g of r-GO and 0.984 g of Ni(CH<sub>3</sub>COO)<sub>2</sub>.4H<sub>2</sub>O, 0.024g of r-GO and 0.976 g Ni(CH<sub>3</sub>COO)<sub>2</sub>.4H<sub>2</sub>O and 0.028 g of r-GO and 0.972 g of

Ni(CH<sub>3</sub>COO)<sub>2</sub>.4H<sub>2</sub>O. For comparison studies NiO was prepared using sonochemical route which involved gradual drop-wise addition of 0.1 M sodium hydroxide (NaOH) to 0.1 M nickel nitrate Ni(NO<sub>3</sub>)<sub>2</sub> solution and vigorous stirring until the pH value will becomes 7 (results in a light-green solution) and this solution was sonicated for 1 h. This results in the formation of a gel which was died at 90 °C by keeping it overnight on a magnetic stirrer. Soformed powder was heated at 400 °C for 5 h to obtain nanocrystalline NiO particles.

#### 3.2 Characterization of materials

#### 3.2.1 X-ray diffraction

To determine the crystallinity (based on Bragg's law,  $2d\sin\theta = n\lambda$ , which relates the wave length of incident X-ray radiation to the diffraction angle  $\theta$  and lattice spacing d) of different materials synthesized in this work, X-ray diffraction (XRD) experiments were carried out using Bruker AXS Model D8 Advanced X-ray diffractometer which was operated at 40 kV and 250 mA. XRD patterns were recorded in the  $2\theta$  range  $10^{\circ}$ - $90^{\circ}$  using Cu K $\alpha$  as the x-ray source ( $\lambda$ =1.54 Å) with a step size of 0.02 in  $\theta$ - $2\theta$  configuration at room temperature. In all the measurements sample amount of ~10 mg was used. XRD patterns were indexed following the standard procedures. XRD patterns were also matched with the respective JCPDS data. In the case of GO and r-GO/FLG, the thickness (t) of each GO or r-GO was calculated by using Debye Scherrer's formula (t = k  $\lambda$ /  $\beta$  Cos $\theta$  where k is Scherrer's constant (0.89),  $\beta$  =  $\sqrt{\beta_s^2 - \beta_l^2}$  where  $\beta_s$  and  $\beta_l$  are FWHM of sample and instrumental broadening (0.045), respectively,  $\theta$  is Bragg's diffraction angle and  $\lambda$  is incident wavelength). The number of layers in each GO or r-GO/FLG is equal to t/d spacing obtained using (002) peak. In cases which required understanding the precise lattice parameters, FULL-PROF program was used to construct (Rietveld refinement) XRD profiles.

#### 3.2.2 Electron microscopy

Morphology of the samples was studied by using field emission scanning electron microscope (FESEM) (Model: Zeiss ultra55). Secondary electron (SE) micrographs were obtained using an accelerating voltage of 5 kV. Morphological studies were also carried out using transmission electron microscope (TEM) (Model: FEI Technai G2 S–Twin). The operating accelerating voltage of TEM was 200 kV. Electron diffraction was considered to ascertain the crystallinity of the samples. For FESEM analysis, the powder samples were uniformly dispersed on a conducting carbon tape and no other sample preparation was necessary. However, in the case of TEM analysis, the samples were prepared in the following

manner: small amount (~1 mg) of the sample (r-GO and metal-oxide (CuO, ZnO, NiO and MgO) decked/decorated r-GO nanocomposites) was dispersed in ethanol of 20 ml and sonicated for 25 min in order to prepare an uniform dispersion of the sample in the solvent. Then, with the help of a micro syringe, 2 to 3 drops of the solution was carefully dropped onto a carbon coated TEM grid. The grid was then allowed dry overnight at room temperature. The dried grid with the sample was used for TEM investigation.

# 3.2.3 Spectroscopy

In order to understand the bonding nature in different materials, Raman scattering and Fourier transform infrared (FTIR) spectroscopy were carried out. Raman scattering was carried out using Witech-alpha 300 Raman spectrometer. Raman spectra were recorded by using Nd-YAG LASER (wave length = 532 nm). LASER power was kept at 10% of the maximum power (40 mW) in order to avoid any thermal influences. The LASER beam (spot size ~1 µm) was focused onto the sample by means of a confocal microscope equipped with 100x objective. Raman studies were carried out in the spectral range of 200–3000 cm<sup>-1</sup>. The focal condition of the LASER and integration time (of 5 s) was maintained the same for all Raman scattering measurements. Lorentz or double peak-Lorentz functions were used to peak fit certain Raman peaks to obtain intensity and full-width at half maximum (FWHM) values. In order to identify specific functional groups in the materials synthesized in this work, FTIR spectroscopic measurements were carried out using JASCO make (FT/IR-4200 type A) analytical FTIR spectrometer. FTIR spectra were collected at room temperature in the wavenumber range 4000-400 cm<sup>-1</sup>. Each sample was pressed into a pellet along with spectroscopic grade KBr. FTIR measurements were carried out on these pellets.

#### 3.3 Dielectric measurements

For dielectric measurements, pellets (8 and 2 mm in diameter and thickness, respectively) of the samples were made. Measurements were made in the frequency range 100 Hz-2 MHz at room temperature and also at temperatures in the range 30-400 °C at fixed frequencies by using E4980A LCR meter (AGILENT make, Precision Impedance Analyzer, **Fig. 3.4**). Parallel plate capacitor method was used to determine all the characteristics of the samples. The temperature dependent electric modulus  $M^* = M' + jM'' = \frac{\epsilon'}{\epsilon'^2 + \epsilon''^2} + j \frac{\epsilon''}{\epsilon'^2 + \epsilon''^2}$  was studied at selected frequencies in the range 1-10 kHz. Here, M' and M'' are real and imaginary parts respectively of the electric modulus representing energy storage and loss factor, respectively.

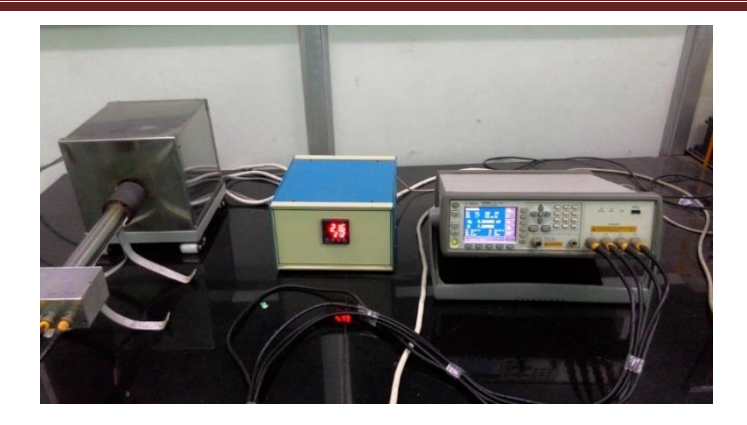


**Figure 3.4.** Photograph of the LCR meter used in this work.

Room temperature polarization behavior of the samples was studied by applying an electric field (1 Hz frequency) strength in the range -1.6-1.6 kV/cm using a polarization tester (Radiant Technology Inc Premier II, Model 2835D Pan American Fwy NE, **Fig. 3.5**).



**Figure 3.5.** Photograph of the P-E hysteresis measuring instrument used in this work.

### References

- [1] Hummers WS, Offeman RE. Preparation of graphitic oxide. J Am Chem Soc 1958;80 (6):1339.
- [2] Titelman GI, Gelman V, Bron S, Khaflin RL, Cohen Y, Peled HB. Characteristics and microstructure of aqueous colloidal dispersions of graphite oxide. Carbon 2005;43(3):641-9.
- [3] Marcano DC, Kosynkin DV, Berlin JM, Sinitskii A, Sun Z, Slesarev A, Alemany LB, Lu W, Tour JM. Improved synthesis of graphene oxide. ACS Nano 2010;4(8):4806-14.
- [4] Yao J, Shen X, Wang B, Liu H, Wang G. In situ chemical synthesis of SnO<sub>2</sub>-graphene nanocomposite as anode materials for lithium-ion batteries. Electchem Commun 2009;11(10):1849-52.
- [5] Flahaut E, Peigney A, Laurent C, Marliere C, Chastel F, Rousset A. Carbon nanotube—metal—oxide nanocomposites: microstructure, electrical conductivity and mechanical properties. Acta Mater 2000;48(14):3803-12.

- [6] Wu ZS, Wang DW, Ren W, Zhao J, Zhou G, Li F, et al. Anchoring hydrous RuO<sub>2</sub> on graphene sheets for high performance electrochemical capacitors. Adv Funct Mater 2010;20(20):3595-602.
- [7] Jie L, Andrew GR, Hongjie D, Jason HH, Kelley BR, Peter JB, Adrian L, Terry I, Konstantin S, Chad BH, Fernando RM, Young-Seok S, T. Randall L, Daniel T, Richard ES. Fullerene pipes. Science 1998;280:1253-56.
- [8] Hamon MA, Chen J, Hu H, Chen Y, Itkis ME, Rao AM, Eklund PC, Haddon RC. Dissolution of single-walled carbon nanotubes. Adv Mater 1999;11(10):834-40.
- [9] Cha SI, Kim KT, Arshad SN, Mo CB, Hong SH. Extraordinary strengthening effect of carbon nanotubes in metal matrix nanocomposites processed by molecular-level mixing. Adv Mater 2005;17(11):1377-81.
- [10] Kim KT, Eckert J, Liu G, Park JM, Lim BK, Hong SH. Influence of embedded carbon nanotubes on the thermal properties of copper matrix nanocomposites processed by molecular-level mixing. Scr Mater 2011;64:181-4.
- [11] Suslick KS. Sonochemistry. Science 1990;247(4949):1439-45.
- [12] Suslick KS, Flannigan DJ. Inside a collapsing bubble: Sonoluminescence and the conditions during cavitation. Annu Rev Phys Chem 2008;59(26):659-683.
- [13] Suslick KS, Choe SB, Cichowlas AA, Grinstaff MW. Sonochemical synthesis of amorphous iron. Nature 1991;353:414-6.
- [14] Zhu JJ, Xu S, Wang H, Zhu JM, dChen HY. Sonochemical synthesis of CdSe hollow spherical assemblies via an in-situ template route. Adv Mater 2003;15(2):156-9.
- [15] Gao T, Wang T. Sonochemical synthesis of SnO<sub>2</sub> nanobelt/CdS nanoparticle core/shell heterostructures. Chem Commun 2004;2558-9.
- [16] Hasin P, Wu Y. Sonochemical synthesis of copper hydride (CuH). Chem Commun 2012;48:1302-4.
- [17] Doktycz SJ, Suslick KS. Interparticle collisions driven by ultrasound. Science 1990;247:1067-9.
- [18] Prozorov T, Prozorov R, Suslick KS. High velocity interparticle collisions driven by ultrasound. J Am Chem Soc 2004;126(43):13890-1.
- [19] Bandyopadhyaya R, Roth EN, Regev O, Rozen RY. Stabilization of individual carbon nanotubes in aqueous solutions. Nano Lett 2002;2(1):25-28.

# **Chapter 4** Results and Discussion

#### 4.1 CuO decked FLG

#### 4.1.1 Structural, morphological, and phase analysis

X-ray diffractogram pertaining to graphite (the starting material) is shown in **Fig. 4.1(a)**. The major diffraction peak at  $2\theta = 26.5^{\circ}$  corresponds to (002) graphite. This corresponds to an interplanar spacing (d spacing) of 0.34 nm. The sharpness of the peak indicates high order of crystallinity (or stacking of numerous graphene layers along the thickness axis) of graphite. The acid treatments on the graphite in IHM oxidize graphite by attaching functional groups like aldehyde (CHO), epoxy (ethers), hydroxyl (-OH), carbonyls (C=O), and carboxylic (-COOH—) etc., at appropriate surfaces and edges of graphite to yield GO. Since GO is a result of intercalation in graphite, the d spacing is bound to increase. X-ray diffractogram (Fig. **4.1(b)**) pertaining to GO shows that the (002) graphite diffraction peak has not only shifted towards lower 20 values indicating an increase in d spacing along the thickness axis but also broadened indicating reduction in the structural quality due to oxidation. The (002) graphite diffraction peak is at  $2\theta = \sim 9.71^{\circ}$  (corresponding to a d spacing of 0.91 nm). The full width at half maximum (FWHM) of the (002) graphite diffraction peak pertaining to the starting material is ~0.36° whereas FWHM value of the same diffraction peak pertaining to GO is ~2.17°. The considerable increase in FWHM clearly indicates a decrease in crystallinity of GO in terms of stacking constituted by less number of graphene layers in the case of GO when compared with graphite [1]. XRD pattern pertaining to FLG is also shown in Fig. **4.1(b)**. It is clearly observed that (002) peak in the case of FLG is shifted towards higher  $2\theta$ values indicating a decrease in interplanar spacing due to the reduction of oxide functional groups or vaporization of intercalated water molecules [2,3]. After Lorentzian fit, (002) peak is observed at  $2\theta = 24.36^{\circ}$  (corresponding d spacing is ~0.363 nm). The d spacing is slightly greater than the theoretical d spacing, which is ~0.34 nm. This is attributed to the presence of few residual epoxy and hydroxyl groups even after thermal exfoliation [4,5]. Drastic change in FWHM of (002) peak can also be clearly observed from Fig. 4.1(b). FWHM value of (002) peak pertaining to FLG is 5.9°. This value is greater than FWHM of (002) peak in GO and much greater than graphite's (002) peak. This indicates further decrease in thickness (t) which is estimated from Debye Scherrer's formula [6] (given in section 3.2). The thickness of each FLG is found to be ~13.57 Å and therefore the number of layers (t/d) in each FLG is estimated as ~4.

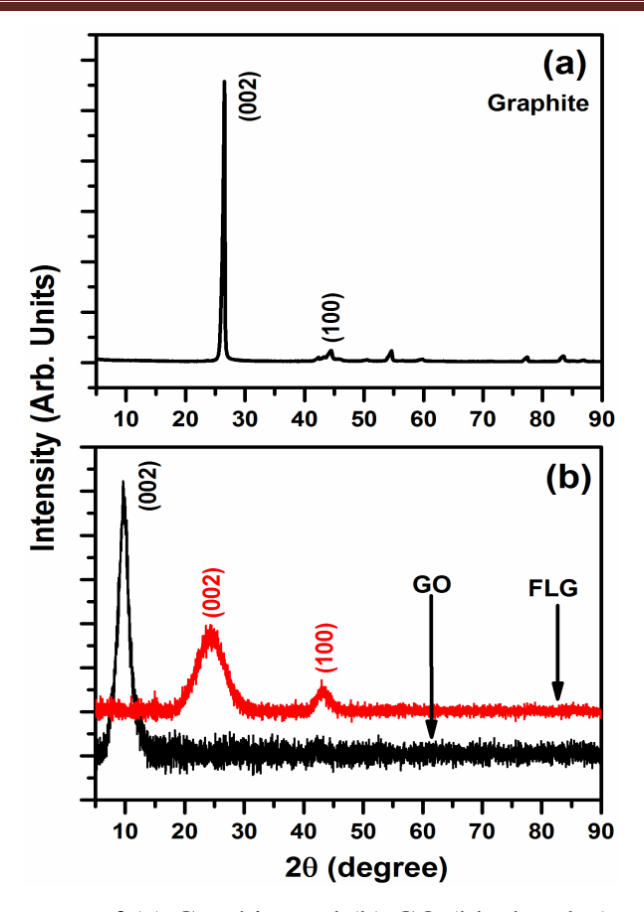


Figure 4.1. XRD patterns of (a) Graphite and (b) GO (black color) and FLG (red color).

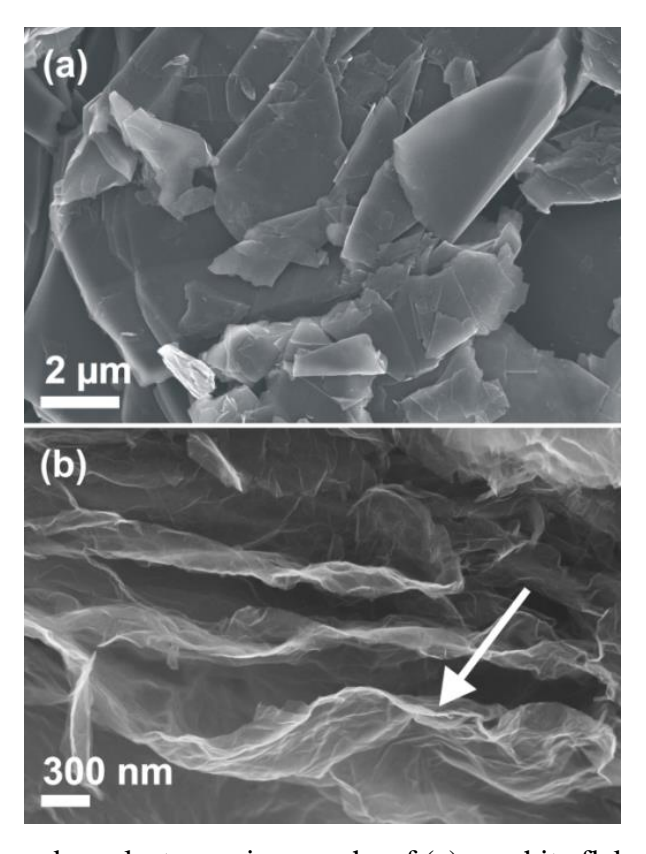
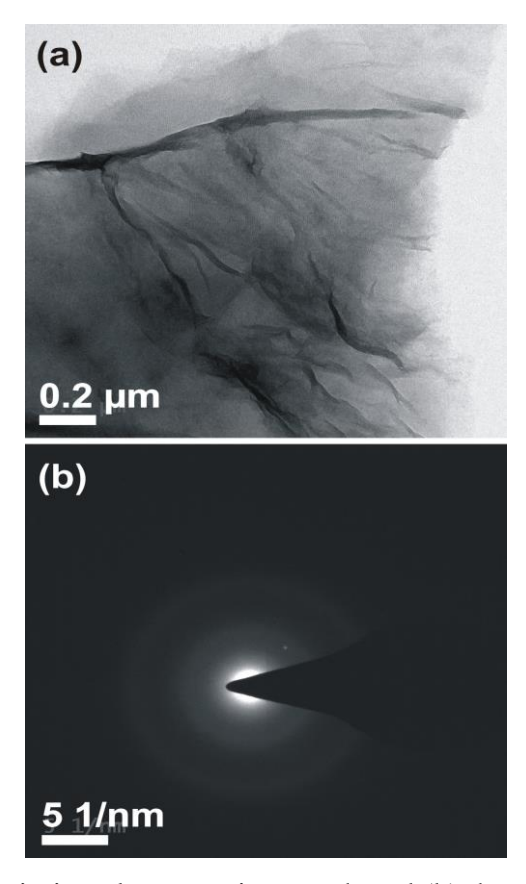


Figure 4.2. Secondary electron micrographs of (a) graphite flakes and (b) FLG.

#### **Results and Discussion**

SE micrographs of graphite flakes and FLG are shown in Fig. 4.2 (previous page). It can be observed that graphite flakes are thick (in the order of micrometers) as shown in Fig. 4.2(a). After acid treatment and thermal reduction, the reduced GO material (FLG) consists of randomly aggregated, thin, crumpled sheets closely associated with each other and forming a disordered solid as observed from the respective micrograph (Fig. 4.2(b)). The folded regions of the FLG (Fig. 4.2(b)) sheets are found to have an average thickness of few nm. The absence of charging during the FESEM imaging indicates that the material constitutes a network of graphene-based sheets which are electrically conductive. Formation of FLG can be clearly concluded from the SE micrographs and discussed XRD analysis. Further support for the same is given by TEM analysis. Fig. 4.3(a) shows transmission electron micrograph of FLG and the corresponding diffraction pattern is shown in **Fig. 4.3(b)**. As observed from Fig. 4.3(a), FLG is transparent to the electron beam and is folded at several regions. The diffused ring electron diffraction pattern resembles that of an amorphous material indicating stacking of only few graphene layers in FLG. These observations are complemented well with XRD observations. Hence, the discussion made till this point clearly indicates that each FLG synthesized from GO using IHM contains only a few layers of graphene.



**Figure 4.3.** (a) Transmission electron micrograph and (b) the corresponding electron diffraction pattern of FLG.

#### **Results and Discussion**

The product of the third step involved in the synthesis of CuO decked FLG by MLM consists a mixture of CuO and Cu<sub>2</sub>O phases. This is evident from the XRD patterns shown in **Fig 4.4**. Fig. 4.4(a) represents the diffraction pattern obtained from the material consisting of CuO/Cu<sub>2</sub>O phases. (110), (111) and (200) diffraction peaks represented in red color correspond to cubic Cu<sub>2</sub>O and the remaining diffraction peaks correspond to monoclinic CuO. Figs. 4.4(b) and (c) correspond to diffraction patterns obtained from CuO/Cu<sub>2</sub>O-0.1G and CuO/Cu<sub>2</sub>O-0.2G samples, respectively. In these patterns, (002) FLG diffraction peak at 26.4° (represented in blue color) can be clearly observed. In these patterns, the presence of both CuO and Cu2O in the samples is also evident. It is also evident from the diffraction patterns corresponding to CuO/Cu<sub>2</sub>O-0.1G and CuO/Cu<sub>2</sub>O-0.2G samples that the diffraction peaks corresponding to Cu<sub>2</sub>O are intense indicating that Cu<sub>2</sub>O phase is dominant. In order to obtain CuO decked FLG, CuO/Cu<sub>2</sub>O-0.1G and CuO/Cu<sub>2</sub>O-0.2G samples were heated [7-10] at 400 °C in ambient atmosphere for 8 h. Due to thermal oxidation, cuprous oxide (Cu<sub>2</sub>O) was converted into cupric oxide (CuO) in the samples following the reaction  $Cu_2O + \frac{1}{2}O_2 \rightarrow$ 2CuO. This is evidenced by a color change from brick red (Cu<sub>2</sub>O) to black (CuO). Pure CuO was also obtained in a similar manner from the material consisting of CuO and Cu<sub>2</sub>O phases.

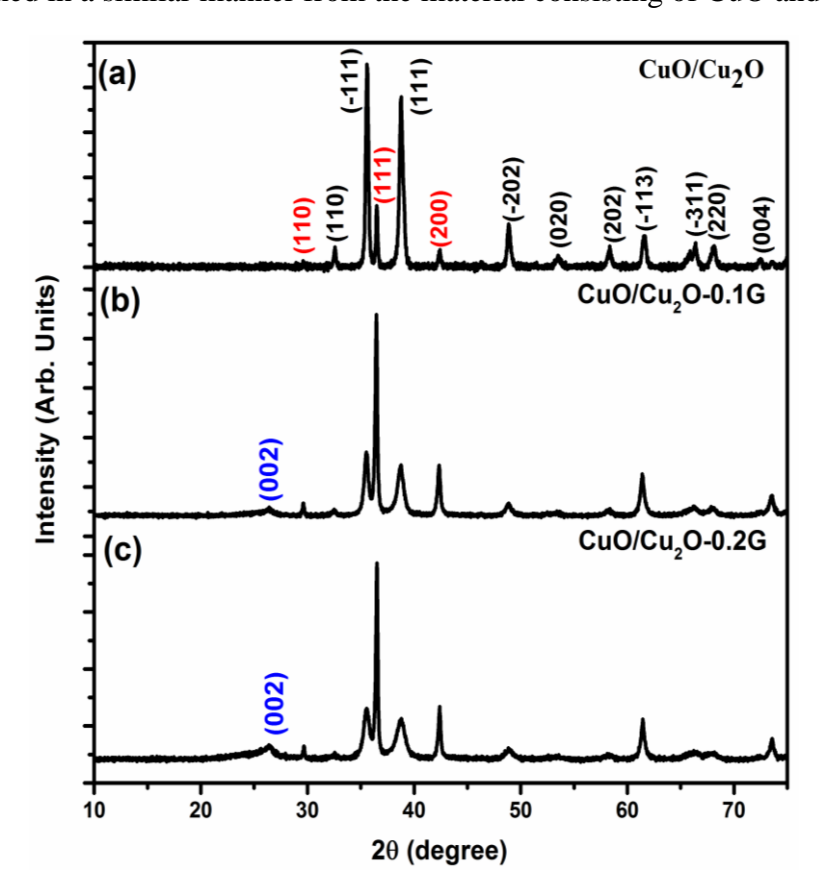


**Figure 4.4.** XRD patterns of (a)  $CuO/Cu_2O$  containing material, (b)  $CuO/Cu_2O$ -0.1G and (c)  $CuO/Cu_2O$ -0.2G.

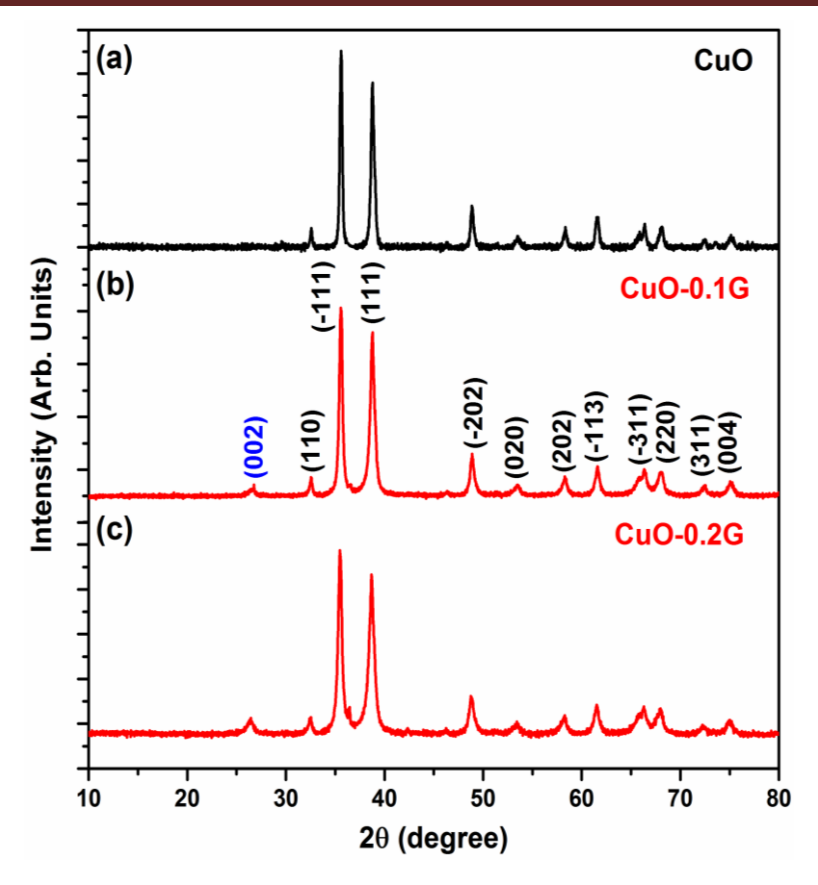
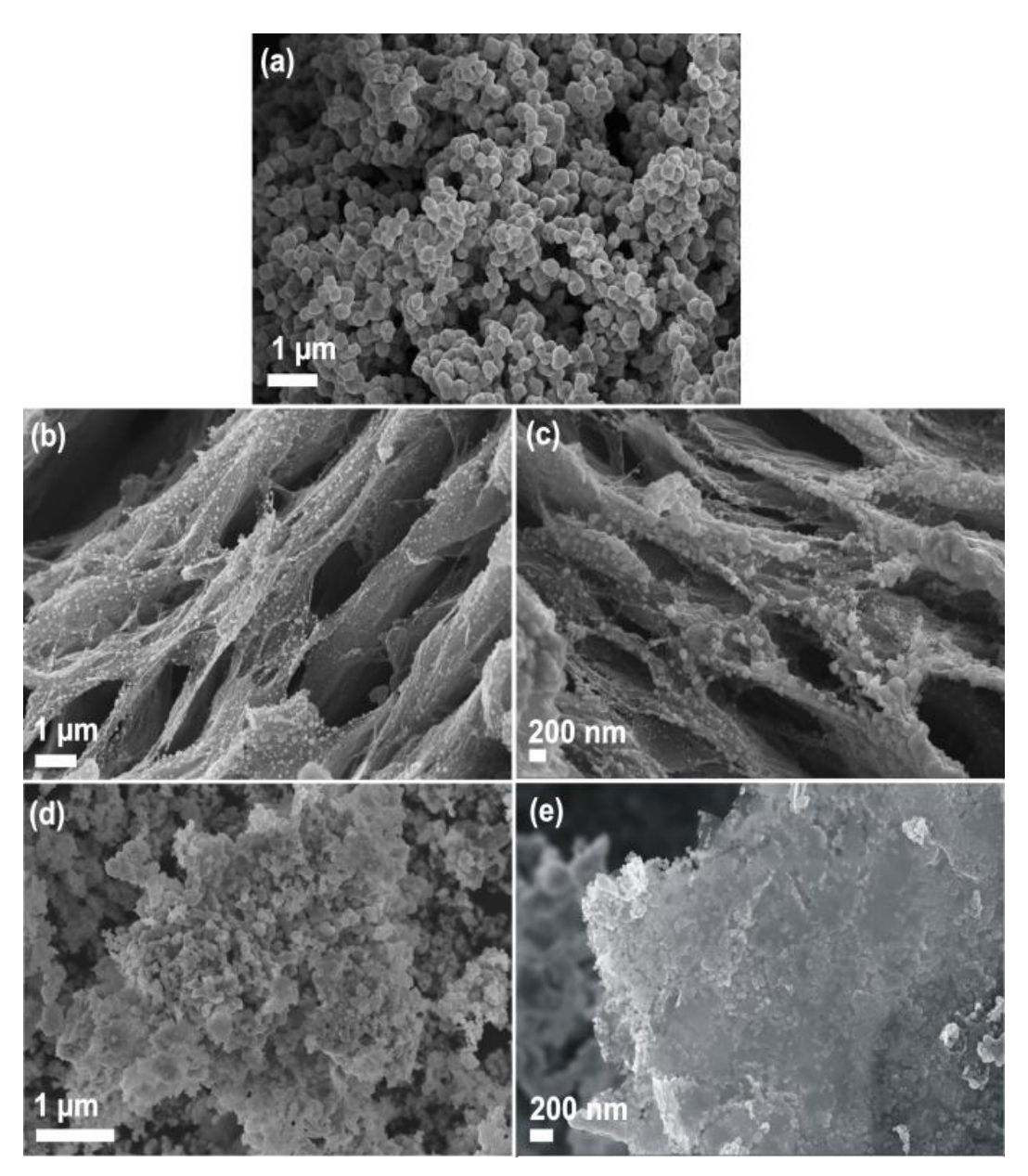


Figure 4.5. XRD patterns of (a) CuO, (b) CuO-0.1G and (c) CuO-0.2G.

The above discussed phase changes are evident from the corresponding XRD patterns shown in Fig. 4.5. In all the patterns the diffraction peaks corresponding to Cu<sub>2</sub>O are absent. It is also evident from Figs. 4.5(b) and (c) that FLG is intact in the samples now named as CuO-0.1G and CuO-0.2G. Intactness of FLG was further confirmed by TEM analysis. In the XRD patterns (Figs. 4.5(b) and (c)) of CuO-0.1G and CuO-0.2G samples, the diffraction peaks corresponding to CuO are broader and lower in intensity when compared to CuO diffraction peaks shown in Fig. 4.5(a). This suggests that CuO-0.1G and CuO-0.2G samples contain small CuO particles with relatively poor crystallization. The presence of some functional groups on FLG hinders the growth and crystallization of metal oxide nanoparticles and renders them with irregular shapes [11]. SE micrographs of CuO, CuO-0.1G, and CuO-0.2G samples are shown in Fig. 4.6. CuO sample has feature sizes (Fig. 4.6(a)) is the order of few tens of nm. In the case of CuO decked FLG sample (CuO-0.1G), CuO nanoparticles are uniformly decked on both sides of the graphene nanosheets as shown in Figs. 4.6(b) and (c). Same is the case with CuO-0.2G (Figs. 4.6(d) and (e)). Plane view of transmission electron micrographs (Figs. 4.7(a), (b), (d) and (e)) supports the SEM observations. Figs. 4.7(c) and (f) show the electron diffraction obtained from CuO-0.1G and CuO-0.2G, respectively. The

## **Results and Discussion**

diffraction rings indicate the presence of polycrystalline material in the sample. The rings are indexed to CuO. High-resolution transmission electron micrographs (**Figs. 4.7(c**) and (**f**)) further support the presence of CuO. They show (111) CuO lattice fringes with d spacing of ~0.232 nm (indicated by arrow marks in **Fig. 4.7(e**)). These observations complement well with XRD results. **Figs. 4.7(b**) and (**e**) confirm that the CuO crystallites are few nm in size.



**Figure 4.6.** (a) SE micrographs of CuO particles. (b) & (c) low and enhanced magnification SE micrographs, respectively of CuO-0.1G and (d) & (e) low and enhanced magnification SE micrographs, respectively of CuO-0.2G.

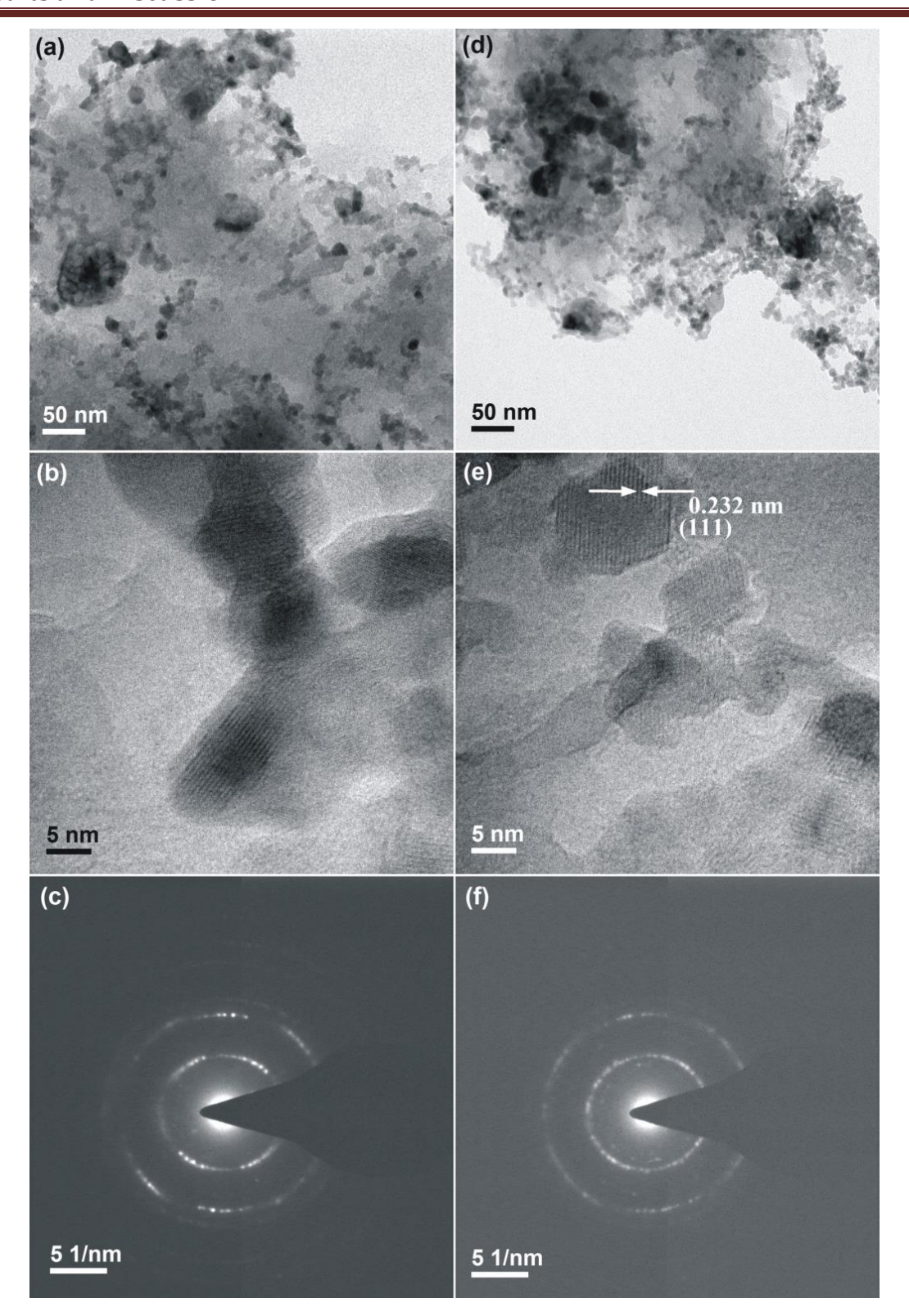


**Figure 4.7.** TEM images and corresponding diffraction patterns of CuO decked FLG. (a), (b), and (c) are low-resolution image, high-resolution image and diffraction pattern of CuO-0.1G, respectively whilst (d), (e), and (f) are low-resolution image, high-resolution image and diffraction pattern of CuO-0.2G, respectively.

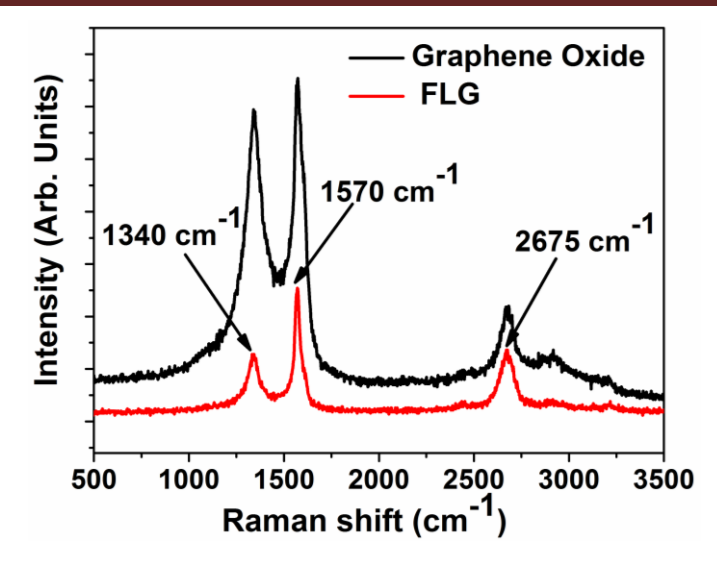


Figure 4.8. Raman spectra of GO (black color) and FLG (red color).

Raman spectra obtained from GO and FLG are shown in Fig. 4.8. The Raman spectrum pertaining to GO displays the prominent G band at ~1570 cm<sup>-1</sup> and the D band at ~1340 cm<sup>-1</sup>. It displays the 2D band at ~2675 cm<sup>-1</sup>. In the Raman spectrum corresponding to FLG (marked in red colour), the G band is broader and lower in intensity when compared to the G band corresponding to GO at same integration time of 5 sec and also the same focal conditions. Besides this, the 2D band is also lower in intensity and broadened in the case of FLG. The broadening is more symmetric indicating a better formation of FLG [12,13]. This is supported by a reduction in the size of the in-plane sp<sup>2</sup> domains with an increase in I<sub>2D</sub>/I<sub>G</sub> ratio (0.49) compared to the same ratio in GO (0.27). This change suggests a decrease in the average size of the sp<sup>2</sup> domains upon reduction of GO resulting in the formation of FLG [14]. To obtain quantitative data, the G band in the case of both GO and FLG was peak fitted using double peak-Lorentz function. G band in the case of FLG has intensity and FWHM values of ~107 counts and 38 cm<sup>-1</sup>, respectively. G band in the case of GO has intensity and FWHM values of ~240 counts and 68.5 cm<sup>-1</sup>, respectively. 2D band was also peak fitted using Lorentz function. In the case of both GO and FLG was peak fitted using double peak-Lorentz function. 2D band in the case of FLG has intensity and FWHM values of ~54 counts and 87.6 cm<sup>-1</sup>, respectively. 2D band in the case of GO has intensity and FWHM values of ~58.8 counts and 76.4 cm<sup>-1</sup>, respectively. 2D/G intensity ratio in the case of FLG is 0.50 whilst it is only 0.22 in the case of GO. The major Raman features of graphene and graphite are G band and 2D band (~2675 cm<sup>-1</sup>). The 2D band originates from a two-phonon double resonance in Raman scattering process [15]. The 2D band is also denoted as G'. It is the second most prominent band of graphite samples after the G band. The obvious difference between the

Raman features of FLG and graphite is 2D band. As the 2D band origins from the two phonons double resonance process, it is closely related to the band structure of graphene layers [12,13]. Broadening of the 2D band is related to the splitting of the electronic band structure of multi-layer graphene. A detailed discussion on how the multi Raman peak structure of 2D band obtained from the stacking of two or more graphene layers is related to the dispersion of  $\pi$  electrons and has already been reported [16]. Unfortunately, the 2D band differences between two and few layers of graphene sheets are not obvious and unambiguous in the Raman spectra. As number of layers increase, the intensity of G band increases while 2D band loses its symmetry. The Raman spectra obtained from CuO-0.1G and CuO-0.2G samples are shown in **Fig. 4.9**. in both the cases, the typical bands corresponds to the presence of FLG (as discussed above) are shifted towards higher wavenumbers. This is due to the decking of CuO on FLG. It is also observed that the intensity of peaks corresponding to FLG is intense in the case of the CuO-0.2G sample due to the presence of more FLG. The Raman band at ~485 cm<sup>-1</sup> could be attributed to the presence of CuO [17-19].

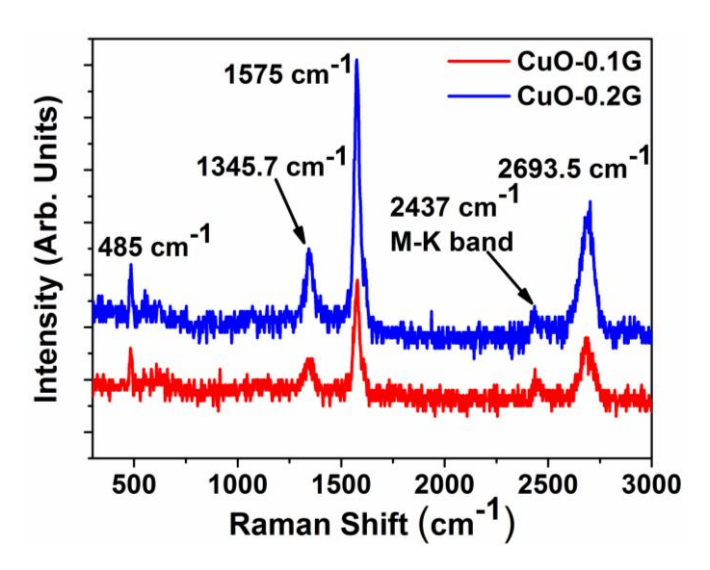
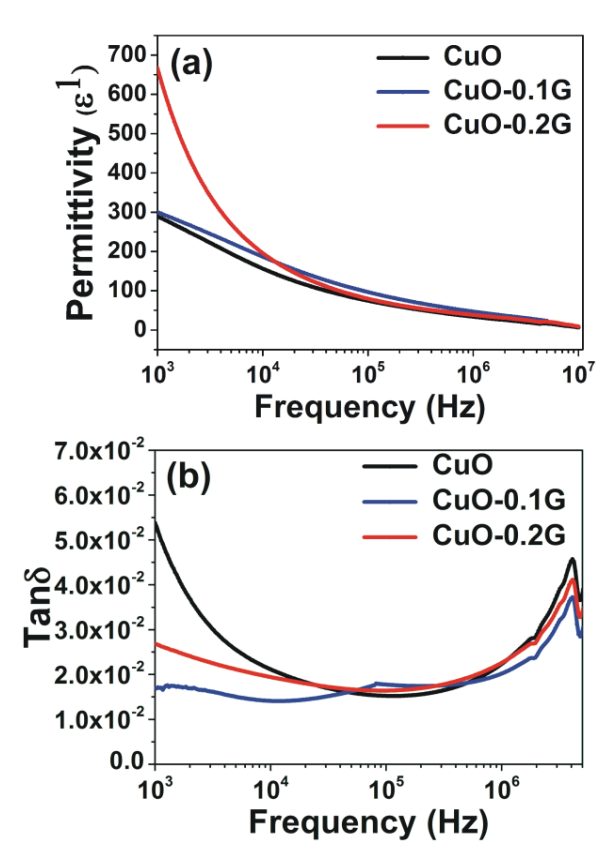


Figure 4.9. Raman spectra of CuO-0.1G (red colour) and CuO-0.2G (blue colour).

#### 4.1.2 Dielectric properties

Dielectric permittivity and tangent loss (as a function of frequency) of CuO and CuO decked FLG (CuO-0.1G & CuO-0.2G) are shown in **Fig. 4.10**. Previous measurements with regards to dielectric permittivity  $\varepsilon'$  of CuO showed surprisingly low value of ~25 for polycrystalline sample, 3-4 for insulating single crystal and 3000 for semiconducting single crystal. Interestingly, CuO in the present work showed high dielectric permittivity of ~289 at 1 kHz for polycrystalline CuO. This value is higher compared to those previously reported [20]. The high dielectric permittivity of CuO is an indication of increased conductivity and that may be

due to the presence of trace Cu<sup>3+</sup> impurities which can make hole hopping between Cu<sup>3+</sup> and Cu<sup>2+</sup> followed by strong interaction with lattice and spin [20]. The dielectric permittivity was significantly increased by addition of FLG. The dielectric permittivity ( $\varepsilon'$ ) of CuO-0.1G composite shows nearly 10% higher ( $\varepsilon' = 318$ ) than CuO ( $\varepsilon' = 289$ ), while CuO-0.2G composite shows 2.3 ( $\varepsilon' = 667$ ) times higher value than that of CuO at 1 kHz shown in **Fig 4.10(a)**. It can also be observed that as frequency increases, the dielectric permittivity value decreases indicating Debye type of polarization in the case of CuO decked FLG samples. This is also true for the CuO synthesized in this work. The increase in the permittivity at 1 kHz for CuO-0.1G and CuO-0.2G composites can be ascribed to the formation of a continuous conductive pathway throughout the medium between FLG sheets. The tangent loss (tan  $\delta = \varepsilon''/\varepsilon'$ ) as a function of frequency in shown in **Fig. 4.10(b)**. CuO shows relatively high loss value compared to that of CuO-0.1G and CuO-0.2G samples. That is, the formation of CuO-0.1G and CuO-0.2G reduces the dielectric loss indicating that the conducting mechanism has changed with the formation of these composites. This suggests that there is strong interfacial polarization occurring in CuO-0.1G and CuO-0.2G samples due to percolation of graphene (FLG) sheets as well as homogeneous distribution of CuO.



**Figure 4.10.** (a) Dielectric permittivity ( $\varepsilon'$ ) and (b) tangent loss (tan  $\delta$ ) of CuO (black color line), CuO-0.1G (blue color line) and CuO-0.2G (red color line) samples.

**Fig. 4.11(a)** shows the increase in the AC conductivity with increase in applied frequency. The AC conductivity values of CuO, CuO-0.1G and CuO-0.2G samples at 1 kHz are 4.5 × 10<sup>-7</sup>, 8.5×10<sup>-7</sup>, and 9.9×10<sup>-7</sup> S/m indicating an insulating behavior (inset figure in **Fig. 4.11(a)**). At higher frequency, CuO-0.1G and CuO-0.2G samples showed semiconducting nature. The AC conductivity values of CuO, CuO-0.1G, and CuO-0.2G are 3.84×10<sup>-4</sup>, 4.03×10<sup>-4</sup> and 4.46×10<sup>-4</sup> S/m, respectively at 10 MHz. Such an increase in conductivity by the formation of this composite at a higher frequency might be due to (i) good conductive particle-to-particle interfaces, which often determines the overall percolation conductivity, (ii) a very dense conductive network with many cross-linked connections and (iii) possible ionic channels of charge transfer across the sample.

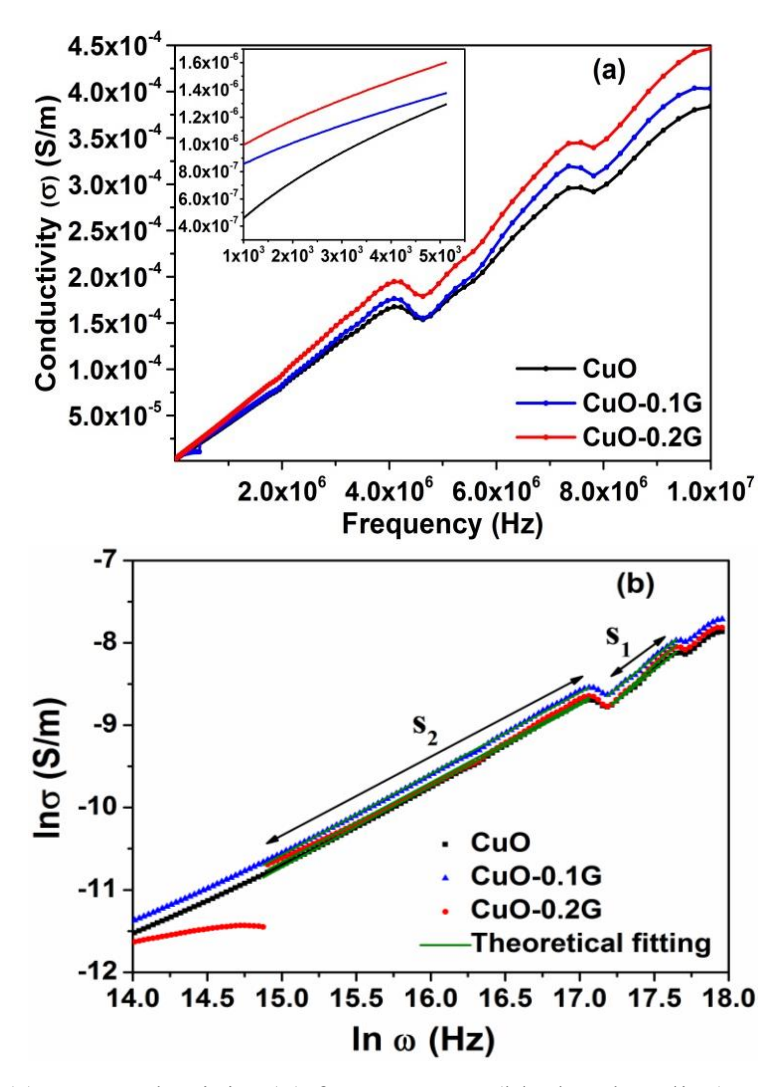


**Figure 4.11.** (a) AC conductivity (σ) for pure CuO (black colour line), CuO-0.1G (blue colour line), CuO-0.2G (red colour line) shown as a function of frequency. (b) Theoretical fitting using Jonscher's power law equation.

Several mechanisms are available that explain the dependence of AC conductivity on either frequency or temperature. Frequency activated increase of conductivity follows the Jonscher's Universal power law given by [21]

$$\sigma(\omega) = \sigma_{dc} + A\omega^{s}$$
 ..... (Equation 4.1)

where  $\sigma_{dc}$  is the dc conductivity, A is the pre-exponential factor which depends on temperature,  $\omega$  is the frequency and s is a dimensionless exponent. The values of A and s are extracted by fitting the experimental data with the above equation as shown in **Fig. 4.11(b)**. Fitting with Jonscher's Universal power law (**Eq. 4.1**) gave good fitting parameters with best parameter fit R<sup>2</sup> in the range 0.9962-0.9993. The AC conductivity increased linearly from frequencies above 2 MHz whereas in the lower frequencies it increased nonlinearly. The values of exponents  $s_1$  and  $s_2$  and "A" for all the three samples in the frequency ranges  $2.9 \times 10^7$ - $4.6 \times 10^7$ Hz and  $2.7 \times 10^6$ - $2.5 \times 10^7$ Hz are given in **Table 4.1**. In the case of CuO-0.2G sample, a discontinuity/jump has been observed (**Fig. 4.11(b)**), which is most plausibly due to a sudden increase in the AC conductivity. However, the fitting in the region after the discontinuity has only been considered for analysis.

The value of s is close to 1 in the considered frequency range. The exponent value below 1 indicates a hopping mechanism involving the electrons [21]. Several theoretical models explain the behavior of ac conductivity based on frequency and temperature. Basically, two distinct processes of relaxation mechanisms occur: Quantum mechanical tunnelling (QMT) model in which the AC conductivity comes from the tunnelling of an electron through a barrier separating localized states giving the temperature independent value of s [22]. Secondly, Correlated Barrier Hopping (CBH) model in which the AC conductivity is dependent on temperature [23]. Since AC conductivity in the present case is taken at room temperature, CBH model has not been used. According to QMT, ac conductivity is given as,

$$\sigma_{ac} = BK_B T[N(E_f)]^2 \alpha^{-5} \omega \left[ ln \left( \frac{1}{\omega \tau_o} \right) \right]^4 \dots (Equation 4.2)$$

where B is the dimensionless constant equals to  $\pi^4/24$ ,

 $K_B$  is the Boltzmann constant

T is the temperature

 $N(E_f)$  is the density of states near Fermi level

 $\alpha$  is the inverse localization length for electron wave function

 $\omega$  is the frequency, and  $\tau_{\alpha}$  is the characteristic relaxation time.

The frequency exponent s for  $\sigma(\omega)$  in this model is given by,

$$s = 1 - \frac{4}{\ln(\omega \tau_{o})}$$
 (Equation 4.3)

Thus, according to QMT model, the frequency exponent s is temperature independent and frequency dependent. The experimental data was fitted with **Eq. 4.3** with  $\omega$  as variable and the values of s are derived. For typical values of parameters namely  $\tau_o = 2.344\text{E-}7$  and  $\omega = 3.09\text{E7}$  "s" becomes ~0.98 (± 0.05). With  $\tau_o = 2.344\text{E-}7$  and  $\omega = 1.83\text{E7}$  exponent "s" becomes ~0.80 (± 0.06). Here  $\tau_o$  has been calculated from **Fig. 4.11(b)** ( $\tau_o = 1/\omega_{\text{max}}$ ). It is noted that the exponent values of s, are almost similar for the three samples and are similar to those predicted by theory and are shown in **Table 4.1**.

**Table 4.1.** Comparison of parameters for CuO, CuO-0.1G, and CuO-0.2G from Jonscher's power law and Quantum Mechanical Tunnelling (QMT) model.

Sample	Jonscher's Universal Power Law				Quantum Mechanical Tunnelling (QMT)	
	$s_1$	$S_1$ $S_2$ $A_1$ $A_2$		S <sub>1</sub>	S2	
	$2.9 \times 10^{7}$ -	$2.7 \times 10^{6}$ -				
	$4.6 \times 10^{7} \text{Hz}$	$2.5 \times 10^{7} \text{Hz}$				
CuO	0.98 (±0.05)	$0.80(\pm 0.06)$	9.7×10 <sup>-12</sup>	$1.46 \times 10^{-15}$	$0.98(\pm 0.05)$	$0.80(\pm 0.06)$
CuO-0.1G	$0.98(\pm 0.05)$	0.81(±0.06)	8.3×10 <sup>-12</sup>	9.8×10 <sup>-16</sup>	$0.98(\pm 0.05)$	0.81(±0.06)
CuO-0.2G	$0.96(\pm 0.05)$	$0.67(\pm 0.06)$	1.14×10 <sup>-11</sup>	4.9×10 <sup>-17</sup>	$0.98(\pm 0.05)$	$0.67(\pm 0.06)$

Cole-Cole plots of CuO, CuO-0.1G, and CuO-0.2G samples are shown in **Fig. 4.12** (next page). All the samples show semi-circle plots. The intercept of a semi-circle on Z¹ axis is the grain boundary resistance. From the Cole-Cole plots, it can be observed that the CuO shows high resistance (0.34×10<sup>5</sup> Ohm) compared to graphene/CuO composite (0.29×10<sup>5</sup> Ohm in the case of CuO-0.1G and 0.22×10<sup>5</sup> Ohm in the case of CuO-0.2G) showing a clear enhancement in conductivity in CuO-graphene composite compared to CuO [24]. Even though there is enhancement in the conductivity, the conductivity values of the composites are low owing to the presence of FLG. Conductivity values can be expected to be high if monolayer graphene is used instead of FLG. Further, it can be observed that with increase in the FLG content in the composite, grain boundary contribution to the conductivity is decreasing. The reason for this important behavior must be good conduction between particle-to-particle interfaces.

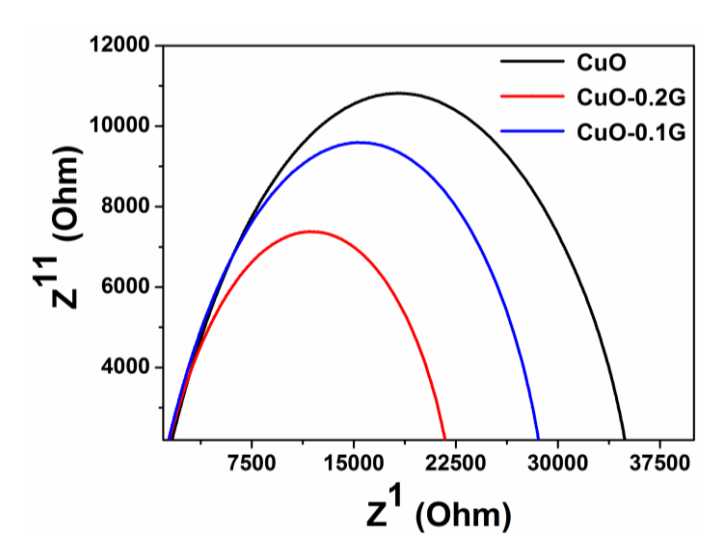


**Figure 4.12.** Cole-Cole plots of CuO (black colour line), CuO-0.1G (blue colour line) and CuO-0.2G (red colour line) samples.

#### 4.2 ZnO decorated r-GO

#### 4.2.1 General comments

The choice of working on ZnO-r-GO composite system is based on the literature [25,26] and also owing to the fact that ZnO has low dielectric permittivity; therefore its combination with r-GO offers a great opportunity to understand interfacial polarization, if any. It has been theoretically elucidated that the interface between ZnO and type of graphene plays a vital role in controlling the polarization behavior of the composite [25,26]. It was therefore worthwhile to understand the dielectric behavior of ZnO-graphene composites through experimentation. In this context, there are some experimental research works on ZnO-graphene composites, which have concentrated on various aspects related to their synthesis, electrical properties, photoluminescence and photovoltaic efficiency [27-31]. Herein, ZnO decorated r-GO composites are synthesized using MLM technique, which enables effective and homogenous distribution of metal oxide particles on the surfaces of r-GO sheets which in turn results in an enhanced synergic interaction between the constituents. r-GO can be typically modified to possess residual defects and attached functional groups (epoxides, hydroxides, and carboxylic groups), which are useful in participating in chemical reactions with the metal ions of the precursor salts to form metal oxides with suitable interfaces. This in turn can prompt energy transition from contiguous states to the Fermi level and introduce defect- related polarization relaxation and functional group-related electronic dipole relaxation under the influence of an external electric field. As mentioned previously, the type of polarization depends upon the

external field's frequency, while the dielectric constant is a function of polarizability. Space-charge polarization is observed up to ~ $10^3$  Hz, while dipolar or orientation (this is also depends on temperature), ionic and electronic polarizations are observed in the ranges  $10^3$ - $10^8$ ,  $10^8$ - $10^{13}$  and  $10^{13}$ - $10^{16}$  Hz, respectively. In this context, it is well-known that semiconducting or insulating composite systems exhibit a strong Maxwell-Wagner polarization [32]. ZnO-r-GO composites could be one such system, therefore the influence of interfaces in this composite on its dielectric properties, such as dielectric permittivity ( $\epsilon'$ ), tangent loss (tan  $\delta$ ), AC conductivity ( $\sigma$ ) and dielectric relaxation (electric modulus), are elucidated in the section 4.2.3. In order to understand the interfacial polarization in ZnO-r-GO composites, the electric modulus formalism has been used. The charge storage capability of the ZnO-r-GO composites in comparison to ZnO is assessed so as to comprehend the composite's usefulness as an active material (i.e., with high dielectric constant and low losses) in charge storage capacitors [33]. Electric modulus (M") formalism in ZnO/r-GO composites as well as in ZnO is also discussed for understanding the interfacial polarization.

# 4.2.2 Structural, morphological, and phase analysis

Firstly, the characteristics of r-GO that was used in the synthesis of ZnO decorated r-GO nanocomposites will be presented. X-ray diffractrogram pertaining to graphite (the starting material) is shown in Fig 4.13(a). The sharp diffraction peak at  $2\theta = 26.5^{\circ}$  corresponds to (002) graphite planes with a d spacing of 0.34 nm (indicating staking of numerous graphene layers). After acid treatment, graphite undergoes oxidation due to attachment of functional groups like hydroxyl (-OH), epoxy (ethers), carbonyls (C=O), carboxylic (-COOH-), and aldehyde (CHO) etc., at appropriate surfaces and edges of it. Due to the attachment of functional groups, the d spacing in GO is expected to be larger in comparison to graphite. Fig **4.13(b)** exactly depicts the same. The diffraction peak at  $2\theta \sim 12.67^{\circ}$  corresponds to (002) diffracting planes in GO with a d spacing of 0.69 nm. Moreover FWHM of this peak is ~1.69° which is much greater than that in graphite (~0.36°) indicating that GO is constituted by less number of graphene layers. In the case of r-GO FWHM is much greater (~2.38°) than that in graphite indicating that r-GO is constituted by few graphene layers. XRD pattern of r-GO (**Fig. 4.13(b**)) clearly shows that (002) peak in the case of r-GO is at a greater  $2\theta$  value (~24.49°) indicating a decrease in the interplanar spacing [2,3]. The d spacing corresponding to this diffraction angle is ~0.363 nm which is greater than the theoretical d spacing (~0.34 nm) in graphite. This in turn confirms that few oxygen functional groups are still present in the case of r-GO [4,5]. Number of graphene layers in each r-GO was found to be  $\sim$ 9.

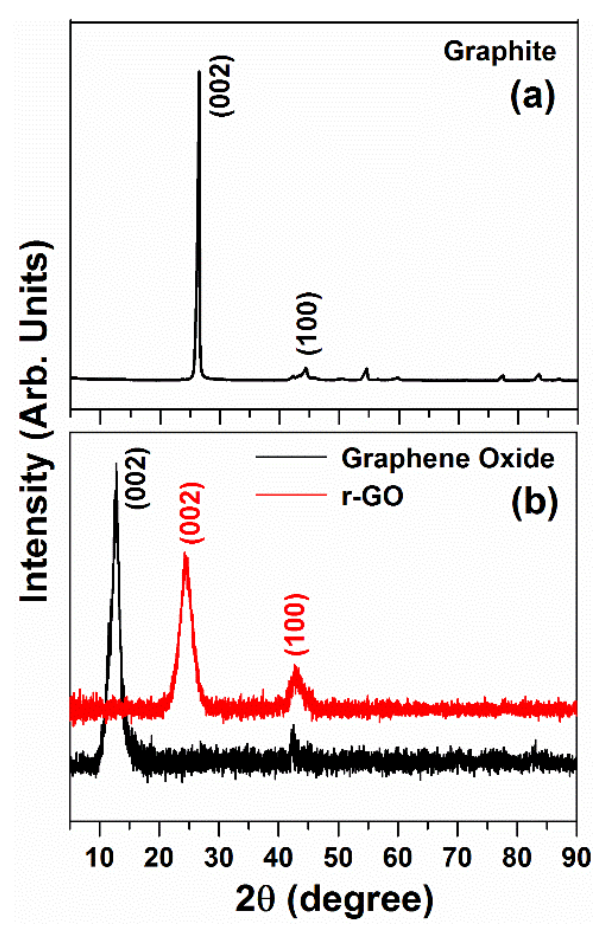


Figure 4.13. XRD patterns of (a) Graphite and (b) GO (black colour) and r-GO (red colour).

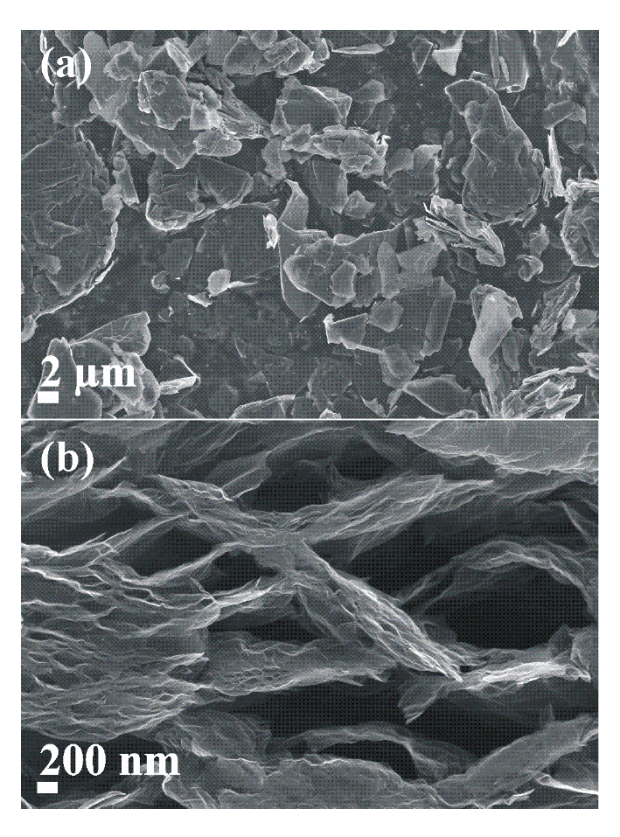


Figure 4.14. Secondary electron micrographs of (a) graphite flakes and (b) r-GO.

SE micrographs of graphite flakes and r-GO are shown in **Fig. 4.14** (previous page). **Fig. 4.14(a)** shows that graphite flakes are thick (in the order of micrometers). **Fig. 4.14(b)** shows that r-GO consists of randomly aggregated, thin, crumpled sheets closely associated with each other and forming a disordered solid. The folded regions of the r-GO (**Fig. 4.14(b)**) sheets are found to have an average thickness of few nm. Formation of r-GO can be clearly concluded from the SE micrographs which are also supported by the XRD analysis.

XRD patterns of ZnO and ZnO-r-GO nanocomposites are shown in **Fig. 4.15**. The diffraction peaks in the case of all the samples are well indexed (JCPDS 89-0510) to the planes in hexagonal ZnO. In the case of ZnO-0.2G and ZnO-0.3G samples, (002) diffraction peak (marked in blue color) at 26.4° indicates the presence of r-GO. This feature is absent in the case of ZnO-0.1G. This may be due to the complete coverage of r-GO sheets by ZnO nanoparticles and/or low content of r-GO in the sample. These reasons are supported by morphological analysis (**Fig. 4.16**). There is no peak shift in the peaks corresponding to r-GO in the composites. This indicates that ZnO nanoparticles are decorated on both sides and also on the edges of r-GO sheets but not in between (intercalation) the r-GO sheets. SE micrographs of ZnO and ZnO-0.2G composite are shown in **Fig. 4.17**. It is clearly observed in **Fig. 4.17(a)** that ZnO particles are few nm in size. **Fig. 4.17(b)** and **(c)** clearly show that the surface and cross-section of r-GO sheets are uniformly decorated by ZnO nanoparticles with an average size of few nm which is further confirmed by TEM analysis.

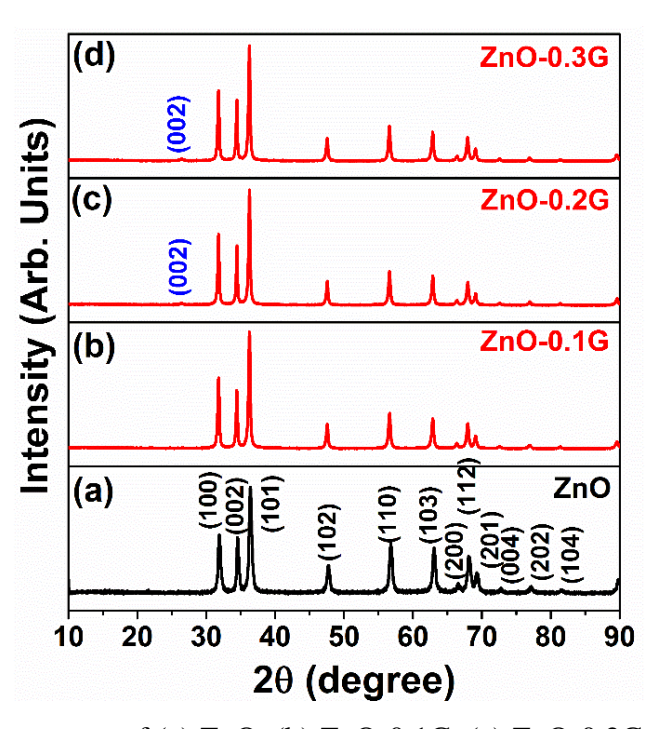


Figure 4.15. XRD patterns of (a) ZnO, (b) ZnO-0.1G, (c) ZnO-0.2G and (d) ZnO-0.3G.

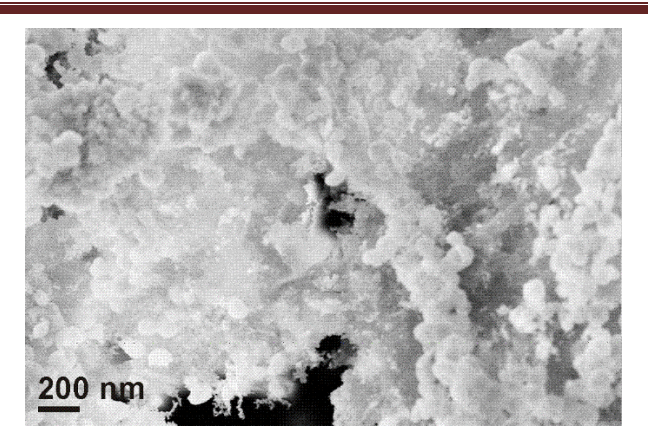
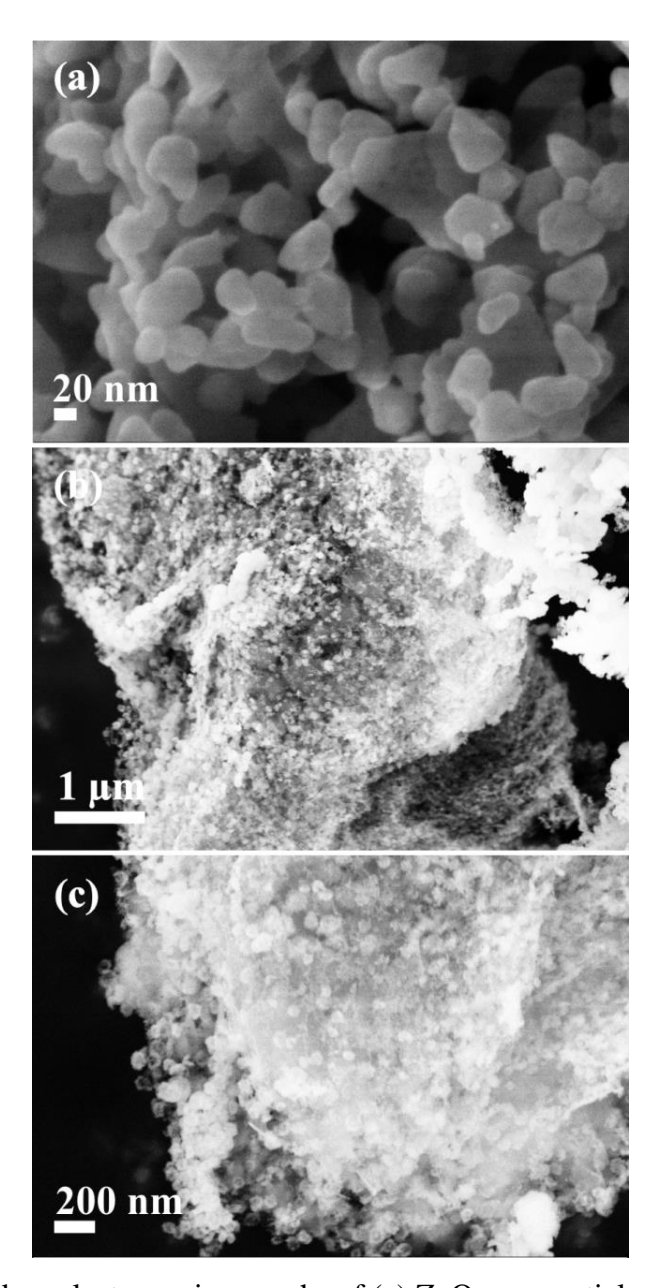
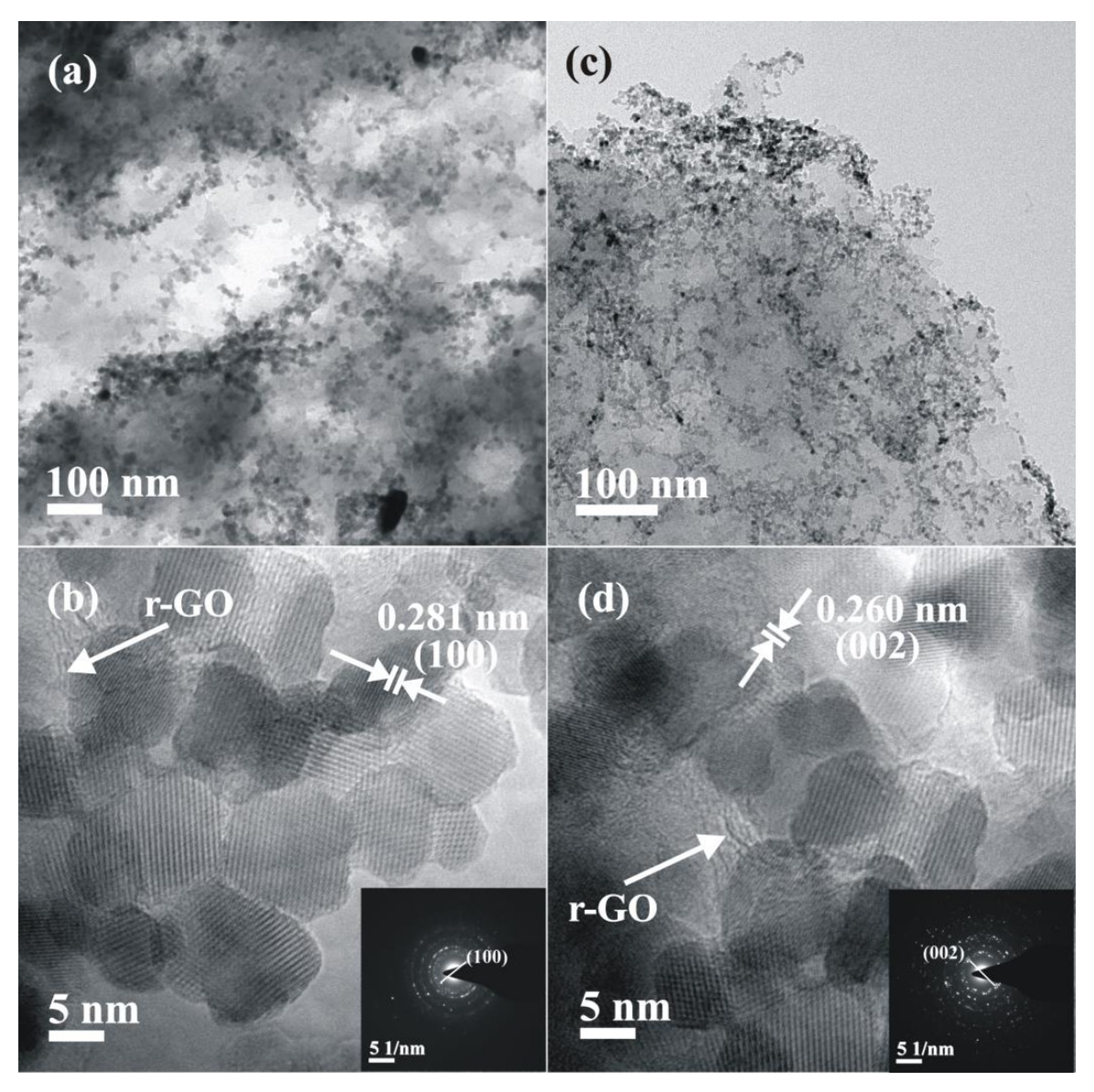


Figure 4.16. Secondary electron micrograph of ZnO-0.1G composite.



**Figure 4.17**. Secondary electron micrographs of (a) ZnO nanoparticles (b) low and (c) high magnification images of ZnO-0.2G composite.

TEM micrographs of ZnO-0.2G and ZnO-0.3G composites are shown in **Fig. 4.18(a)** and **(c)**, respectively. The micrographs clearly show uniform decoration of ZnO nanoparticles on both sides of r-GO sheets. High resolution TEM images (**Fig. 4.18(b)** and (**d**)) give a much clear picture on the sizes of ZnO nanoparticles decorated on the r-GO sheets. ZnO nanoparticles are observed to have sizes in the 10-20 nm with a narrow size distribution. (100) and (002) crystal faces with lattice spacing of 0.281 nm and 0.26 nm, respectively are marked on the micrographs. The corresponding electron diffraction patterns shown in the insets of **Fig. 4.18(b)** and (**d**) indicate the polycrystalline nature of ZnO nanoparticles.



**Figure 4.18.** (a) Low, (b) high resolution TEM image and its diffraction pattern (inset) of ZnO-0.2G, respectively whilst (c) low, (d) high resolution TEM image and its diffraction pattern (inset) of ZnO-0.3G, respectively.

Raman spectra of ZnO and ZnO-r-GO composites are shown in **Fig. 4.19**. All typical bands pertaining to ZnO could be identified in the case of all samples [34-38]. Raman band at 436 cm<sup>-1</sup> corresponds to non-polar optical phonon  $E_2$  (high) and the band at 582 cm<sup>-1</sup> is a typical band positioned between  $A_1$  (LO) +  $E_1$  (LO) of ZnO. The bands at 328 cm<sup>-1</sup> and 662 cm<sup>-1</sup> are owing to the surface phonon scattering. The bands observed in the range 1050-1200 cm<sup>-1</sup> are the typical second order scattering modes in ZnO [38]. In the case of ZnO decorated r-GO nanocomposites, the typical Raman bands corresponding to the presence of r-GO (D band (1343 cm<sup>-1</sup>), G band (1570 cm<sup>-1</sup>) and 2D band (2679 cm<sup>-1</sup>)) are clearly identified [39]. It is observed that the intensity of D and G bands increased with increase in r-GO content (Raman experiments were done with the same integration time of 5 sec and same focal condition and fit with Lorentz-function). The intensities of G and D bands are 95.9 and 43.86 ( $I_D/I_G = 0.45$ ), 81.71 and 22.2 ( $I_D/I_G = 0.27$ ), and 46.14 and 10.68 ( $I_D/I_G = 0.23$ ), respectively for ZnO-0.3G, ZnO-0.2G, and ZnO-0.1G, respectively. These values indicate that defects' concentration increased with r-GO content.

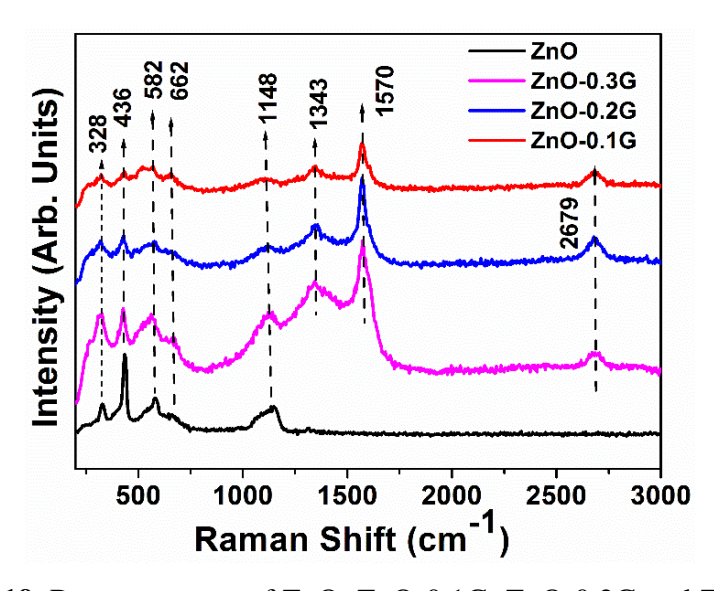


Figure 4.19. Raman spectra of ZnO, ZnO-0.1G, ZnO-0.2G and ZnO-0.3G.

All in all, the above presented results show that ZnO and r-GO containing nanocomposites have formed and that the ZnO nanoparticles are decorated on the surfaces and edges of r-GO.

#### 4.2.3 Dielectric behavior

**Fig. 4.20(a)** shows that the dielectric permittivity ( $\epsilon'$ ) decreased with an increase in frequency and that there is relaxation in all the samples (including ZnO). The behavior of dielectric permittivity in relation to the free dipoles (in the samples) oscillating in an alternating external electric field is classically described as follows: At very low frequencies  $\omega << 1/\tau$ ,

where  $\tau$  is the relaxation time, dipoles follow the field. As the frequency increases i.e., when  $\omega < 1/\tau$ , dipoles begin to lag behind the field and  $\epsilon'$  starts to slightly decrease. When the frequency reaches a characteristic frequency i.e., when  $\omega \sim 1/\tau$ , the dielectric constant drops (relaxation process). At very high frequencies, i.e., when  $\omega >> 1/\tau$ , dipoles can no longer follow the field and  $\epsilon' \approx \epsilon_{\infty}$ . Qualitatively it can be concluded from **Fig. 4.20(a)** that this behavior is observed in the samples considered in this work.  $\tau$  in the case of ZnO is  $\sim 8.8 \times 10^{-7}$  sec whilst it is one order high in the case of composites  $(1.62 \times 10^{-6}, 3.85 \times 10^{-6} \text{ and } 7.01 \times 10^{-6}$  sec in case of ZnO-0.1G, ZnO-0.2G and ZnO-0.3G, respectively). These values were calculated from  $\epsilon''$  versus  $\log(\omega \tau)$  and a single relaxation peak (as shown in **Fig. 4.21**) is observed in all the cases (including ZnO) which indicates Debye type of relaxation.

 $\varepsilon'$ ,  $\tan\delta$ , and  $\sigma$  values as a function of applied frequency for ZnO and ZnO decorated r-GO composites are shown in **Fig. 4.20**. At 1 kHz,  $\varepsilon'$  of ZnO is ~10 which is close to a previously reported value of ~9 measured in the case of similar ZnO nanoparticles [40].  $\varepsilon'$  values of ZnO decorated r-GO composites are significantly larger when compared to  $\varepsilon'$  of ZnO. Moreover, these values are observed to increase with increasing r-GO content. At 1 kHz,  $\varepsilon'$  values of ZnO-0.1G, ZnO-0.2G, and ZnO-0.3G are 11 ( $\varepsilon'$  = 114), 15 ( $\varepsilon'$  = 153) and 40 ( $\varepsilon'$  = 400) times greater that of ZnO ( $\varepsilon'$  = 10), respectively. It was also noticed that  $\varepsilon'$  values decreased as the frequency increased indicating that the polarization of constituents in all the samples is lagging behind the applied field. This is designated as Debye type of polarization. The increased  $\varepsilon'$  values in the case of composites are justified in the following paragraph.

r-GO contains polar functional groups like -OH, -CHO, -CO, -COOH etc., [41] which play a role in enhancing  $\epsilon'$  [42]. The availability of these functional groups is greater with increasing content of r-GO which ensures good bonding and appropriate local electrical contacts which may lead to a strong interfacial polarization (Maxwell-Wagner interfacial polarization) [32] in presence of an external electric field. This interfacial polarization becomes much stronger (hence  $\epsilon'$  enhancement) when a greater number of  $\pi$ -electrons are present, as in the present case owing to the presence of r-GO. Besides these, defects also play an important role. In the present case there are numerous lattice and/or topological defects [43] (as indicated by the identification of Raman D band in the case of composites) and interfaces which can bring changes in positive and negative space charge distributions creating a condition for the formation of numerous dipole moments which enhance  $\epsilon'$  [44].  $\tan\delta$  values for the composites are shown in **Fig. 4.20(b)**. It can be clearly observed that ZnO-0.1G ( $\tan\delta = 0.16$ )

and ZnO-0.2G ( $\tan\delta=0.42$ ) composites showed little loss in comparison to ZnO ( $\tan\delta=1.16$ ). In contrast, ZnO-0.3G sample showed high  $\tan\delta$  value of 2.31. This might be owing to inappropriate concentration of lattice defects in this sample as evidenced through Raman analysis. In the case of ZnO-0.3G, the defect related Raman band is the dominant feature ( $I_D/I_G$  was measured as 0.45). In the case of all the considered samples, it was also observed that  $\tan\delta$  values are lower at higher frequencies which is again a signature of Maxwell-Wagner relaxation. The lower loss in the case of ZnO-0.1G and ZnO-0.2G composites is attributed to strong interfacial polarization.

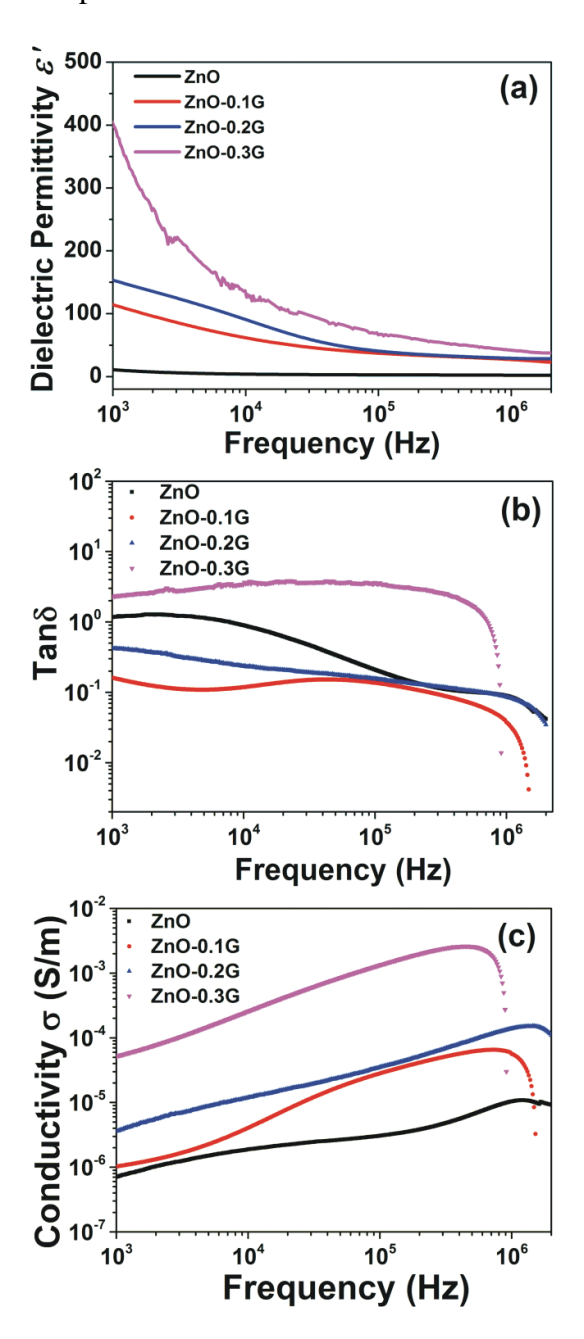


**Figure 4.20.** (a)  $\epsilon'$ , (b)  $\tan\delta$  and (c)  $\sigma$  vs. frequency plots of ZnO-0.1G, ZnO-0.2G and ZnO-0.3G composites in comparison to ZnO.

**Fig. 4.20(c)** shows an enhanced conductivity of the composites in comparison to ZnO. At 1 k Hz, σ values are 5.21×10<sup>-5</sup>, 3.62×10<sup>-6</sup>, 1.02×10<sup>-6</sup> and 7.08×10<sup>-7</sup> for ZnO-0.3G, ZnO-0.2G, ZnO-0.1G and ZnO, respectively. It was also observed that σ values increased with frequency. At a high frequency of 1 MHz, σ values are 2.56×10<sup>-3</sup>, 1.51×10<sup>-4</sup>, 6.11×10<sup>-5</sup> and 1.08×10<sup>-5</sup> for ZnO-0.3G, ZnO-0.2G, ZnO-0.1G and ZnO, respectively. The enhanced conductivity of the composites is due to hopping of charge carries [45] between the interfaces of ZnO nanoparticles and r-GO through cross-linked connections (possible for charge transfer channels) as seen in the case of CuO decked FLG (section 4.1.2). Above 1 MHz σ values decrease due to saturation of hopping carriers. In order to further understand the interfacial polarization, temperature dependence dielectric studies (relaxation) by varying the frequency in the range of 1-10 kHz were carried out on ZnO-0.2G, ZnO-0.1G and ZnO samples.

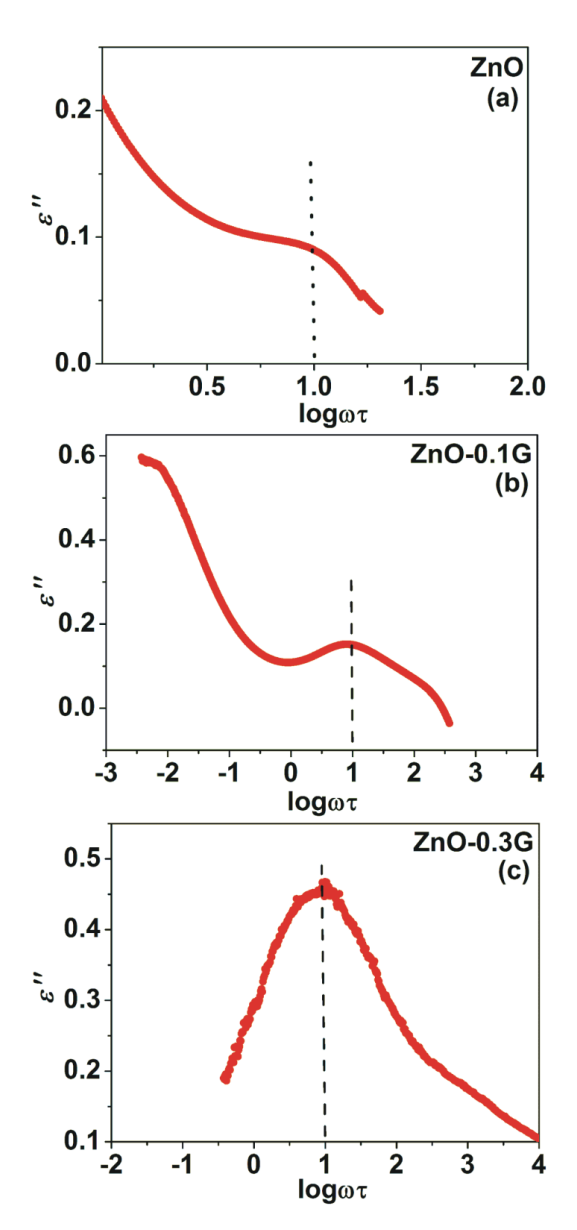


**Figure 4.21.**  $\varepsilon''$  Vs log( $\omega \tau$ ) plots of (a) ZnO, (b) ZnO-0.1G, and ZnO-0.3G samples.

**Fig. 4.22** shows  $\varepsilon'$  versus temperature at fixed frequencies (1, 2, 3, 4, 5 and 10 kHz) for ZnO-0.2G and ZnO-0.3G samples. It can be clearly observed that  $\varepsilon'$  values are small at around 50 °C. As the temperature is increased,  $\varepsilon'$  sharply increased in low frequency region (1 kHz) and slowly increased in high frequency region (10 kHz). As the temperature increased, the dipoles obtained sufficient thermal excitation energy and responded/followed in-phase with the applied field. As the temperature further increased (260 °C and 225 °C in case of ZnO-0.2G and ZnO-0.3G, respectively) the charges no longer followed the applied field and are observed to be relaxed. The similar phenomenon (not shown here) was also observed in the case of ZnO-0.1G and ZnO.

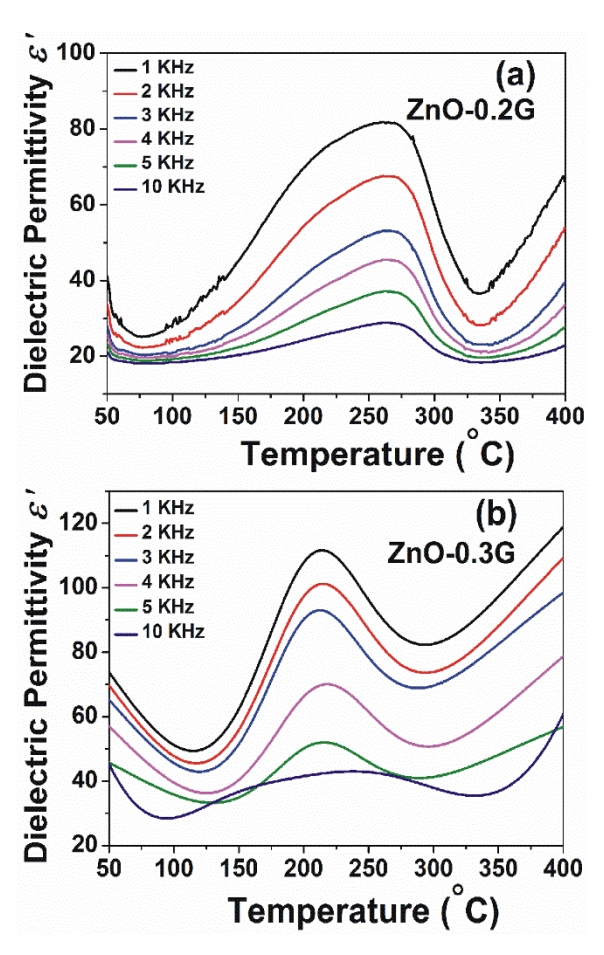


**Figure 4.22**. Dielectric permittivity as a function temperature of (a) ZnO-0.2G and (b) ZnO-0.3G sample.

The increment in the dielectric permittivity with decrease in frequency in the case of ZnO decorated r-GO composites (both in frequency (**Fig. 4.20(a**)) and temperature dependence (**Fig. 4.22**) plots) in comparison to ZnO reveals that the samples are exhibiting strong interfacial polarization at low frequencies. In order to obtain more information regarding the interfacial polarization in these composites, electric modulus formalism was examined and

debated. The advantage of using electric modulus formalism is to understand the dielectric response that it is independent of the nature of electrode and contact, space-charge injection and impurity conduction. These factors usually obscure dielectric relaxation [46,47]. M" (loss component) values pertaining to ZnO and ZnO decorated r-GO composites (ZnO-0.1G and ZnO-0.2G samples) are shown in **Fig. 4.23**. **Fig. 4.23(a)** corresponds to ZnO in which the first relaxation peaks (P1) which appeared at low temperatures i.e., around 50 °C (at constant frequencies 1-10 kHz) are due to interfacial polarization between ZnO nanoparticles. M" was in the order of 10<sup>-3</sup> which is an indication of losses in ZnO sample. Relaxation peaks (P2) which appeared at high temperatures i.e., around 255 °C are related to the hopping of ions (conductivity) due to presence of oxygen vacancies in ZnO [48]. It is also observed that as frequency increased from 1 kHz to 10 kHz there is a shift in both P1 (from 35 to 50 °C) and P2 (from 250 to 255 °C) peaks towards higher temperatures indicating the relaxation phenomenon [49,50]. The composite samples showed lower M" values (in the order of 10<sup>-4</sup>) in comparison to ZnO. This clearly indicates low losses and the existence of Maxwell-Wagner interfacial polarization in ZnO composites.

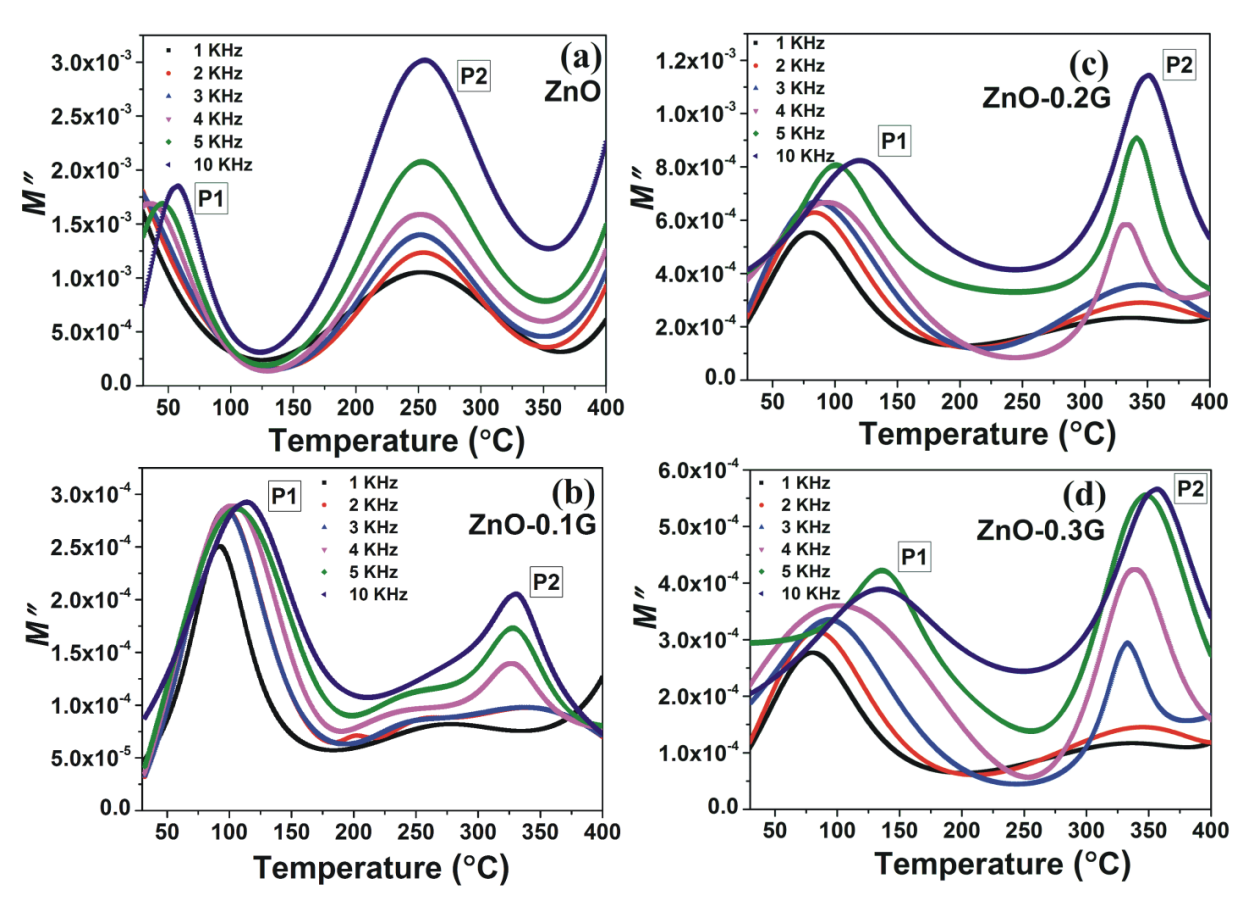


**Figure 4.23**. Electric modulus (*M*") as function of temperature at different frequencies 1, 2, 3, 4, 5, and 10 kHz of (a) ZnO (b) ZnO-0.1G (c) ZnO-0.2G and (d) ZnO-0.3G samples.

In the case of composites, the peaks P1 are shifted towards high temperatures. They are around 92-112 °C in the case of ZnO-0.1G while they are around 95-120 °C, 80-135 °C in case of ZnO-0.2G, ZnO-0.3G (frequency increase was from 1 kHz to 10 kHz) which further supports a strong interfacial polarization in composites owing to suitable defects [44]. It was observed that defects have increased with r-GO content and in this situation as the temperature increased there could be a blocking of charge carries' flow at different interfaces in the composites. In order to overcome this blockage, the carries appear to have obtained energy (from the increase in temperature) while the frequency of localized carriers was approximately equal to that of the applied AC field. Hence P2 peaks shifted towards much higher temperatures in the range 300-330, 330-355 and 330-358 °C in the cases of ZnO-0.1G, ZnO-0.2G and ZnO-0.3G composites, respectively, as frequency increased from 1 kHz to 10 kHz in comparison to ZnO (250-255 °C). Beyond these temperatures, the conductivity increased, which means that the system is under relaxation mode.

### 4.2.4 Unique polarization and ionic conductivity

In the previous section it was shown that ZnO decorated r-GO nanocomposites showed an excellent dielectric behavior. In the pursuit of further tuning the polarization behavior of ZnO decorated r-GO composites, minuscule variations in synthesis conditions were introduced and a new set of ZnO decorated r-GO nanocomposites were synthesized. PFG in r-GO could also help in controlling the morphology and crystal structure of ZnO, which is a poor polarizable material. In this work, it will be shown that the presence of an appropriate number of polar functional groups (PFG) along with defects and a slightly distorted ZnO lattice (owing to minuscule changes in synthesis conditions) help in tuning the polarization behavior of ZnO decorated r-GO composites.

The new set of ZnO decorated r-GO nanocomposites were synthesized in the following manner: In the 1<sup>st</sup> step, 0.1 g of r-GO powder was dispersed in 250 ml ethanol by sonication for 30 min to obtain a stable suspension. In the 2nd step, 0.9 g of zinc acetate dehydrate (Zn(CH<sub>3</sub>COO)<sub>2</sub>·2H<sub>2</sub>O) was added to the r-GO suspension and then sonicated for 3 h instead of 2 h as in the case of nanocomposites presented in section 4.2.3. In the 3<sup>rd</sup> step, the resultant solution was heated at 100 °C in air. In the final step which involves the calcination process, the product was heated at 400 °C (instead of 500 °C as in the case of nanocomposites presented in section 4.2.3) for 8 h in ambient atmosphere to obtain ZnO decorated r-GO named as ZnO- 0.1G. Two other composites named as ZnO-0.2G and ZnO-0.3G are also

synthesized using 0.2 g of r-GO and 0.8 g of Zn(CH<sub>3</sub>COO)<sub>2</sub>·2H<sub>2</sub>O and 0.3 g of r-GO and 0.7 g Zn(CH<sub>3</sub>COO)<sub>2</sub>·2H<sub>2</sub>O, respectively. For comparison purposes, ZnO similar to that in the composites was also synthesized. The ZnO nanoparticles were prepared using Zn(CH<sub>3</sub>COO)<sub>2</sub>·2H<sub>2</sub>O, the same precursor used to obtain ZnO in the case of composites. ZnO nanoparticles were synthesized by using a simple sono-chemical method in which 0.1 M sodium hydroxide (NaOH) was drop-wise added to 0.1 M Zn(CH<sub>3</sub>COO)<sub>2</sub>·2H<sub>2</sub>O solution (ethanol as the solvent) under vigorous stirring. The resultant solution was subsequently sonicated for 2 h to obtain a gel which was dried at 80 °C by keep it overnight on magnetic stirrer. The obtained powder was heated at 400 °C for 5 h to finally obtain nanocrystalline ZnO particles similar to those decorated on r-GO in the composites.

In the synthesis method mentioned above, an increase in the time of sonication and the 2<sup>nd</sup> step were aimed to enhance the dispersion of Zn ions among the suspended r-GO sheets in ethanol and to promote the effective reaction between Zn ions and functional groups on r-GO sheets. The enchantment is mainly attributed to the improved thermolysis of the solute and the formation of highly reactive radicals such as hydroxyl radicals, which create extreme reaction conditions in media such as ethanol. Also, the growth of the nucleated solid in the solution is inhibited, thereby increasing the total solid surface in contact with the solvent. It can also be observed that the increase in time of sonication in the 2<sup>nd</sup> step helped in decreasing the calcination temperature. Similar to the studies carried out on the nanocomposites whose results were presented in the previous section, studies were also carried out on the new set of nanocomposites.

XRD profiles (observed as well as calculated) of different samples are shown in **Fig. 4.24**. Except for (002) reflection at 26.4°, which corresponds to r-GO in composites (except in ZnO-0.1G, which plausibly did not have enough r-GO content that could diffract), all other diffraction peaks are indexed to hexagonal ZnO crystal structure. The calculated lattice parameters (**Table 4.2**) are a = 3.2523 Å, c = 5.2022 Å, and therefore c/a = 1.5995 in the case of ZnO-0.2G whilst a = 3.2514 Å, c= 5.2010 Å, and therefore c/a = 1.5996 in case of ZnO-0.3G (1.6008 in case of ZnO-0.1G). This confirms that ZnO lattice in composites is 'squeezed' along c-axis in comparison to ZnO nanoparticles (c/a ratio is ~1.602) [51]. **Fig. 4.25** shows the composites' Raman spectra, the features in which are similar to those presented in the section 4.2.2. The features indicate the presence of partially reduced GO and ZnO in the composites. For convenience, Raman and FTIR spectra of r-GO are shown in **Fig. 4.26** and **Fig. 4.27**, respectively.

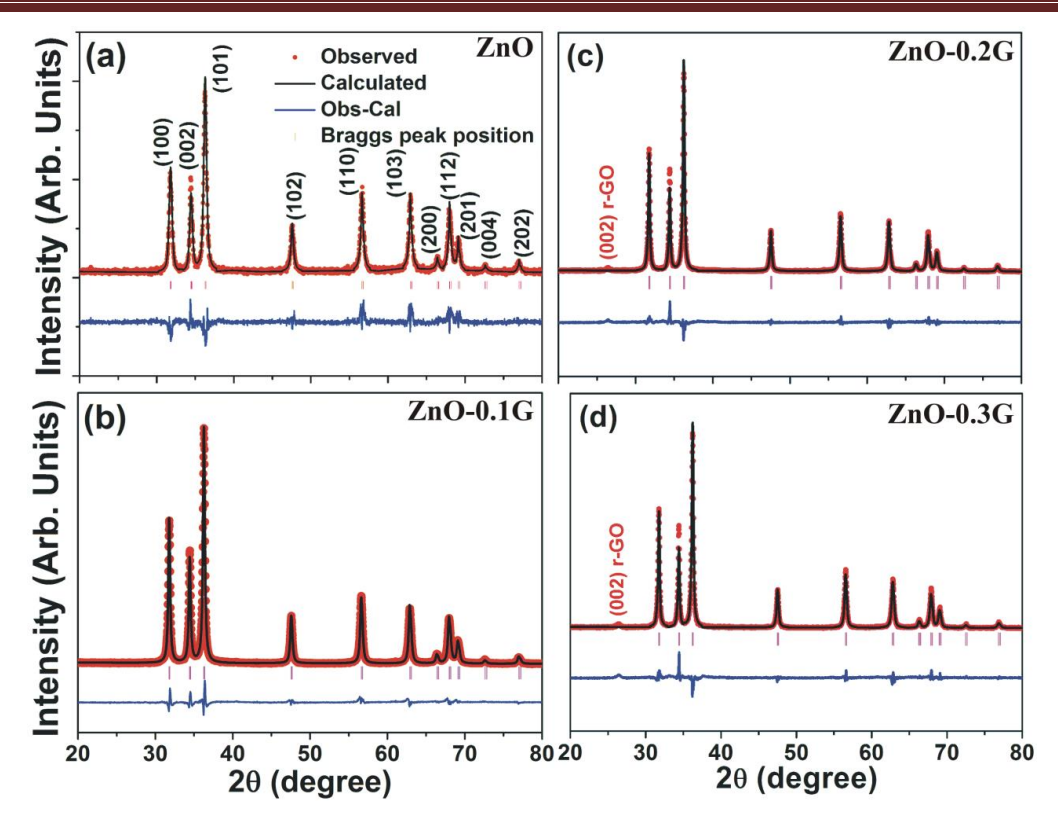


**Figure 4.24.** XRD profiles of (a) ZnO, (b) ZnO-0.1G (c) ZnO-0.2G and (b) ZnO-0.3G samples and the corresponding Rietveld refined profiles.

**Table 4.2.** Summary of lattice parameters values of ZnO and ZnO/r-GO composites from Rietveld analysis.

Sample	Lattice parameters		c/a	error
	a and c			
ZnO	3.2492	5.2054	1.6020	$\pm$ 0.00020; a axis
ZnO-0.1G	3.2511	5.2045	1.6008	
ZnO-0.2G	3.2523	5.2022	1.5995	$\pm 0.00015$ ; c axis
ZnO-0.3G	3.2514	5.2010	1.5996	

Raman band at 432 cm<sup>-1</sup> (**Fig. 4.25**) corresponds to non-polar optical phonon E<sub>2</sub> (high) while the band at 573 cm<sup>-1</sup> is a typical band positioned between A<sub>1</sub> (LO) + E<sub>1</sub> (LO) of ZnO. The bands at 324 and 657 cm<sup>-1</sup> are due to surface phonon scattering by ZnO. The band at 1125 cm<sup>-1</sup> is a typical second order scattering mode of ZnO. The typical D (1341 cm<sup>-1</sup>), G (1565 cm<sup>-1</sup>) and 2D (2673 cm<sup>-1</sup>) bands corresponds to the presence of partially reduced GO in the composites are also observed. Raman spectrum of r-GO (**Fig. 4.26**) shows the typical G band at ~1574 cm<sup>-1</sup>, D band at ~1345 cm<sup>-1</sup> and 2D band at ~2678 cm<sup>-1</sup>. FTIR spectrum of r-GO (**Fig. 4.27**) shows the presence of different type of oxygen functional groups (the bands at 3402, 1720, 1228 and 1058 cm<sup>-1</sup> correspond to O-H stretching, C=O, C-OH, and C-O stretching modes, respectively [52,53].

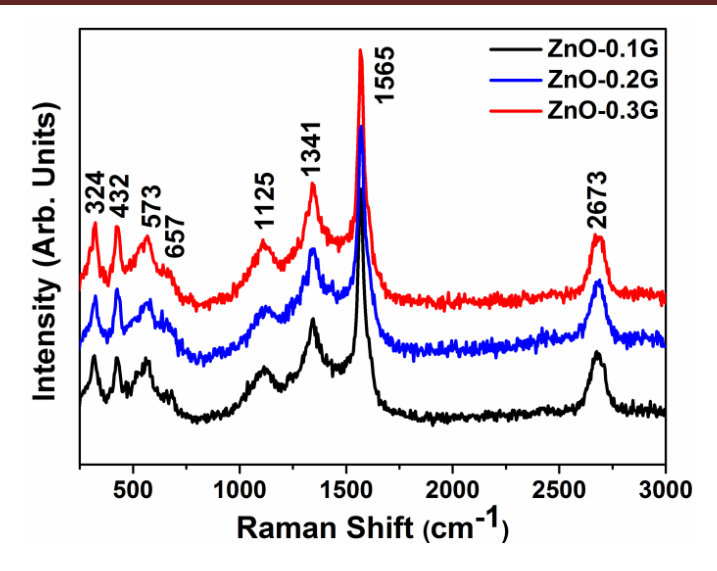


Figure 4.25. Raman spectra of ZnO-0.1G, ZnO-0.2G and ZnO-0.3G samples.

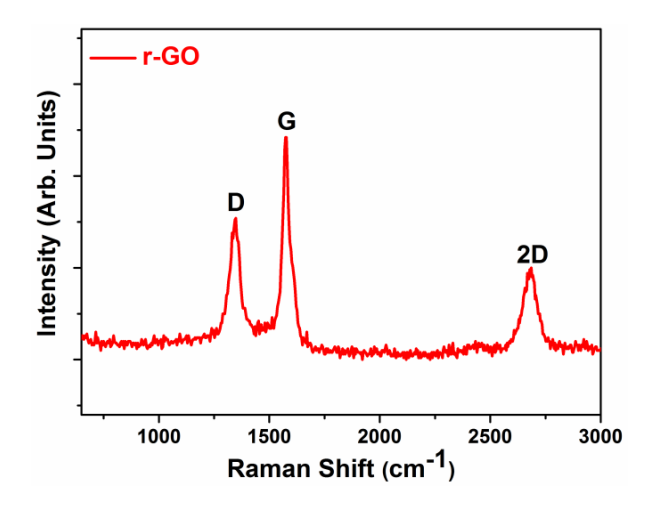


Figure 4.26. Raman spectrum of r-GO.

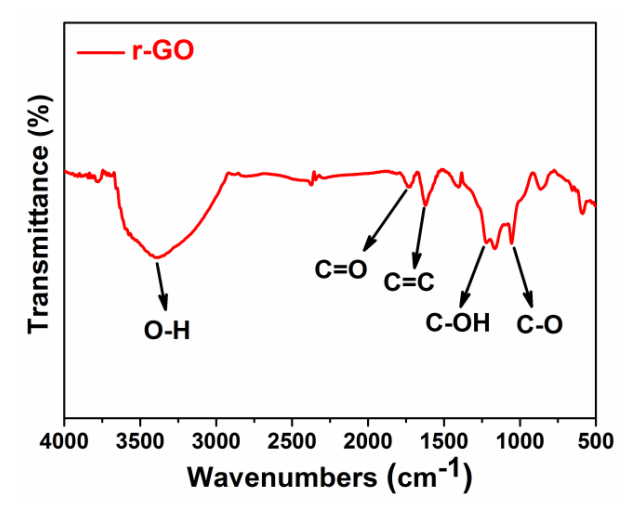
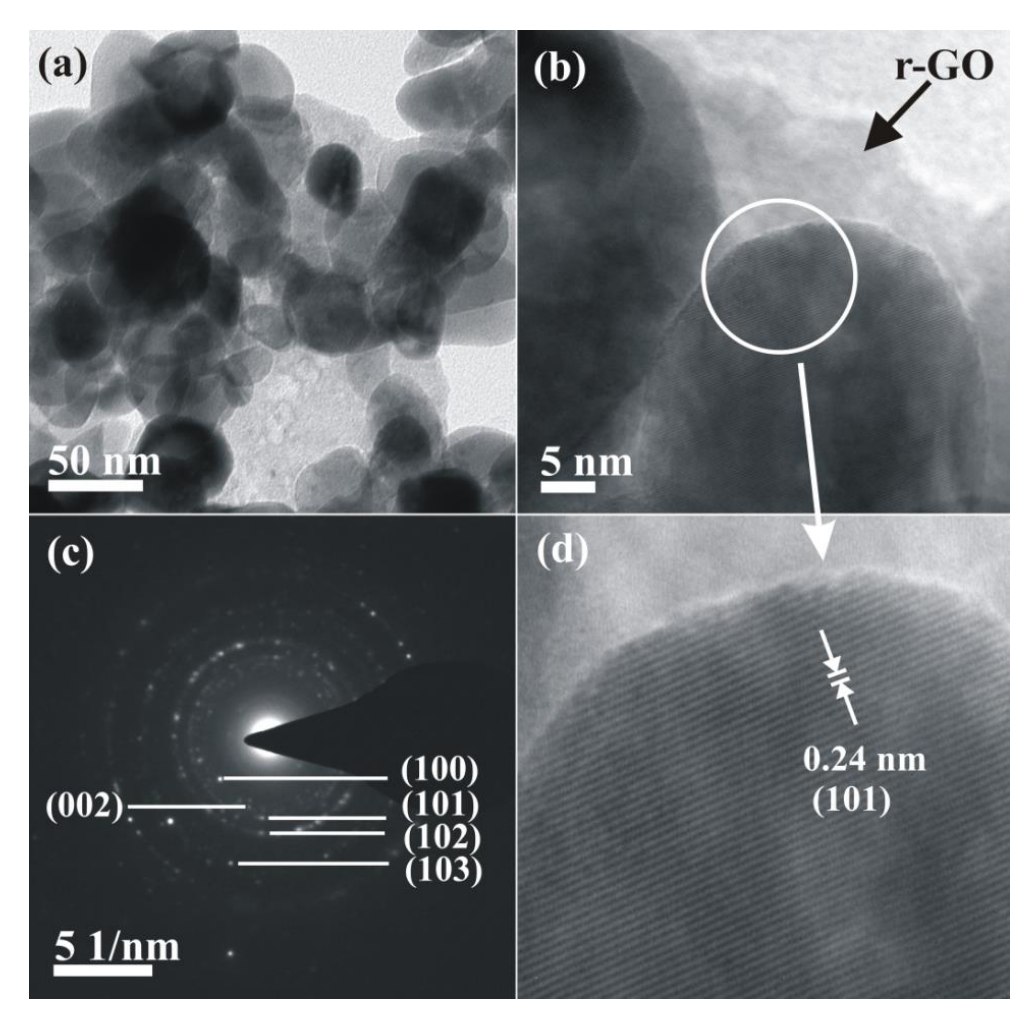


Figure 4.27. FTIR spectrum of r-GO.

Further, electron microscope images (Figs. 4.28 and 4.29) shows clearly the excellent decoration of ZnO nanoparticles on r-GO sheets. TEM micrographs (including the high-resolution micrograph) and a representative electron diffraction pattern of ZnO-0.3G sample are shown in Fig. 4.28. From Figs. 4.28(a) and 4.28(b) the decoration of ZnO particles on r-GO can be clearly observed. It is also clear from these images that the sizes of ZnO nanoparticles decorating r-GO sheets are in the range of 10–20 nm with a narrow size distribution. In Fig. 4.28(d), the lattice spacing of 0.24 nm that corresponds to (101) ZnO in ZnO-0.3G sample is marked. In Fig. 4.28(c), the diffraction spots corresponding to the presence of r-GO in the composite are faintly visible and hence are not indexed. Good homogeneity of the ZnO nanoparticles' decoration is clearly observed from low magnification electron micrographs as shown in Fig. 4.29. Similar observations have also been made in section 4.2.2.



**Figure 4.28.** TEM data of ZnO-0.3G. (a) Low, (b) high resolution image and its (c) diffraction pattern respectively; (d) high resolution image (corresponding the encircled area in (b)) showing the lattice fringes of (101) ZnO.

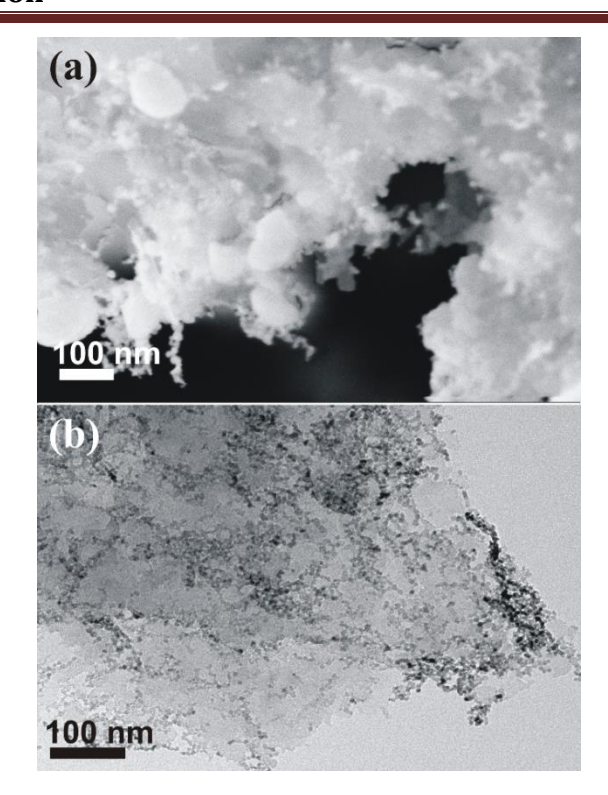


Figure 4.29. Low magnification (a) FESEM and (b) TEM images of ZnO-0.3G.

It is now known that r-GO can be decorated with several PFG such as -OH, -CHO, - CO, -COOH, etc., and that C in r-GO will be in different oxidation state depending on the bond it makes (with H or O) [54]. Basically these are polar bonds (uneven sharing of electrons; which creates a partial positive and negative sign on atoms/ions in bond formation). On other hand pure ZnO (without defects) is an insulator, but due to presence of defects it acts as a semiconductor. Oxygen vacancies and zinc interstitials have often been invoked as sources of electric sign in ZnO. The excess of Zn<sup>+2</sup> ions (oxygen vacancies lead to non-stoichiometric) were create a partial positive sign on ZnO which can make bond with negative sign of oxygenated polar functional groups. In this condition, the ZnO nanoparticles decorating the r-GO sheets (as shown in electron micrographs) make contacts with different functional groups typically in the form of ZnO/PFG/GO which gives an opportunity for any free charge carriers from r-GO side to tunnel into ZnO lattice during the formation of the composite and push the ZnO lattice into a distorted condition, thereby the changes in c/a ratios of ZnO lattice in the case of composites as revealed by XRD analysis (Figure 4.24 and Table 4.2). In general, the lattice parameters were mainly influenced by Coulomb interactions between atoms or ionic species, oxidation states, presence of foreign atoms/ions or charge carriers, and ionic radius [55,56]. In the present study, since ZnO nanoparticles are decorated on functionalized r-GO sheets, a charge transfer might have occurred between ZnO and r-GO and thereby a distorted

ZnO lattice was observed (as confirmed by XRD analysis). A similar observation was previously made in the case of doped ZnO [57-59]. It has been observed that, when the ionic radius of the dopant (for example, 0.60 A for Li<sup>+1</sup>) is smaller than the host (0.74 A for Zn<sup>+2</sup>), the substituents occupy off-centered positions causing distortion in the lattice and locally induce electric dipoles which eventually influence the polarization behavior. By this, in the present case, one can anticipate that ZnO/PFG/GO arrangement may exhibit unique polarization behavior in the presence of an electric field. To understand this, polarization (P) versus (Vs) electric field (E) measurements were carried out and the discussion is presented in the following paragraphs.

P Vs E of different samples is shown in **Fig. 4.30** which clearly shows that ZnO exhibits poor polarization. P Vs E curve of ZnO indicates that the current and voltage are in-phase and therefore no charge storage capability. On the contrary, the composites clearly exhibited P-E hysteresis revealing their charge storage capability. It is observed that the area of the hysteresis loop is significantly enhanced with increasing r-GO content in the composites. However, the slight elliptical shape of the loops indicates that the resistive component in the nanocomposite is greater than the capacitive component.

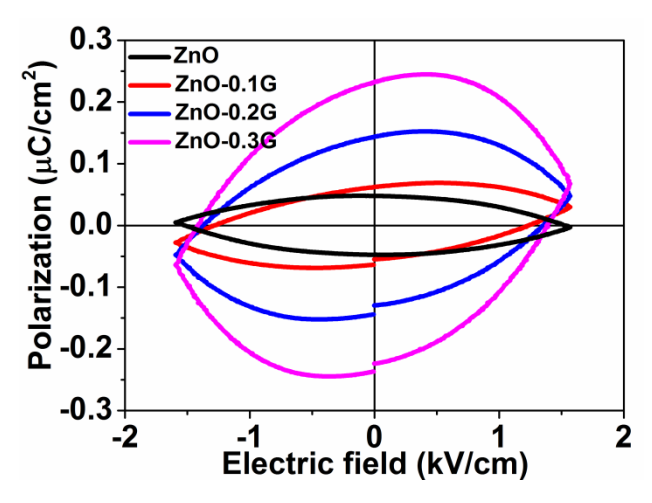
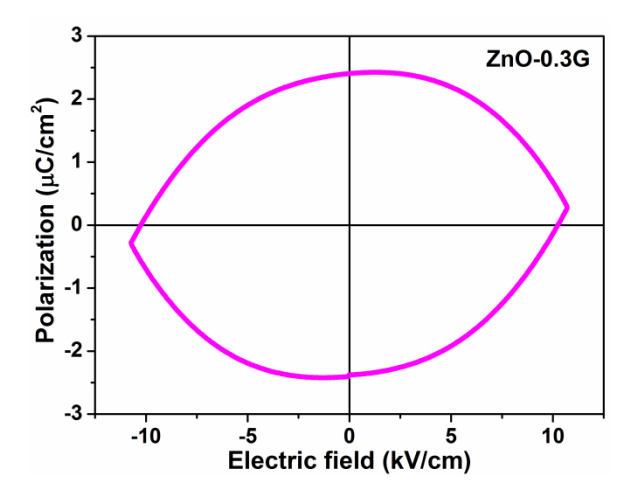


Figure 4.30. P-E hysteresis curves of ZnO and ZnO decorated r-GO composites.

**Table 4.3.** Remnant polarization (P<sub>r</sub>), maximum polarization (P<sub>max</sub>) and coercive field values obtained from P-E measurements on different ZnO/r-GO composites.

Sample	Electric field (kV/cm)	Coercive field (kV/cm)	Remnant polarization (P <sub>r</sub> ) ( $\mu$ C/cm <sup>2</sup> )	$P_{max}$ ( $\mu$ C/cm <sup>2</sup> )
ZnO-0.1G	-1.6 to 1.6	1.24	0.062	0.069
ZnO-0.2G		1.35	0.143	0.152
ZnO-0.3G		1.37	0.232	0.245

Careful observation of the P-E hysteresis loops of the composites at same field strength (~1.6 kV/cm) clearly showed that an increase in r-GO content in the composites resulted in the increase of remnant polarization ( $P_r$ ) and maximum polarization ( $P_{max}$ ) by at least one order. These values are tabulated in **Table 4.3** (previous page). In the case of ZnO-0.3G,  $P_r$  value increased to 2.402  $\mu$ C/cm<sup>2</sup> (**Fig. 4.31**) at 11 kV/cm. These results are consistent with a previous work [60] where-in, the material showed high dielectric permittivity due to enhancement in polarization with increasing r-GO content. However, here the composites did not exhibit any discernible saturation polarization (i.e., absence of ferroelectric behavior) [61] most plausibly owing to heat or leakage current losses.



**Figure 4.31.** P-E loop of ZnO-0.3G composite sample recorded at 11 kV/cm.

The above presented observations strongly indicate that the presence of r-GO (and through which the presence of PFG) plays an important role in pushing the system into an easy polarization direction. Here it should be noted that the PFG [59,62] at appropriate positions on r-GO are also in contact with ZnO nanoparticles (i.e., ZnO/PFG/GO) and as r-GO content increases in the composites, the number of availability functional groups will also increase. In the composite, owing to ZnO/PFG/GO arrangement at numerous locations, the electrical contacts between ZnO and r-GO are expected to be robust in nature ensuring a significant increase in the relative concentration of the dipole moments which in turn lead to easy dipolar alignment and reorientation [41] and thereby ultimately increasing the number of stable polarization states with respect to the applied field direction as observed in Fig. 4.30. This can be understood on the basis of Valence Shell Electron-Pair Repulsion (VSEPR) theory [63] which, when applied to the present situation indicates that there can be different types of local bonding configurations that can induce dipole moments. The polarization behavior of ZnO decorated r-GO composites is similar to that of graphene based hetero-structured tunnel

junction [63]. Hence, the enhanced polarization in ZnO/r-GO composites is due to both distorted ZnO lattice and the orientation of PFG.

In a previous report it was shown that the conductivity (product of mobility and charge carrier density) of the composites can be enhanced by polarization [64]. In another report it was shown that the proton conductivity in GO along its surface is very high due to the presence of -OH, -COOH, and -CO functional groups [41]. These reports [64,41] indicate that there is a relation between conductivity and PFG. In view of this, it is quite interesting to observe the ionic conductivity (Fig. 4.32; please read Fig. 4.32 with Figs. 4.33 and 4.34) in ZnO decorated r-GO composites in the temperature range 398-523 K. In general, the total conductivity ( $\sigma(\omega)$ ) is the sum of dc and ac conductivities [65] i.e.,  $\sigma(\omega) = \sigma_{dc} + A\omega^{s}$ , where A is the pre-exponential factor which depends on temperature, ω is the frequency and s is a dimensionless exponent. The thermally activated hopping ions aid in dc conduction which is frequency independent and has long range order. Here, all the samples exhibited high frequency dispersion with an essential part of frequency independent conductivity at low frequencies. The samples are found to switch over from frequency independent region to frequency dependent region showing an onset of conductivity relaxation. The temperature dependent conductivity followed the Arrhenius law [66] given by:  $\sigma_{dc} \alpha T^{-1} \exp(\frac{-E_a}{k.T})$ where T is temperature in Kelvin,  $k_{B}$  is Boltzmann constant and Ea activation energy for dc conduction. The conductivity ( $\sigma_{dc}$ ) plots (**Fig. 4.35**) i.e.,  $\ln(\sigma_{dc}T)$  Vs 1000/T plots are fitted with linear function.  $\sigma_{dc}$  values were found to increase with temperature, and the linear fits of the plots of  $ln(\sigma T)$  Vs 1000/T (shown in **Fig. 4.35**) revealed dc activation energies (E<sub>a</sub>) of 0.581, 0.560 and 0.538 eV in the case of ZnO-0.3G, ZnO-0.2G and ZnO-0.1G composites, respectively. It is well-known that reduction of functional groups increases the fraction of sp<sup>2</sup> carbon atoms [67] and as a result conductivity increased in all composites in comparison with ZnO. Also, here the conductivity depends on the temperature and values are increased from ~ $10^{-3} \Omega^{-1} \text{ cm}^{-1}$  to  $10^{-2} \Omega^{-1} \text{cm}^{-1}$  (**Table 4.4**) with increasing temperature. These observations were consistent with previous reports on the conductivity studies of r-GO [65,68-70]. From Fig. 4.32 it can be clearly observed that in the frequency region 10<sup>3</sup>-10<sup>6</sup> Hz, the conductivity values have uniformly increased with the temperature indicating that the conductivity is thermally activated.

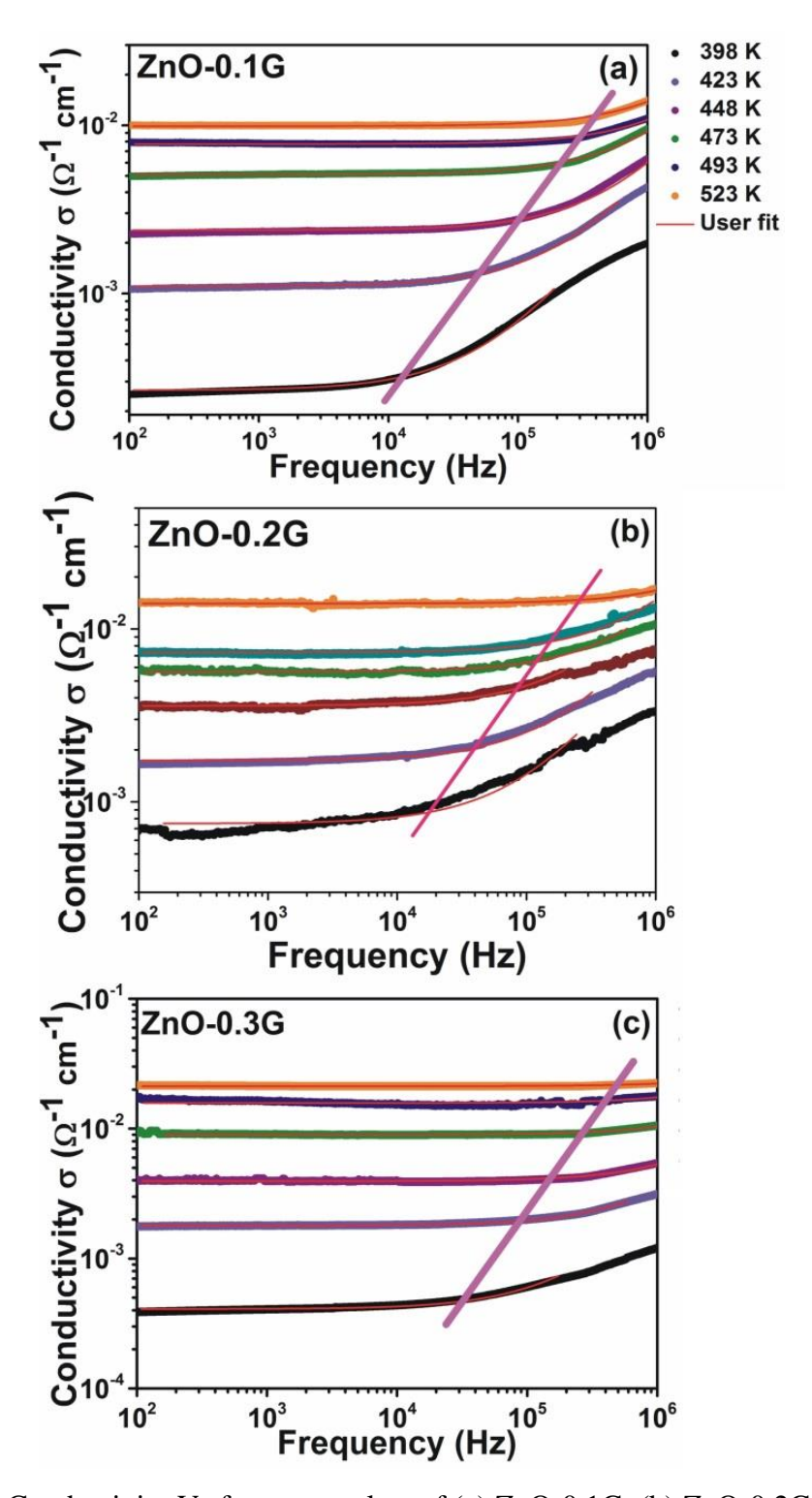


**Figure 4.32.** Conductivity Vs frequency plots of (a) ZnO-0.1G, (b) ZnO-0.2G and (c) ZnO-0.3G samples fitted with an appropriate power law (**Figs. 4.33** and **4.34**). The straight line in the figures indicates that the conductivity is thermally activated.

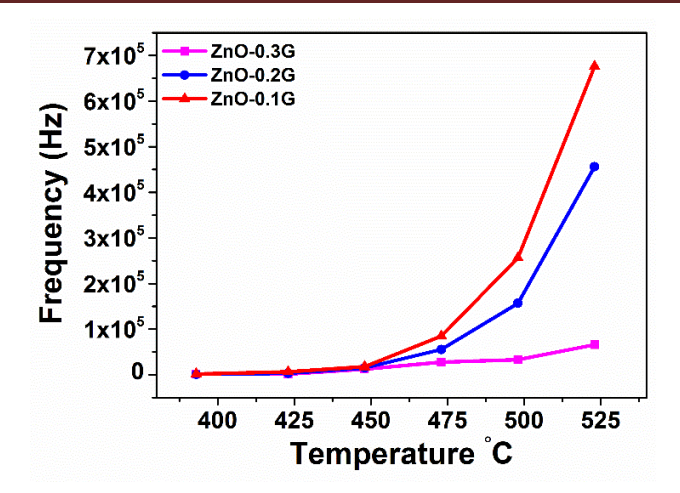


**Figure 4.33.** Frequency Vs temperature for different ZnO/r-GO composites which switch from frequency independent region to frequency dependent region showing an onset of conductivity relaxation, which shifted towards higher frequencies as temperature increased.

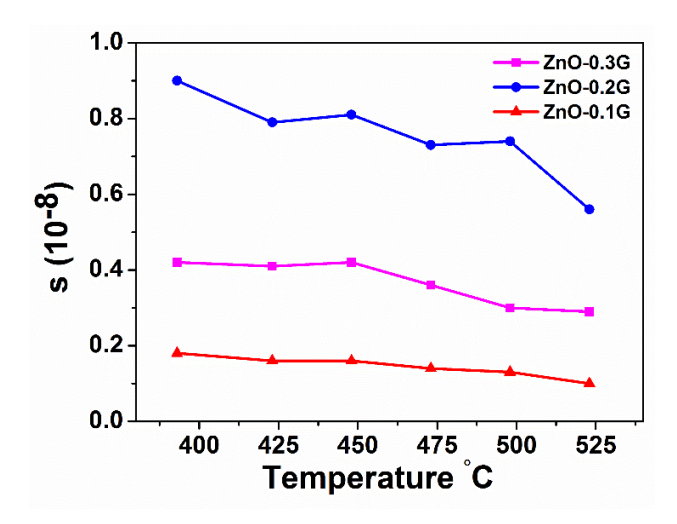


**Figure 4.34.** Variation of the fitting exponent 's' with temperature. The range of fitting was  $10^3$ - $10^6$  Hz. The s value varied (order of  $10^{-8}$ ) form 0.18 to 0.1 in the case of ZnO-0.1G, form 0.9 to 0.56 in the case of ZnO-0.2G and from 0.42 to 0.29 in the case of ZnO-0.3G. The range of fitting increased with temperature.

From **Table 4.4** it can be easily noticed that the conductivity slightly decreased with increasing r-GO concentration as a consequence of varied dc activation energy values. Here it should be noted that low activation energy leads to high  $\sigma_{dc}$  and vice versa. This implies that r-GO in the composite is only partially reduced as indicated by Raman scattering results If it is completely reduced, higher content of r-GO should result in higher  $\sigma_{dc}$  of the composite because  $\sigma_{dc}$  of r-GO is much higher than that of ZnO. On the contrary to the composites, ZnO did not exhibit the Arrhenius behavior (as shown in **Fig. 4.36**) while the conductivity values are found to be consistent with those reported in the literature [71,72].

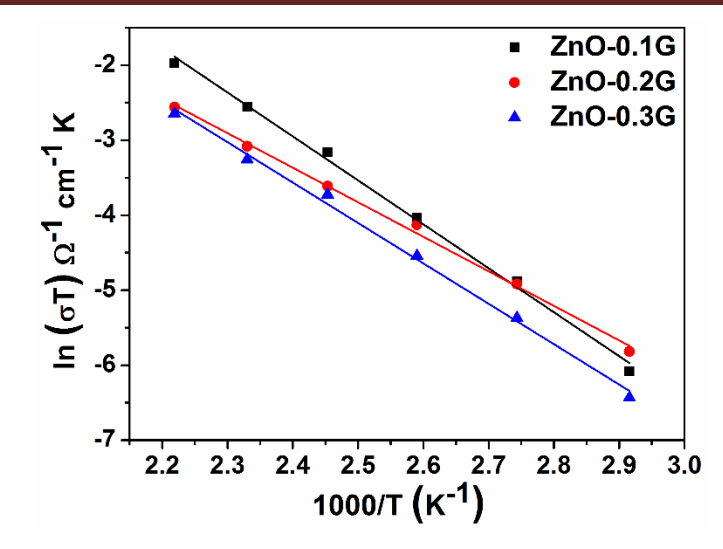


**Figure 4.35.**  $ln(\sigma T)$  Vs 1000/T for ZnO-0.1G, ZnO-2G and ZnO-0.3G samples.

<b>Table 4.4.</b> Conductivity	(odc	values of ZnO/r-GO com	apposites at different temperatures.
--------------------------------	------	------------------------	--------------------------------------

Temperature	Conductivity (Ω <sup>-1</sup> cm <sup>-1</sup> )				
(Kelvin)	ZnO-0.1G	ZnO-0.2G	ZnO-0.3G		
393	0.40 ×10 <sup>-3</sup>	0.37×10 <sup>-3</sup>	0.26 ×10 <sup>-3</sup>		
423	0.18×10 <sup>-2</sup>	0.17×10 <sup>-2</sup>	$0.11 \times 10^{-2}$		
448	0.39×10 <sup>-2</sup>	0.35×10 <sup>-2</sup>	0.23×10 <sup>-2</sup>		
473	$0.89 \times 10^{-2}$	0.56×10 <sup>-2</sup>	$0.50 \times 10^{-2}$		
498	1.57×10 <sup>-2</sup>	0.77×10 <sup>-2</sup>	$0.72 \times 10^{-2}$		
523	1.82×10 <sup>-2</sup>	1.47×10 <sup>-2</sup>	0.98×10 <sup>-2</sup>		

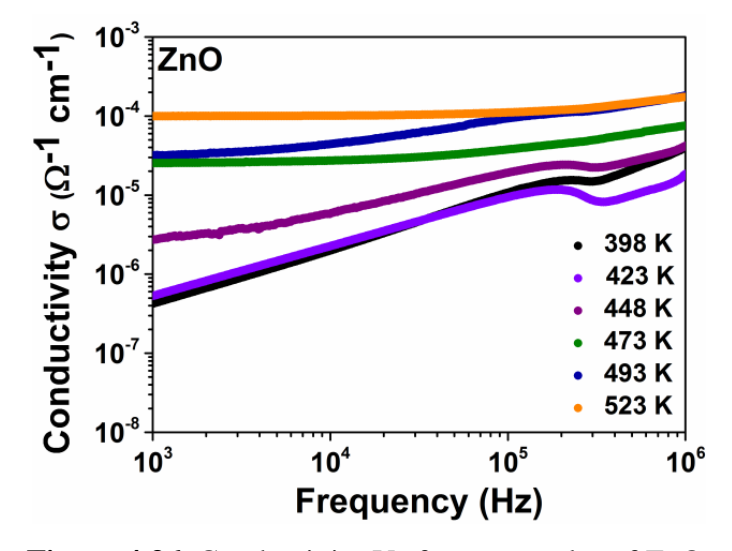


Figure 4.36. Conductivity Vs frequency plot of ZnO.

The conductivity of the samples can be understood on the basis of scattering mechanism as reported in the literature [73,74] according to which the conductivity is given by  $\sigma = ne\mu$  where  $\mu = \frac{e\tau}{m^*}$  is mobility, a function of effective mass  $(m^*)$  and relation time  $(\tau)$  of charge carriers.  $\tau$  is related to the scattering mechanism in materials. It is known that  $\tau$  is a function of vacancies and velocity  $(v) = \sqrt{\frac{3k_{\beta}T}{m^*}}$  of the charge carriers [73,75]. For normal semiconductors, the scattering possibility decreases with increasing temperature (directional mobility of charge carriers increases and thereby the conductivity increases). In polar semiconductors, the charge carriers might be scattered by long optical wave. Therefore, in polar semiconductors both intrinsic carrier concentration and mobility are responsible for conductivity, which increases with temperature as in the present case of the composites. With increasing r-GO the charge carrier concentration might be increased but the ions' mobility (which depends on  $\tau$ ) might be constrained on account of polarization.

Based on the above observations, the conductivity behavior of composites w.r.t increase in r-GO content in composites is justified in the following manner: Generally, conductivity ( $\sigma$ ) depends on both mobility ( $\mu$ ) and charge carrier (ions) density (n) as it is the product of  $\mu$  and n. In the case of the ZnO-0.1G sample, the conductivity is slightly high (low r-GO content) in comparison to other two samples. This implies that the mobility of ions is more elevated in the case of the ZnO-0.1G sample as reflected in the measured low activation energy (0.538 eV) in comparison to ZnO-0.2G (0.560 eV) and ZnO-0.3G (0.581 eV) samples which contain more functional groups (owing high r-GO content). This clearly indicates the ions or charge carriers in ZnO-0.3G and ZnO-0.2G samples are constrained and unable to wander throughout the material (reflecting the charge carriers' bound nature). This in turn has been reflected as high polarization (easy alignment and re-orientation) in these samples in comparison to ZnO-0.1G sample.

# 4.3 MgO decorated r-GO

#### 4.3.1 General comments

In the previous sections dielectric behavior of metal oxide decorated r-GO nanocomposites was attributed mainly to the functional groups and to the layered structure of r-GO sheets (in the composites) which naturally created numerous capacitors that led to charge accumulation based on Maxwell–Wagner polarization [32,76]. As mentioned previously, the dielectric behavior of the above mentioned nanocomposites is strongly dependent on the type of

underlying polarization mechanism. Till now it was elucidated that the dielectric behavior of graphene-based composites depends majorly on the polarization mechanisms namely i) electronic (10<sup>13</sup>-10<sup>16</sup> Hz) and ii) ionic polarizations (10<sup>9</sup>-10<sup>13</sup> Hz) due to the small displacement of electrons and ions, iii) dipolar polarization due to the orientation of molecular dipoles (below 10<sup>9</sup> Hz) and iv) Maxwell-Wagner or interface polarization (radio frequency region) due to the charges accumulated at the interfaces in the composites. In this context it was also very interesting to elucidate whether or not graphene-metal oxide composites exhibit Debye or non-Debye relaxation. While studying the general dielectric behavior of MgO decorated r-GO composites, a hint of non-Debye relaxation was observed. Hence, a thorough study was conducted and non-Debye relaxation in MgO decorated r-GO composites was confirmed and explained using Havriliak-Negami (HN) relaxation function. Strong interfacial polarization was also noticed in these composites.

### 4.3.2 Structural, morphological, and phase analysis

XRD patterns of MgO-0.05G and MgO-0.15G are shown in Fig. 4.37. The XRD patterns of all the composites are almost the same except for the observation of a very low intensity peak at  $2\theta = 26.4^{\circ}$  in the case of MgO-0.15G. This peak confirms the existence r-GO in the composite. The absence of this peak in the other cases is due to complete coating of MgO on r-GO sheets and due to low volume content of r-GO. The diffraction peaks at  $2\theta = at 36.8^{\circ}$ , 42.8°, 62.1°, 74.5° and 78.4° are indexed to (111), (200), (220), (331) and (222) lattice planes, respectively in cubic MgO. These diffraction peaks could also be well-matched with the peaks in the JCPDS data file No. 79-0612, which corresponds to cubic MgO. The secondary electron micrographs of MgO decorated r-GO composites are shown in Fig. 4.38. It can be observed from the micrographs that small particles are decorated on sheet-like features. The decoration is clearer in the high magnification images shown in Figs. 4.38(b), (d), and (f). Further clarity on the decoration of MgO on r-GO was obtained through TEM analysis. TEM images of MgO-0.15G composite are shown in Fig. 4.39 which clearly shows that the surface and cross-section of r-GO sheets are uniformly decorated by MgO particles whose crystallinity was confirmed by indexing of the corresponding electron diffraction pattern shown in Fig. 4.39(d). Raman spectra of MgO decorated rGO composites are shown in Fig. 4.40, in which the typical D, G and 2D bands are observed at ~1340, ~1570 and ~2680 cm<sup>-1</sup>, respectively, indicating the presence of r-GO in composites. All in all, through different characterization methods, it is confirmed that MgO nanoparticles are decorated on r-GO sheets. The probe ultrasonication assisted chemical method is an effective technique to

homogeneously disperse metal ions on r-GO. It is well known that residual oxygenated functional groups are attached to r-GO sheets. Amongst these functional groups, the carboxylic acid (-COOH) may interact with  $Mg^{+2}$  ions to form  $Mg(OH)_2$  on r-GO sheets. During calcination,  $Mg(OH)_2$  undergoes thermal oxidation and forms MgO on r-GO sheets.

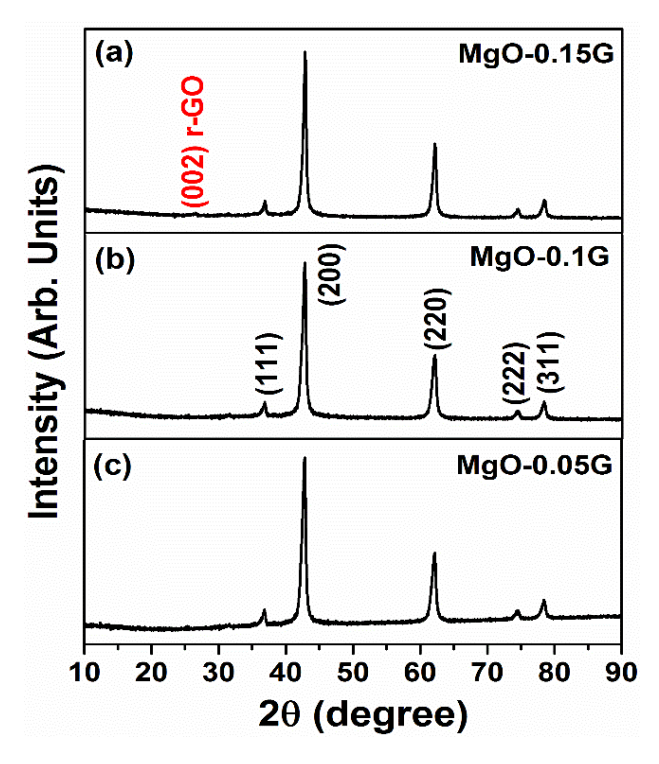
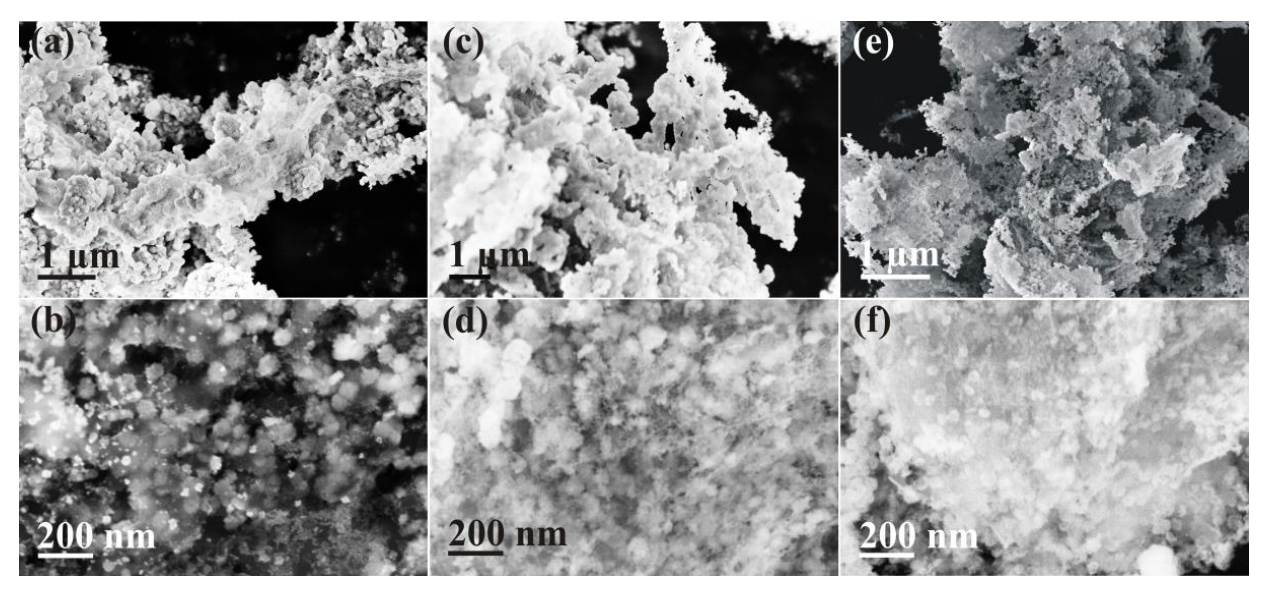
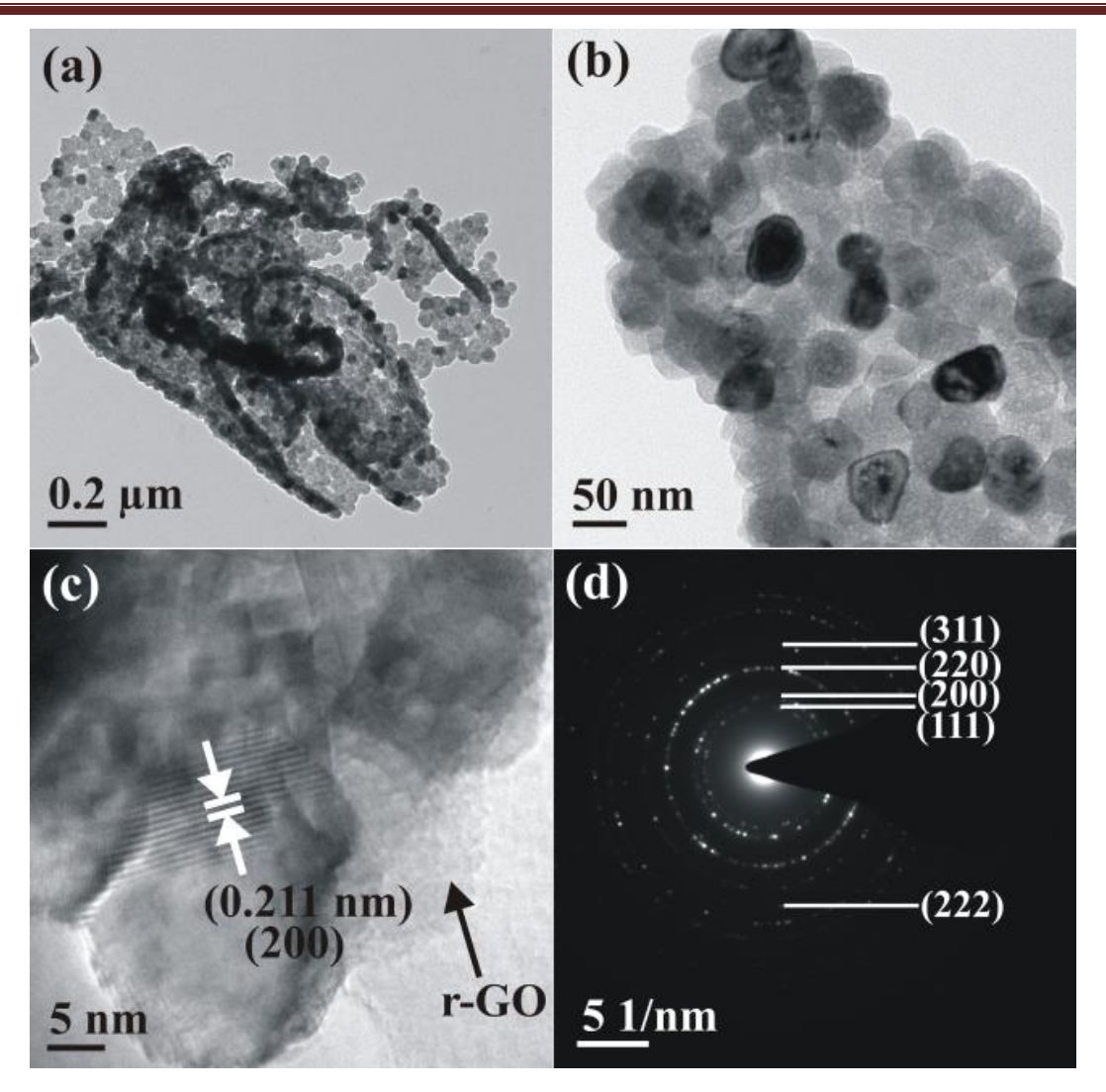


Figure 4.37. XRD patterns of (a) MgO-0.15G, (b) MgO-0.1G and (c) MgO-0.05G.



**Figure 4.38.** Secondary electron micrographs of MgO decorated r-GO composites. (a) Low and (b) high, (c) low and (d) high, (e) low and (f) high magnification micrographs of MgO-0.05G, MgO-0.1G and MgO-0.15G, respectively.



**Figure 4.39.** TEM images of MgO-0.15G. (a) Low, (b) & (c) are high resolution image and (d) diffraction pattern, respectively.

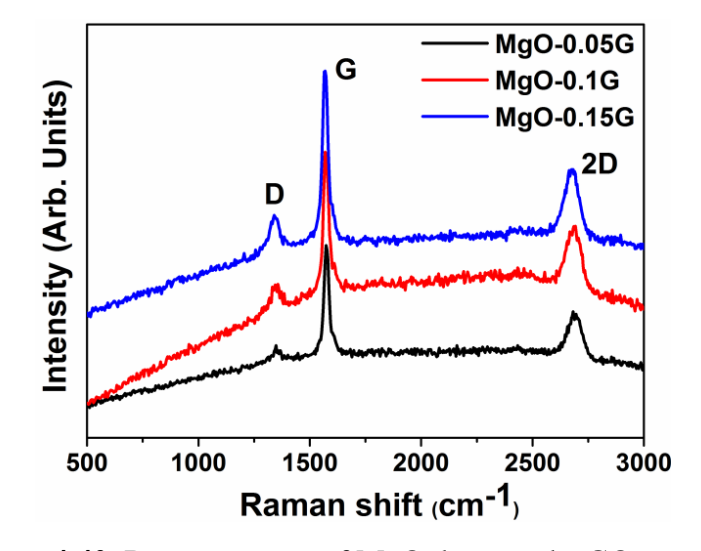
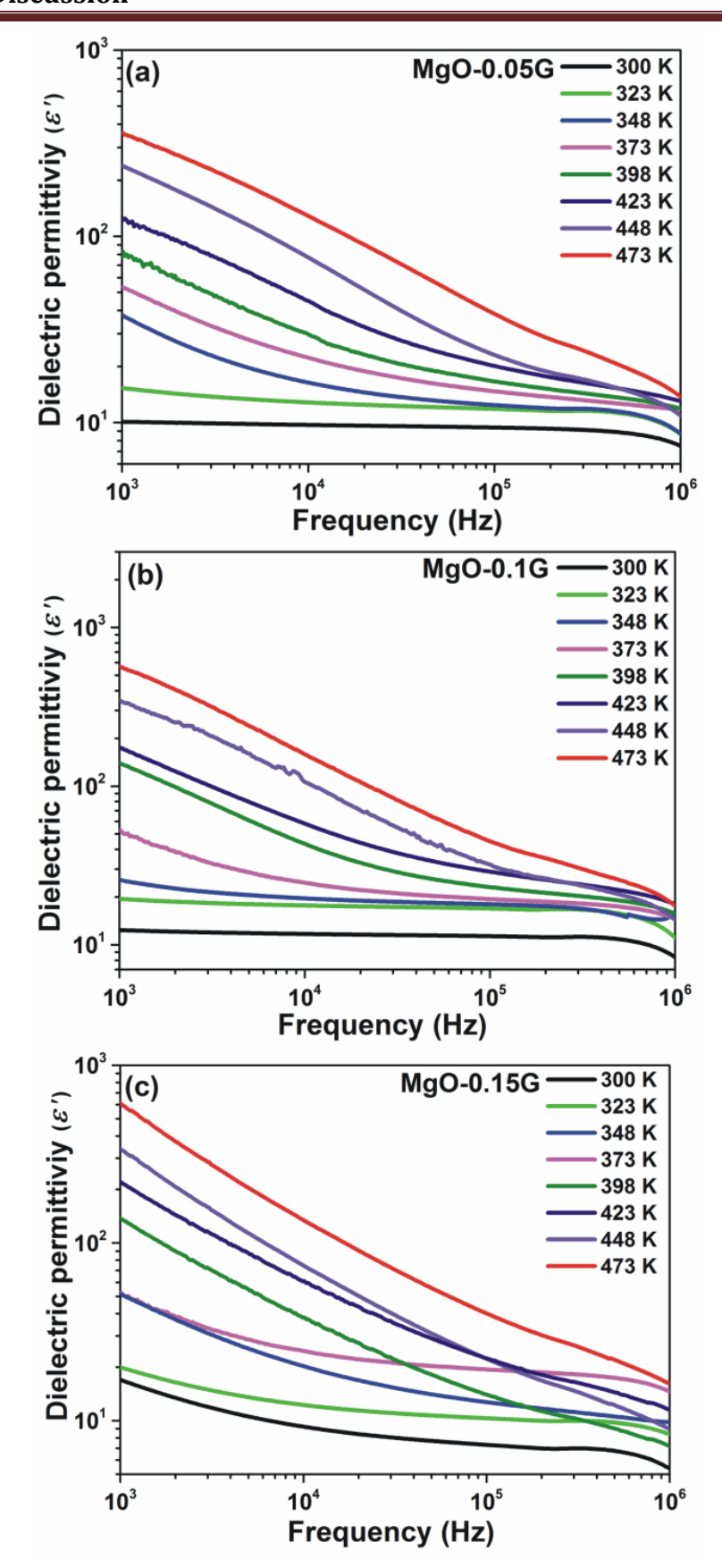


Figure 4.40. Raman spectra of MgO decorated r-GO composites.

#### 4.3.3 Non-Debye relaxation

Fig. 4.41 shows the variation of  $\varepsilon'$  (at fixed temperatures in the range 300-473 K) of MgO decorated r-GO samples as a function of frequency. It can be clearly observed that  $\varepsilon'$  values are high at lower frequencies. It can be also observed that  $\varepsilon'$  values decrease with increasing frequency and increase with increasing temperature. In particular,  $\varepsilon'$  values sharply increased with increasing temperature in the low frequency region when compared to the same in the high frequency region. The measured room temperature  $\varepsilon'$  values at 1 kHz are 10, 12 and 18, which increased to 358, 563 and 612 at 473 K in the case of MgO-0.05, MgO-0.1G and MgO-0.15G, respectively. The enhancement in  $\varepsilon'$  values (radio frequency region) is a function of both orientation and interfacial polarizations and is due to the presence of oxygenated polar functional groups (-COOH, -OH, -CHO, -C=O) as well as defects in the system. The above observations are interesting because it is normally anticipated that with increasing temperature (at a particular frequency) the dipoles retain sufficient thermal energy and follow the applied field direction resulting in enhancement of  $\varepsilon'$  values and this may continue up to a critical temperature beyond which the values may start to decrease [77]. In fact, at lower frequencies the charges have time to accumulate at the conducting regions in the system which causes  $\varepsilon'$  to increase [78] but at higher frequencies the charges may not have sufficient time to accumulate and polarize. Therefore, the relaxation was observed in the frequency range 10<sup>3</sup>-10<sup>5</sup> Hz with a shift towards high frequencies at higher fixed temperatures. In general, two relaxation processes namely orientational and interfacial relaxations related to orientation and interfacial polarizations, respectively, are observed in the presence of an applied electric field. At low fixed temperatures, relaxation is observed towards higher frequencies (the step in Fig. 4.41). At higher fixed temperatures, the step shifted towards higher frequencies indicating thermally activated process in the samples in this frequency region. The high  $\varepsilon'$  value at low frequency in the case of MgO decorated r-GO composites is attributed to the charge carriers' accumulating at the numerous interfaces between r-GO sheets and MgO particles throughout the bulk of the material; this is a consequence of Maxwell-Wagner interfacial polarization in the presence of an electric field. Further, dielectric loss ( $\epsilon''$ ) Vs temperature at fixed frequencies is shown in **Fig. 4.42**, which clearly shows multi (at least two are discernable) relaxation peaks which is a clear indication of the presence of non-Debye relaxation in the MgO decorated r-GO nanocomposites. The confirmation of non-Debye relaxation needs a critical evaluation of the data and therefore the data was fit with HN relaxation function to further understand the non-Debye relaxation.



**Figure 4.41.** Dielectric permittivity ( $\epsilon$ ') of (a) MgO-0.05G, (b) MgO-0.1G and (c) MgO-0.15G as a function of frequency at fixed temperatures in the range 300-473 K.

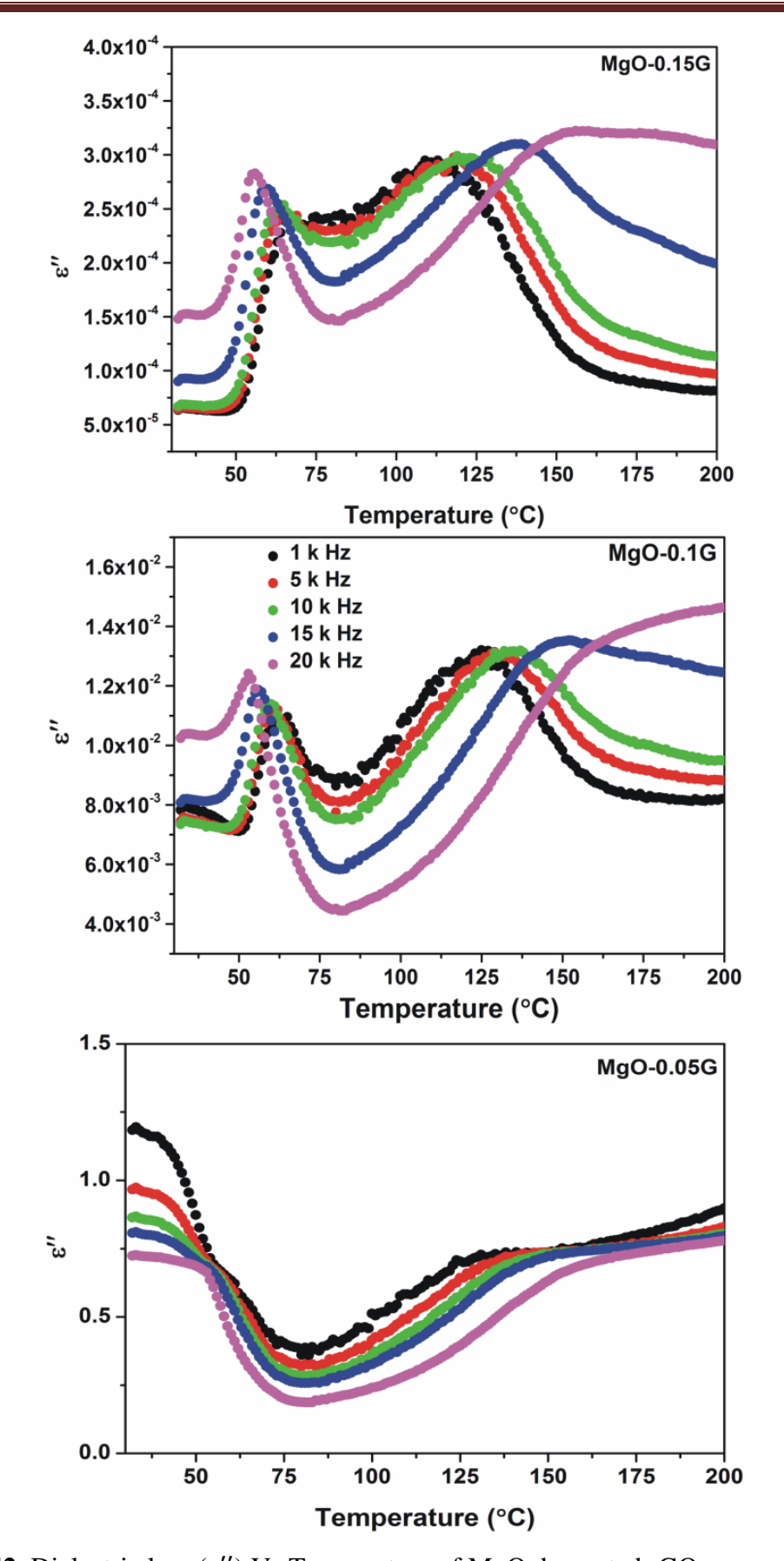
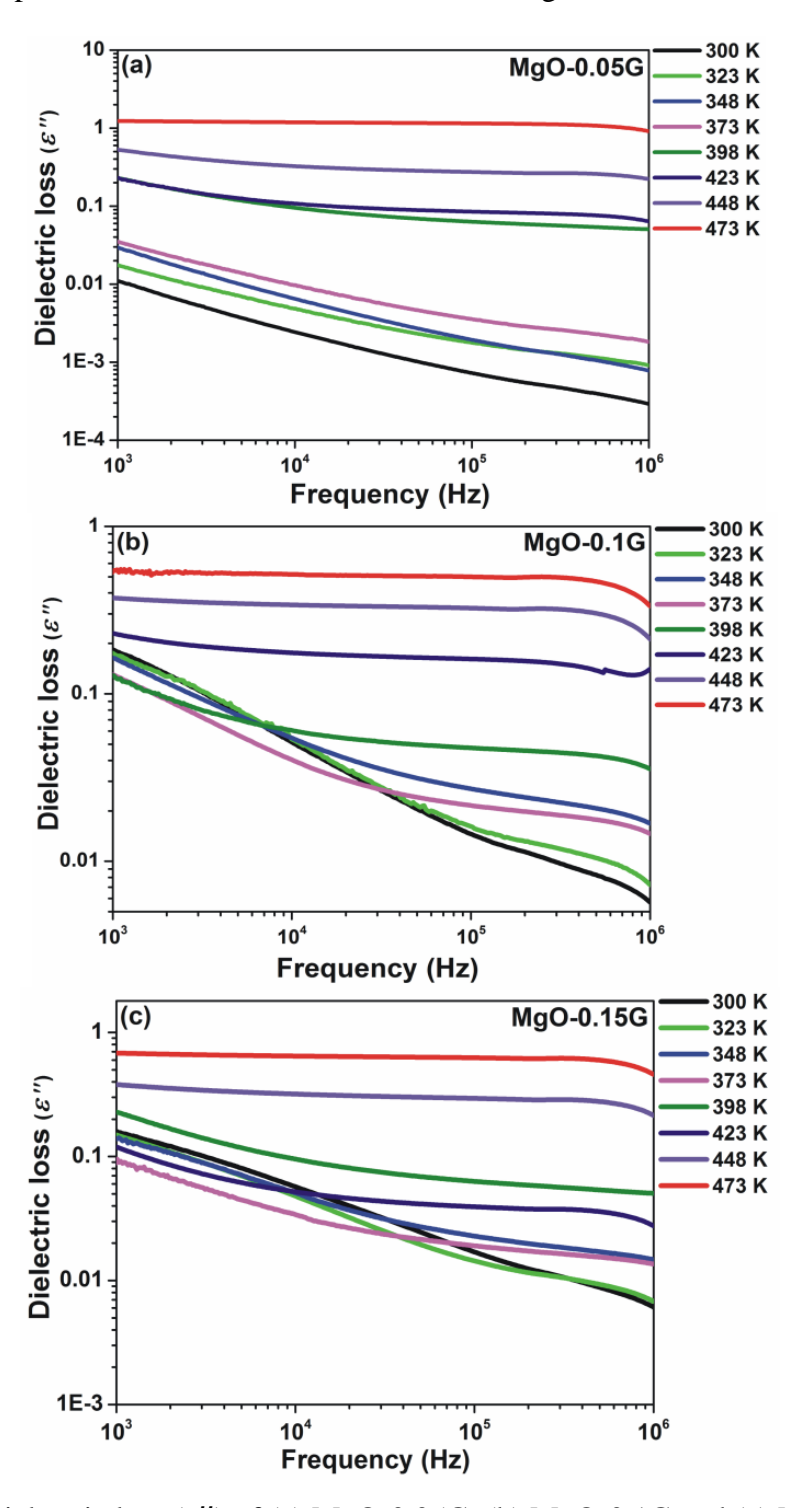


Figure 4.42. Dielectric loss ( $\epsilon''$ ) Vs Temperature of MgO decorated rGO nanocomposites at fixed frequencies in the range 1-20 kHz.

**Fig. 4.43** shows the variation of  $\varepsilon''$  (at fixed temperatures in the range 300-473 K) of the samples as a function of frequency. It is clear from **Fig. 4.43** that high dielectric losses are observed at the highest fixed temperature of 473 K rather than at room temperature. Also, the losses are observed to be decreasing with increasing frequency while the relaxation is due to inappropriate response of the accumulated interfacial charge carriers.



**Figure 4.43.** Dielectric loss ( $\epsilon''$ ) of (a) MgO-0.05G, (b) MgO-0.1G and (c) MgO-0.15G as a function of frequency at fixed temperatures.

All in all, it has been noticed that the MgO decorated r-GO samples exhibit low  $\varepsilon'$  values at 300 K and high  $\varepsilon'$  values at 473 K. Also the high  $\varepsilon'$  values are due to the existence of strong interfacial polarization. At this juncture it is very interesting to know, up to which frequency the interfacial polarization is sustained. For this purpose and owing to the nature of the dielectric dispersion curves, HN relaxation model [79,80], which is pertaining to non-Debye type relaxation in composite systems has been applied on the experimental data. HN equation [80,81] is given by

$$\varepsilon^* = \varepsilon_{\infty} + \frac{\Delta \varepsilon}{(1 + (i\omega\tau_1)^{\alpha})^{\beta}} + \frac{\Delta \sigma_{dc}}{i\omega} \left( 1 - \frac{1}{1 + (i\omega\tau_2)^{\gamma}} \right)$$
 (Equation 4.1)

where  $\varepsilon_{\infty}$  indicates the instantaneous dielectric constant,  $\Delta \varepsilon = \varepsilon_0 - \varepsilon_{\infty}$  is dielectric relaxation strength,  $\tau_1$  and  $\tau_2$  are the relaxation times, and  $\alpha$ ,  $\beta$  and  $\gamma$  are parameters expressing distribution of relaxation times. In order to analyze the dielectric data using the HN model, it is necessary to incorporate the temperature dependence of the complex modulus. The third term in Equation (1) corresponds to the dc conductivity relaxation which is related to the interfacial polarization.  $\sigma_{dc}$  is due to the unrestricted motion of free charge carriers. It is well known that both interfacial and orientation polarizations usually occur in the radio frequency region (i.e., in the range  $10^1$ - $10^8$  Hz). Orientation polarization occurs when charges are locally bound in molecules. If the system consists of polar molecules (dipoles), it is easier to polarize (orient) them in the field direction. Interfacial polarization occurs when there is accumulation of charges at the interfaces between two materials or between two regions within a material. Interfacial polarization also effects free charges [82].

Interfacial polarization (Maxwell-Wagner type) polarization usually occurs at the interface of inhomogeneous regions with different conductivities. It is typically interpreted as a combination of the conduction and dipolar polarization effects and is related to the 3<sup>rd</sup> term of **Eq. 4.1**. This polarization occurs when the motions of the migrating charges (surface- or free-charge carriers) are impeded and the charges are trapped at the interfaces in the material. In Equation (1), the combination of first two terms corresponds to orientational polarization and third term corresponds to interfacial polarization [40,79]. However  $\alpha$  and  $\beta$  values play a crucial role to certify the type of relaxation in composite systems. For specific examples,  $\alpha = 1$ ,  $\beta = 1$  corresponds to Debye relaxation,  $\alpha \neq 1$ ,  $\beta = 1$  corresponds to Cole-Cole relaxation and  $\beta \neq 1$ ,  $\alpha = 1$  corresponds to Cole-Davidson relaxation [83,84], and  $\alpha \neq 1$  and  $\beta \neq 1$  corresponds to HN relaxation [80]. The last case (i.e., non-Debye relaxation) is typically observed in polymer nanocomposites with carbonaceous fillers [85,86] and

therefore in all such cases, the experimental dielectric data is usually fitted with HN equation to understand the intricate polarization behavior of the material. In the present case as PVA was used as a binder in preparing the pellets of the samples for measuring the dielectric properties, polarization behavior of the samples in the radio frequency region (i.e., in the range 10<sup>1</sup>-10<sup>8</sup> Hz) will be influenced (i.e., PVA is anticipated to strengthen interfacial polarization along with r-GO content) by the presence of PVA. In order to understand the interfacial polarization phenomenon in the samples, the third term of the HN function was separately used to fit experimental dietetic data ( $\varepsilon'$ ) at room temperature (300 K) and as well high temperature (473 K). Fig. 4.44 shows the theoretical fitting of HN function along with the experimental dielectric data. In order to study interfacial phenomena using HN function it is necessary to consider fixed temperature dependence data. The overall HN function is well fitted with the experimental dielectric data both at room temperature and at 437 K as shown in Figs. 4.44 (a), (c), and (e) and Figs. 4.44 (b), (d), and (f), respectively. However, when fitted with the 3<sup>rd</sup> term of HN function (interfacial polarization term), the theoretical fit deviates from experimental data from a particular frequency onwards to a point where the interfacial polarization diminishes while the orientation polarization is still sustained [87,88]. At room temperature, the theoretical fit deviates from the experimental data at low frequencies of 1254, 1580 and 1760 Hz in the case of MgO-0.05G, MgO-0.1G and MgO-0.15G, respectively, which is an indication of the existence of strong interfacial polarization up to these frequencies (response of surface charge/free charge carriers with applied filed) and above which interfacial relaxation (out of phase response) is observed. Besides this, an increase in r-GO content would shift the theoretical interfacial polarization fit towards higher frequencies (i.e., from 1254 to 1760 Hz), which reveals that the interfacial polarization is stronger when more r-GO is present in the sample because greater the r-GO content, greater is the number of charge carriers (due to increase in number of functional groups). But at 473 K, theoretical interfacial polarization fit deviated from the dielectric data and shifted towards much higher frequencies of 2445, 5051 and 2774 Hz in MgO-0.05G, MgO-0.1G and MgO-0.15G cases respectively, in comparison to the respective theoretical fit frequencies at 300 K. The large shift in interfacial polarization fit frequencies at 473 K is reflected in the enhancement of  $\varepsilon'$  values (as shown in **Fig. 4.41**), which can be considered as a consequence of strengthened interfacial polarization. Overall and third term HN fitting parameters at 300 and 473 K are listed in Table 4.5 and Table 4.6, respectively, which clearly show that interfacial polarization fitting parameters are consistent with the experimental data.

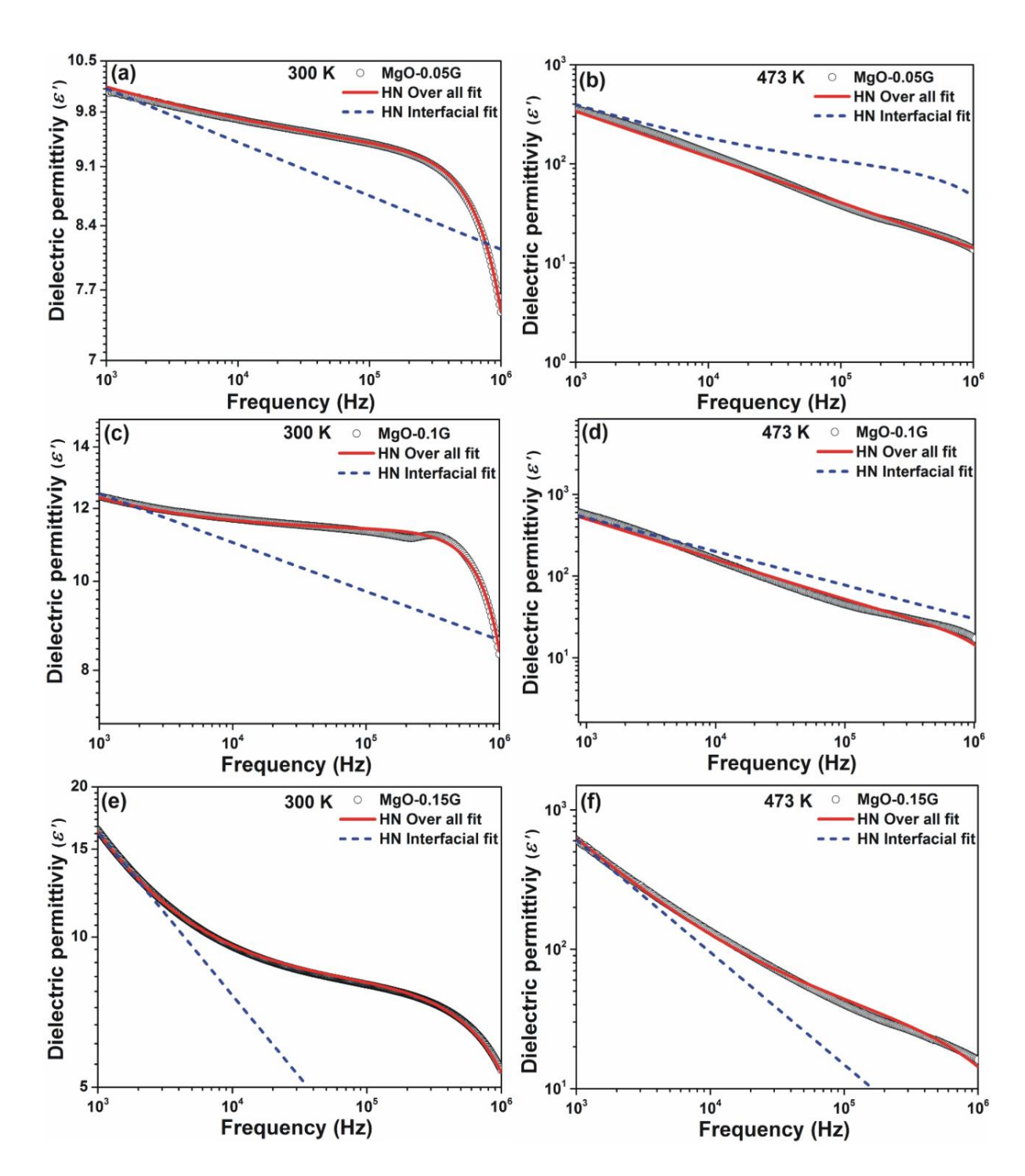


**Figure 4.44.** The theoretical fitting of HN function (red line represents overall fit and dotted blue line represents interfacial polarization fit) to the experimental dielectric data of MgO/r-GO composites. (a), (c), and (e) correspond to 300 K and (b), (d) and (f) correspond to 473 K.

It is important to note from **Table 4.6** that the relaxation times ( $\tau_1$  and  $\tau_2$ ) at high temperature (473 K) are lower in comparison to the same at room temperature. This is a consequence of quick orientation of surface charge carries/dipoles/molecules in the field direction. This has also reflected in the enhancement in the respective dielectric permittivity values. Moreover, the  $\tau_2$  values (which are related to the interfacial relaxation) are in the order of  $10^{-7}$  to  $10^{-8}$  (at 473 K) and  $10^{-4}$  to  $10^{-5}$  (at 300 K), which clearly indicate the existence of stronger interfacial polarization at high temperature than at room temperature.

**Table 4.5.** Overall HN fitting parameters at 300 and 473 K.

Parameters	Room temperature (300 K)		
	MgO-0.05G	MgO-0.1G	MgO-0.15G
$\mathcal{E}_{\infty}$	7.855	8.0486	9.0729
$\Delta arepsilon$	124.04	293.08	342.21
$ au_1$	0.0082	0.0043	0.0012
α	0.92	0.85	0.95
β	0. 18	0.52	0.58
$\Delta\sigma_{dc}$	5.319×10 <sup>-7</sup>	1.695×10 <sup>-7</sup>	1.842×10 <sup>-8</sup>
$ au_2$	5.566×10 <sup>-4</sup>	3.95×10 <sup>-4</sup>	9.652×10 <sup>-5</sup>
γ	0.78	0.15	0.32
	High temperature (473 K)		
	MgO-0.05G	MgO-0.1G	MgO-0.15G
$\mathcal{E}_{\infty}$	18.49	33.52	70.21
$\Delta arepsilon$	428.45	600.10	859.22
$ au_1$	0.00091	0.00076	0.00056
α	0.77	0.95	0.89
β	0. 32	0.64	0.43
$\Delta\sigma_{dc}$	1.26×10 <sup>-5</sup>	2.91×10 <sup>-6</sup>	1.27×10 <sup>-6</sup>
$ au_2$	7.765×10 <sup>-7</sup>	4.95×10 <sup>-8</sup>	2.652×10 <sup>-8</sup>
γ	0.68	0.82	0.83

**Table 4.6.** Third term HN fitting parameters at 300 and 473 K.

Parameters	At room temperature (300 K)		
	MgO-0.05G	MgO-0.1G	MgO-0.15G
$\Delta\sigma_{dc}$	5.236×10 <sup>-7</sup>	1.728×10 <sup>-7</sup>	1.865×10 <sup>-8</sup>
$ au_2$	5.652×10 <sup>-4</sup>	4.10×10 <sup>-4</sup>	9.568×10 <sup>-5</sup>
γ	0.78	0.45	0.32
Parameters	At high temperature (473 K)		
	MgO-0.05G	MgO-0.1G	MgO-0.15G
$\Delta\sigma_{dc}$	$1.42 \times 10^{-4}$	2.85×10 <sup>-5</sup>	1.68×10 <sup>-5</sup>
$ au_2$	7.625×10 <sup>-7</sup>	4.654×10 <sup>-8</sup>	2.725×10 <sup>-8</sup>
γ	0.54	0.89	0.86

#### 4.4 NiO decorated r-GO

#### 4.4.1 General comments

Developing giant dielectric permittivity ( $\varepsilon'$ ) exhibiting materials has always been fascinating both science and technology wise. These materials play a crucial role in electronic circuits because they are used to fabricate essential devices such as memory devices and capacitors [61,89]. In this context, high dielectric constant exhibiting materials such as perovskites namely Pb(Zr,Ti)O<sub>3</sub> and PbMg<sub>0.33</sub>Nb<sub>0.66</sub>O<sub>3</sub> whose ε' values are greater than 1000 [90,91], lead free material such as CaCu<sub>3</sub>Ti<sub>4</sub>O<sub>12</sub> ( $\varepsilon' \sim 10^5$ ) [92], and NiO based ceramics [93-100] were developed. NiO based ceramics are non-perovskite and non-ferroelectric materials with the general formula A<sub>x</sub>B<sub>y</sub>Ni<sub>1-x-y</sub>O (where A is monovalent element namely K, Na and Li, and B is Al, Ti, Ta, Si and Fe). These ceramics show high  $\varepsilon'$  values in the range of  $10^3-10^5$  [93-100] and therefore attracted considerable attention in recent years. Moreover, the dielectric properties of the NiO based ceramics can be varied by changing A and B in the above mentioned formula. However, the reasons for the high dielectric permittivity are still unclear while the synthesis techniques/methods used to obtain these ceramics are complicated and cumbersome (for example: sintering temperatures are very high). Therefore, it is important to search for either a new class of giant dielectric constant exhibiting materials or use the existing knowledge, for example percolation effect of the fillers on the dielectric behavior as observed in polymer nanocomposites filled with r-GO [101,102]. However, the problem with these polymer nanocomposites is the quite high dielectric loss associated with them. Nonetheless, materials such as graphene-BaTiO<sub>3</sub>/ferroelectric polymer composite [103] and polyvinylidene fluoride composites based on sandwich structured of MnO<sub>2</sub>/graphene/MnO<sub>2</sub> [104] have been prepared overcoming the problem of high dielectric loss. Moreover, it was suggested that metal oxides in such polymers play a key role in order to control the restacking of r-GO sheets [104]. In this direction too few works were taken up to improve the dielectric permittivity while keeping the dielectric loss as minimum as possible [105-107]. Another interesting concept that was used to achieve giant dielectric permittivity was to create trap induced capacitance owing to impurity levels in r-GO [108,109]. The trap induced capacitance model was used to explain the high dielectric permittivity in Co doped r-GO and graphene/ZnCo<sub>2</sub>O<sub>4</sub> nanocomposite [108,109]. In view of the above presented works, NiO decorated r-GO nanocomposites were chosen to study the percolation effects on their dielectric behavior, if any. Other dielectric characteristics and the resistance to charge carriers pertaining to NiO decorated r-GO nanocomposites are also explained.

### 4.4.2 Structural, morphological, and phase analysis

XRD diffractograms of different NiO decorated r-GO nanocomposites in comparison to NiO are shown in **Fig. 4.45**. In all the nanocomposite cases, the peaks are indexed to cubic NiO phase (JCPDS No. 03-65-2901). The (002) diffraction peak at  $2\theta = \sim 26.4^{\circ}$  corresponds to the presence of r-GO. It is observed that with an increase in r-GO wt % in the nanocomposites, the intensity of the diffraction peaks corresponding to NiO decreased and the peaks broadened too. On the other hand, the diffraction peak at  $2\theta = \sim 26.4^{\circ}$  was more discernible in the case of nanocomposites with higher r-GO wt %. NiO crystallite sizes were calculated using the typical Debye Scherrer's formula and were found to be 55, 42, 35, 28, 14, 9 and 7 nm in the case nanocomposites with 0.0, 0.4, 0.8, 1.2, 1.6, 2.4 and 2.8 wt % of r-GO, respectively. It is clear that the crystallite size decreased with increase in r-GO content, which is consistent with previous reports on percolation controlled ceramic-graphene composites [110]. Additionally, it was also observed that NiO peak positions slightly shifted towards lower angle side indicating that lattice of NiO is strained in the nanocomposites.

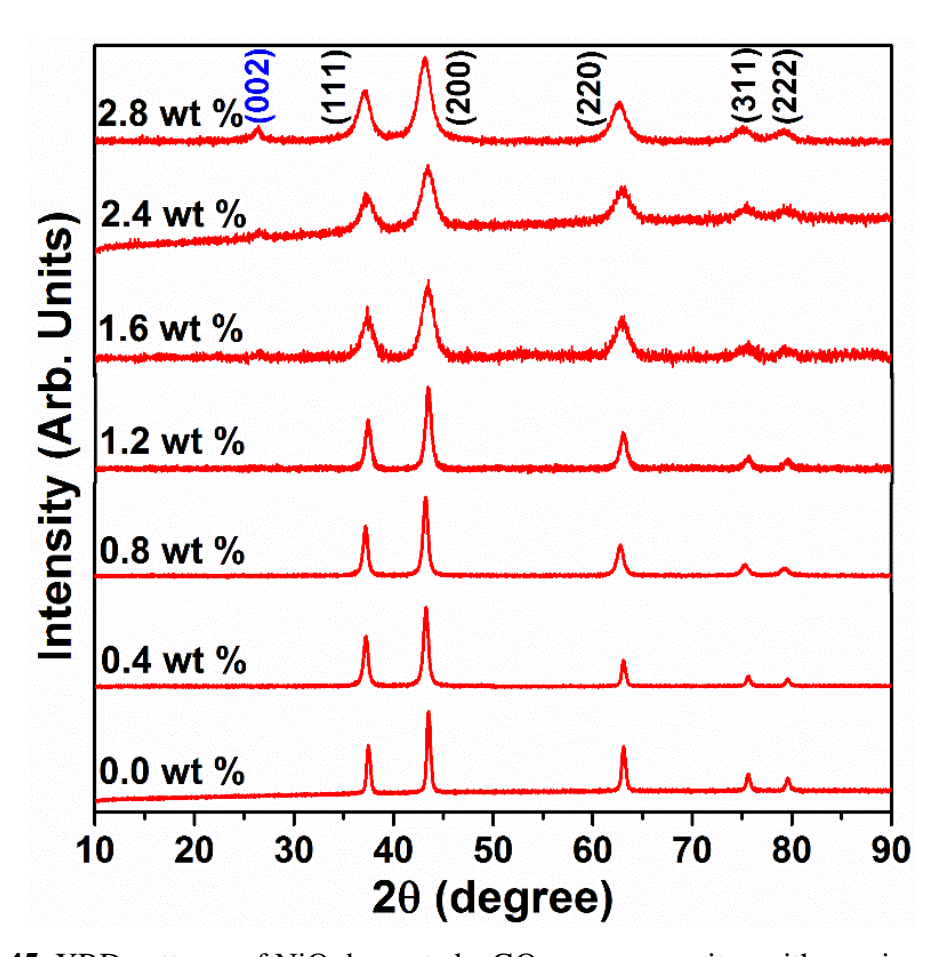


**Figure 4.45.** XRD patterns of NiO decorated r-GO nanocomposites with varying wt % of r-GO (ranging from 0.0 to 2.8 wt %).

The secondary electron micrographs of NiO and NiO-0.024G nanocomposite are shown in **Fig. 4.46**. It is clearly observed in **Fig. 4.46(a)** that the size of NiO nanoparticles is of few nm and **Figs. 4.46(b)** and (c) clearly show that the surface and cross-section of r-GO sheets are uniformly decorated with NiO particles. The decoration was further confirmed by TEM images (of NiO-0.024G composite) which are shown in **Fig. 4.47**. The high magnification TEM image **Fig. 4.47(b)** clearly shows uniform distribution of Ni nanoparticles on r-GO. **Fig. 4.47(c)** shows (111) NiO places with a lattice spacing of 0.24 nm. The electron diffraction pattern in **Fig. 4.47(d)** indicates polycrystalline nature of NiO nanoparticles.

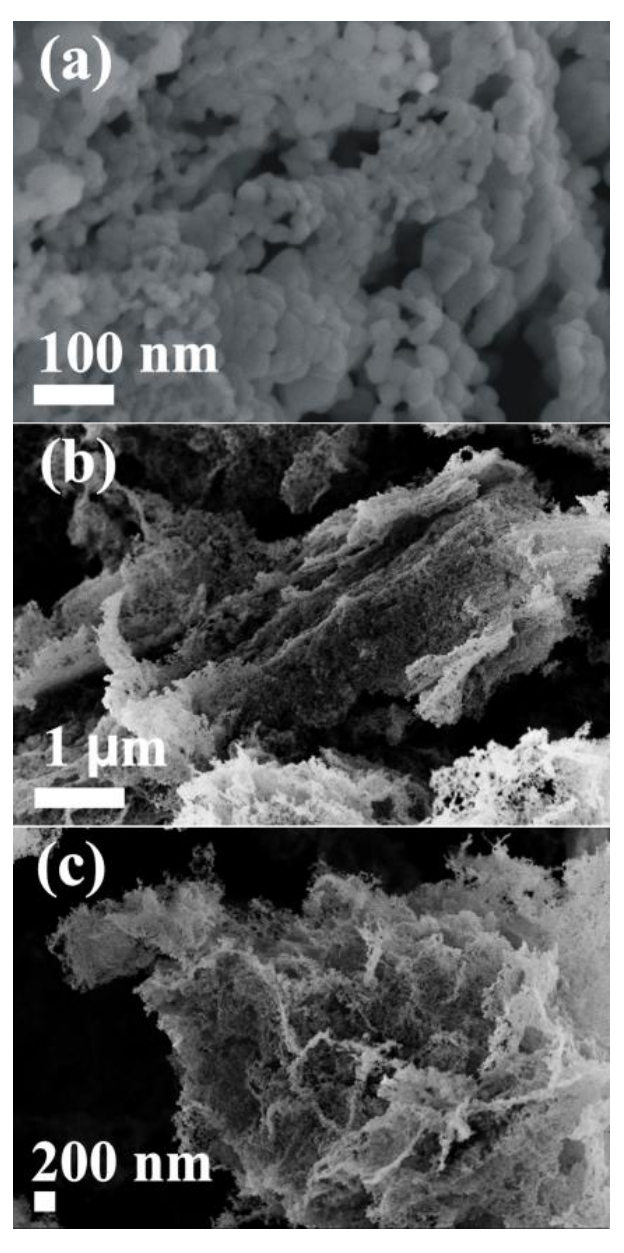


**Figure 4.46.** Secondary electron micrographs of (a) NiO (0.0 wt %), (b) low and (c) high magnification images of NiO-0.024G (2.4 wt % r-GO) composite.

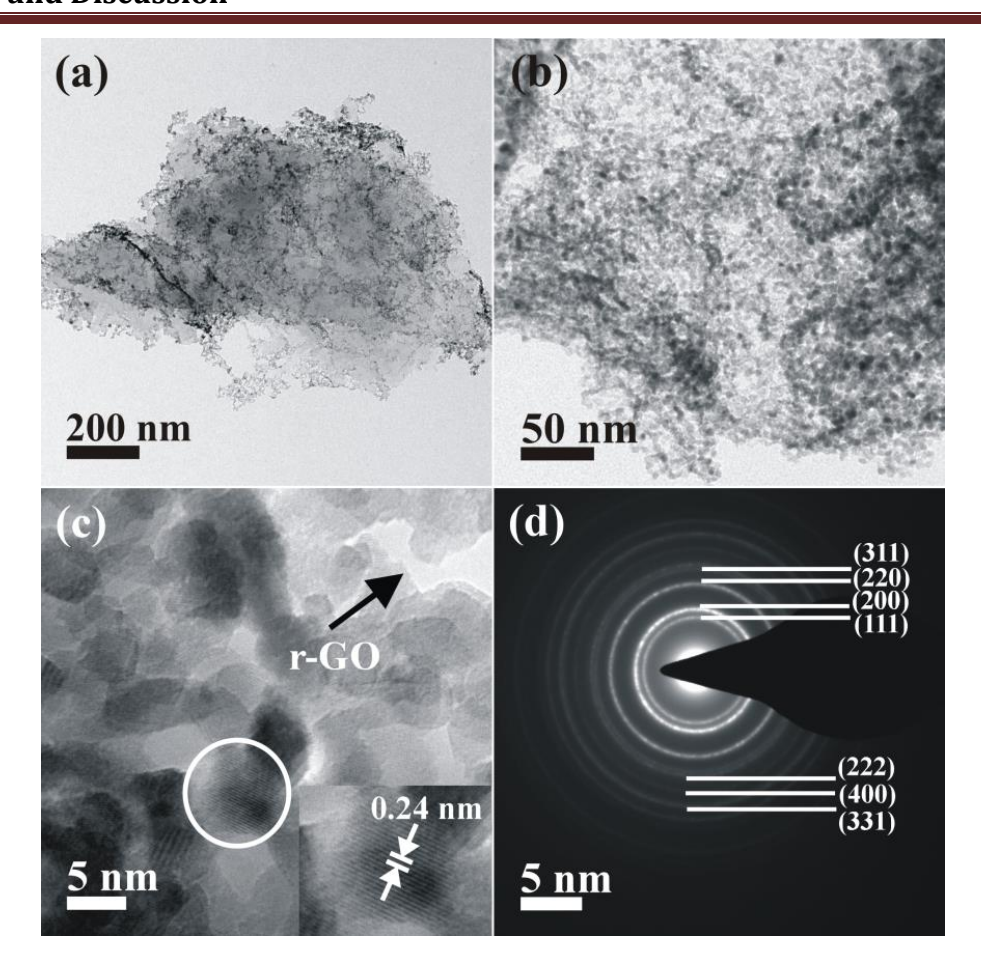


**Figure 4.47.** TEM micrographs and corresponding diffraction pattern of NiO decked r-GO. (a) low, (b) and (c) high resolution image and its (d) diffraction pattern of NiO-0.024G, respectively.

**Fig. 4.48** shows FTIR spectra of r-GO and NiO decked r-GO composites (0.8 wt %, 1.6 wt % and 2.4 wt % of r-GO). The presence of different oxygen functional groups in r-GO and in nanocomposites was confirmed. The bands at 3400 cm<sup>-1</sup>, 1720 cm<sup>-1</sup>, 1220 cm<sup>-1</sup> and 1060 cm<sup>-1</sup> correspond to O-H stretching vibrations. The band at corresponds to stretching vibrations of C=O while the sharper band at corresponds to stretching vibrations of C-OH and the band at corresponds to C-O stretching vibrations [52,53]. Low intensity of O-H band is attributed to deoxygenation. Similar peaks were also observed in the case of other composites; to avoid redundancy, they are not shown here. FTIR spectra clearly indicated that the bands corresponding to oxygen functionalities experienced a chemical reduction as evidenced by the decrease in intensity and/or suppression of different bands related to oxygen functionalities and also due to the decoration of NiO nanoparticles on r-GO sheets. FTIR bands corresponding to NiO were observed in range 410-465 cm<sup>-1</sup> in all the nanocomposites consistence with previous reports [111,112].

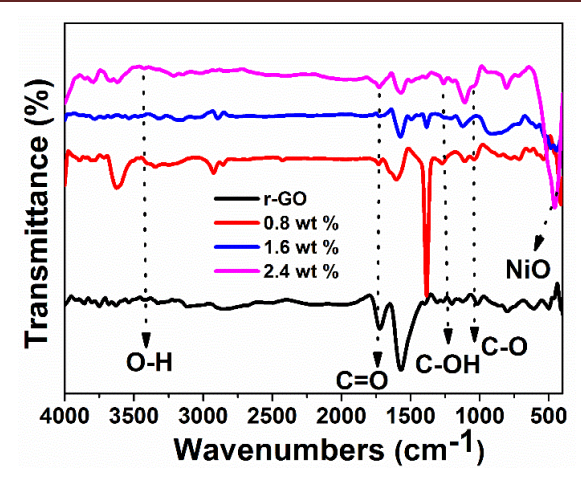


Figure 4.48. FTIR spectra of r-GO and NiO decked r-GO composites.

Presence of NiO in the nanocomposites was further confirmed by Raman scattering. Raman spectra of NiO decorated r-GO composites are shown in **Fig. 4.49**. Raman bands namely G (1575-1580 cm<sup>-1</sup>), D (1345-1350 cm<sup>-1</sup>) and 2D (2680-2690 cm<sup>-1</sup>) bands of r-GO are observed [13,16]. Apperance of M-K band at 2450 cm<sup>-1</sup> in the case of nanocomposites indicates the decoration of NiO particles on r-GO sheets. The appearance of first- and second- order phonon scattering from NiO in the nanocomposites is attributed to large exchange interactions in the nanocomposites [113]. The intense first-order scattering from the optical phonons was observed in between 495-552 cm<sup>-1</sup>. This band corresponds to the longitudinal optical (LO) mode in NiO. With increasing r-GO wt % this band is shifted towards lower wave number side. This is attributed to the columbic interactions between NiO and functional groups on r-GO sheets. The second order longitudinal optical (2LO) mode in NiO was observed around 1070 cm<sup>-1</sup> only in the case of NiO and 0.4 wt % of r-GO nanocomposite. In the case of all other samples, this peak was not discernable; this is attributed to the restricted motion of phonons owing to the increase in decoration of NiO on r-GO or vice-versa.

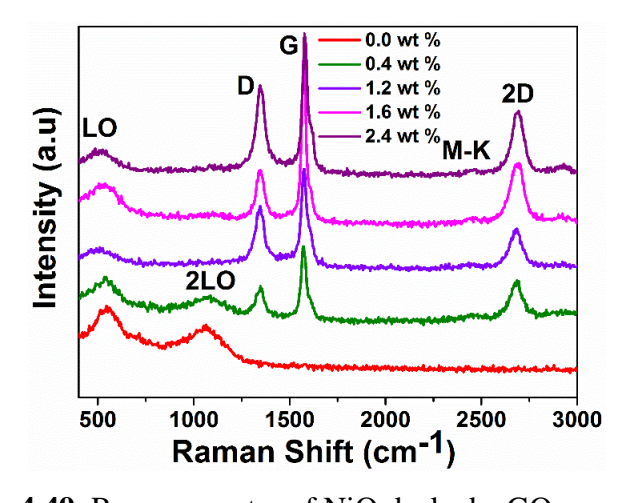
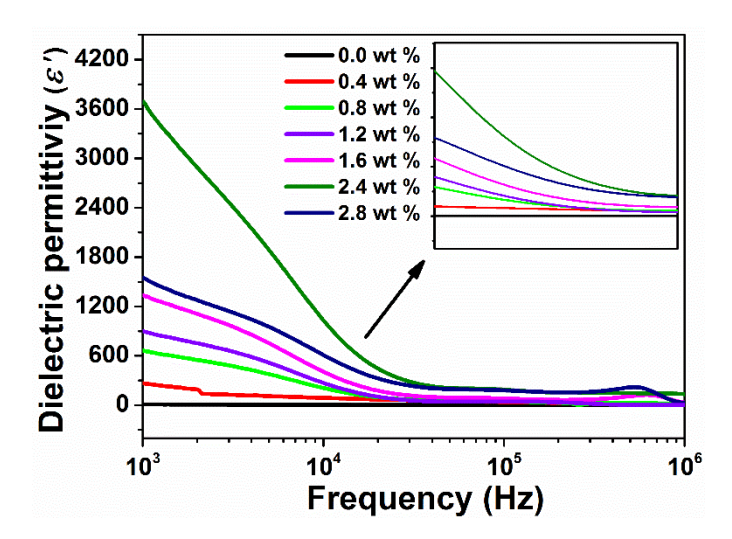


Figure 4.49. Raman spectra of NiO decked r-GO composites.

### 4.4.3 Giant dielectric permittivity and percolation effect

The dielectric permittivity ( $\epsilon'$ ) of NiO decked r-GO nanocomposites (with varying r-GO wt % from 0.0 to 2.8 wt %) as function frequency is shown in **Fig. 4.50**. It is observed that  $\epsilon'$  of composites increased drastically with increasing r-GO wt % (from 0.0 wt % to 2.4 wt %) and reached a percolation threshold ( $f_c$ ) at 2.4 wt % of r-GO and then decreased dramatically at 2.8 wt % of r-GO.  $\epsilon'$  values at 1 kHz frequency are 9.3, 264, 665, 898, 1335, 3688, and 1548 in case of NiO, and 0.4 wt %, 0.8 wt %, 1.2 wt % 1.6 wt % 2.4 wt %, and 2.8 wt % of r-GO containing NiO decked r-GO nanocomposites, respectively. The highest  $\epsilon'$  value is nearly 390 times to that of bare NiO value [94]. This large enhancement in  $\epsilon'$  value near  $f_c$  is 3688 at 2.4 wt % of r-GO (threshold weight percentage  $m_c = 2.4$ ).  $\epsilon'$  value decreased by nearly 42% at 2.8 wt % of r-GO in comparison to that at 2.4 wt % of r-GO. Conventionally, a power law (**Eq. 4.2**) is used to describe the relationship between  $\epsilon'$  and the volume fraction of the r-GO in the nanocomposites when the filler content is approaching the percolation threshold [114].



**Figure 4.50.** Dielectric permittivity Vs frequency of NiO decorated r-GO nanocomposites with varying r-GO wt %.

$$\mathcal{E} \alpha (f_c - f_{r-GO})^{-s}$$
 for  $f_{r-GO} < f_c$  ...... (Equation 4.2)

where  $\mathcal{E}$  is dielectric permittivity of the composite,  $f_c$  is critical volume fraction at percolation threshold and  $f_{r-GO}$  is volume fraction of r-GO filler in the nanocomposite and 's' is the critical exponent. For general understanding, the volume fraction (f) is replaced by weight percentage or mass percentage (m) and the above equation is written as

$$\mathcal{E} \alpha (m_c - m_{r-GO})^{-s} for m_{r-GO} < m_c$$
 ..... (Equation 4.3)

where  $m_c$  is critical weight percentage or threshold and  $m_{r-GO}$  is weight percentage of r-GO.

In the case of nanocomposites presented in the previous sections, the highest dielectric permittivity value is 667. But here, a giant dielectric permittivity was observed. The reasons for this observation is justified as follows: the factors namely, large aspect ratio of r-GO sheets and their unique layered structure gives an advantage in the formation of a large number of parallel-board micro-capacitors [115-119], presence of polar oxygen containing functional groups like -OH, -CHO, -CO, -COOH etc., on r-GO [41,62] and presence of defects promote a strong interfacial polarization (Maxwell-Wagner interfacial polarization) between NiO and r-GO in the nanocomposites have collectively contributed to the increase in the dielectric permittivity of NiO decorated r-GO nanocomposites with increasing content of r-GO. It should also be noted that dielectric permittivity may also depend on grain size [120]. In general, the dielectric permittivity increases with decreasing grain size and reaches a maximum value and thereafter decreases with decreasing grain size [120]. In the present study it was observed that  $\varepsilon'$  increases and reaches a maximum value 3688 at a grain size of ~9 nm and then decreases. However, the grain size of NiO is strongly influenced by r-GO wt % in the nanocomposites and it is observed that grain size decreased with increasing r-GO wt % which is consistent with a previous report [110]. It is also necessary to discuss about the microstructure of the nanocomposite at the percolation threshold. At the threshold, r-GO sheets in NiO decorated r-GO nanocomposite are closely arranged but remained isolated and electrically insulated due to the presence of NiO nanoparticles on/between the neighboring few-layered r-GO nanosheets (number of layers in each r-GO was ~6). In presence of external electric field, there is a greater tendency for charge polarization within conjugated r-GO nanosheets on a long-range order, and this heterogeneous system could be treated as many parallel-board micro-capacitors connected to each other and as a consequence the microstructure also contributes to the giant permittivity value. Beyond percolation threshold, dielectric permittivity decreases owing to conductive nature of nanocomposites. All in all, the dielectric behavior follows the percolation theory and obeys a power law. In Eq. 4.3, mc is the percolation threshold wt % of r-GO, 's' is the critical exponent in the insulating  $(m_{r-GO} <$  $m_c$ ) and conducting  $(m_{r-GO} > m_c)$  region, respectively. The best fit of the dielectric permittivity with the log-log plots of the power law gives  $m_c$  as 2.4 and 's' as 0.4 (see the inset in Fig. 4.51); this observation is consistence with previous reports (the universal value for s is 0 to 3) [121,122]. As far as the dielectric loss is concerned, an abrupt increase was observed near the percolation threshold (Fig. 4.51), which is expected due to the formation of conductive paths within the nanocomposites. At r-GO wt % of 2.4, the dielectric loss was

2.52. The dielectric permittivity and dielectric loss values at the percolation threshold are highly beneficial in applications such as electromagnetic-wave absorption [123]. As r-GO wt % increased beyond the percolation threshold the dielectric loss increased to 3.21.

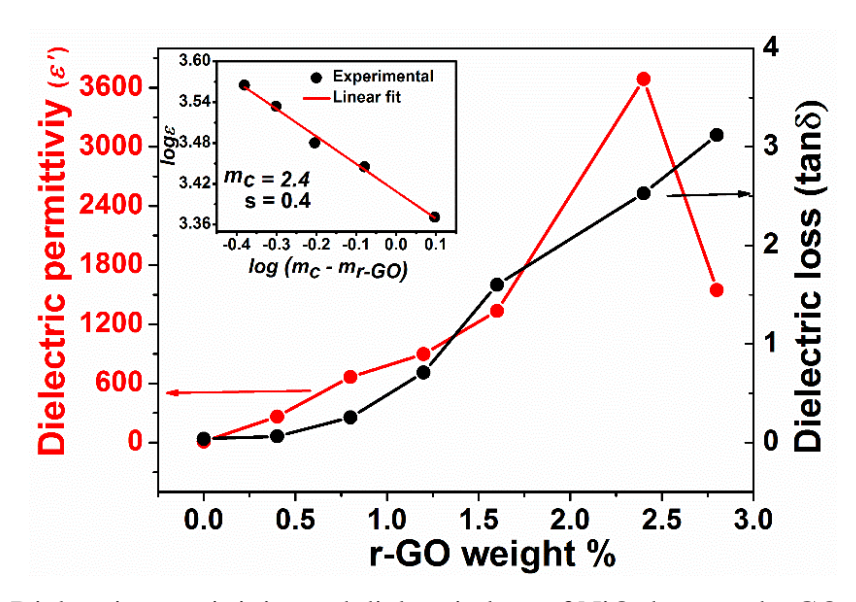


**Figure 4.51.** Dielectric permittivity and dielectric loss of NiO decorated r-GO composites as a function of r-GO wt % at 1 kHz frequency and room temperature. Inset shows the fit curve.

The conductivity ( $\sigma$ ) as a function of  $f_{r-GO}$  at 1 kHz abruptly increases near the critical concentration (2.4 wt % of r-GO) indicating the formation of the continuous conductive network in the nanocomposites. According to the percolation theory [121], dependence of conductivity on the power law is

$$\sigma \alpha (m_c - m_{r-GO})^{-s'}$$
 for  $m_{r-GO} < m_c$  ...... (Equation 4.4)

where  $\sigma$  is effective conductivity,  $m_c$  is the percolation threshold, and s' is the critical exponent in the insulating region. The best fit of the conductivity with Eq. 4.4 yields  $m_c = 2.4$  and s' = 0.25 (please see inset of Fig. 4.52). The exponent value s' is lower than the universal value which is in the range 0.8-1 [121,122]. However, the universal percolation threshold value is 0.16 which is lower than the present case 2.4; this significant change is attributed to the possibility of gaps between and surrounding NiO decorated r-GO sheets due to adhesive forces which in turn leads to losses in the form of conductivity [124,125]. But interestingly dielectric and conductivity data fits yield the same  $m_c$  value.  $\sigma$  of the nanocomposites in the regime  $m_{r-GO} < m_c$  exhibits a strong frequency dependence while its frequency dependence becomes weaker at and after percolation threshold as shown in Fig. 4.53. These characteristics are useful in shielding electromagnetic or radio-frequency interference of electronic devices [123].

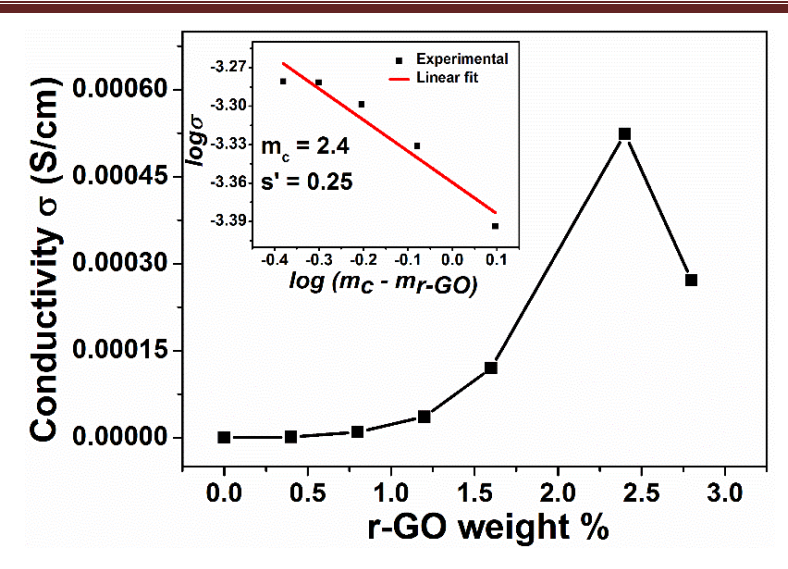


**Figure 4.52**. Effective conductivity of NiO/ r-GO composites as function of r-GO wt % at 1 kHz frequency and room temperature. Inset shows the fit curve with **Eq.4.4**.

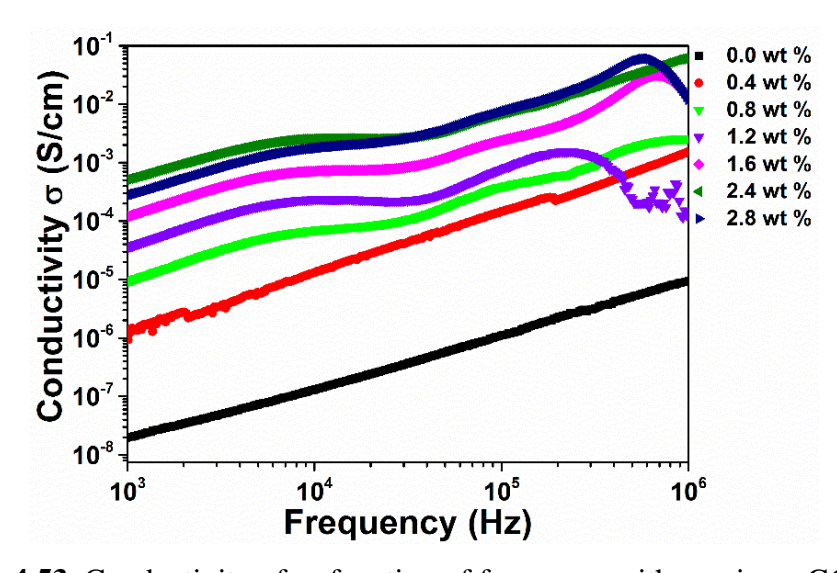
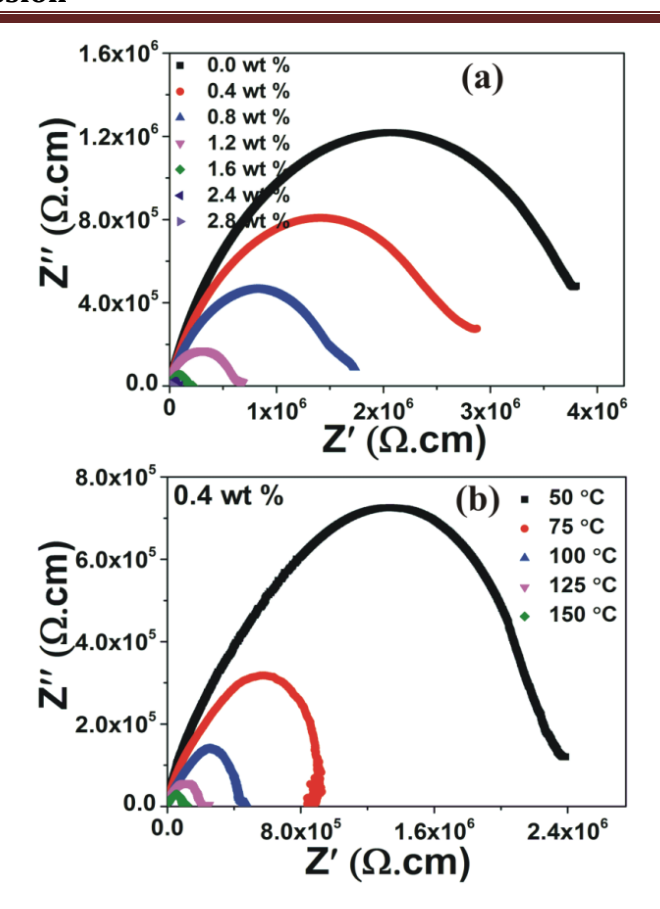


Figure 4.53. Conductivity of as function of frequency with varying r-GO wt %.

Impedance spectroscopy is a good tool in order to understand grain and the grain boundary effects in materials. **Fig. 4.54** shows the impedance spectra of NiO decked r-GO composites at room temperature and varied temperature. It is observed that the complex impendence semicircles have become smaller with increasing r-GO wt % and smaller with also increasing temperature. This suggests that the grain boundaries/interfaces are more active than grains in the nanocomposites. In general, the grain boundary or interface effects on electric conductivity may originate from potential barriers which are ascribed to the functional groups on r-GO sheets covered by NiO. Grain and grain boundary (or interface) resistance values obtained from **Fig. 4.54** are tabulated in **Table 4.7**.



**Figure 4.54**. Impedance spectra of (a) NiO decked r-GO composites with varying r-GO weight % at room temperature (RT) (b) with varying temperature of 0.4 wt % r-GO sample.

**Table 4.7.** Grain and grain boundary (or interface) resistance of NiO decked r-GO composites with varying r-GO wt %.

r-GO wt %	Grain boundary resistance $(R_{gb}) (10^6 \Omega \text{ cm})$	Grain resistance $(R_g) (10^4 \Omega \text{ cm})$
0.0	3.7	2.0
0.4	2.8	1.8
0.8	1.7	1.7
1.2	0.6	1.3
1.6	0.1	0.6
2.4	0.07	0.48
2.8	0.03	0.33

#### References

- [1] Jeong HK, Lee YP, Lahaye RJ, Park M, An KH, Kim IJ, Yang CW, Park CY, Ruoff RS, Lee YH. Evidence of graphitic AB stacking order of graphite oxides. J Am Chem Soc 2008;130(4):1362-6.
- [2] Titelman GI, Gelman V, Bron S, Khaflin RL, Cohen Y, Peled HB. Characteristics and microstructure of aqueous colloidal dispersions of graphite oxide. Carbon 2005;43(3):641-9.

- [3] Wakeland S, Martinez R, Gey JK, Luhrs CC. Production of graphene from graphite oxide using urea as expansion reduction agent. Carbon 2010;48(12):3463-70.
- [4] Jeong HK, Lee YP, Jin MH, Kim ES, Bae JJ, Lee YH. Thermal stability of graphite oxide. J Chem Phys Lett 2009;470(4):255-258.
- [5] Ju HM, Choi SH, Huh SH. X-ray diffraction patterns of thermally-reduced graphenes. J Korean Phy Soc 2010; 57(6):1649-52.
- [6] Cullity BD. Elements of X-ray Diffraction, The structure of polycrystalline aggregates. Addision Wesely.1978:259-263.
- [7] Akkari FC, Kanzari M, Rezig B. Preparation and characterization of obliquely deposited copper oxide thin films. Eur Phys J Appl Phys 2007;40(1):49-54.
- [8] Figueiredo V, Elangovan E, Goncalves G, Barqunha P, Pereira L, Franco N, Alves E, Martins R, Fortunato E. Effect of post-annealing on the properties of copper oxide thin films obtained from the oxidation of evaporated metallic copper. Appl Surf Sci 2008;254(13):3949-54.
- [9] Figueiredo V, Elangovan E, Goncalves G, Franco N, Alves E, Park SHK, Martins R, Fortunato E. Electrical, structural and optical characterization of copper oxide thin films as a function of post annealing temperature. Phy. Status Solidi A 2009;206(9):2143-8.
- [10] De Los Santos Valladares L, Hurtado Salinas D, Bustamante Dominguez A. Crystallization and electrical resistivity of Cu<sub>2</sub>O and CuO obtained by thermal oxidation of Cu thin films on SiO<sub>2</sub>/Si substrate. Thin Solid Films 2012;520(20):6368-67.
- [11] Wang H, Robinson JT, Diankov G, Dai H. Nanocrystal growth on graphene with various degrees of oxidation. J Am Chem Soc 2010;132(10):3270-1.
- [12] Ferrari AC, Robertson J. Interpretation of Raman spectra of disordered and amorphous carbon. Phys Rev B 2000;61(20):14095-107.
- [13] Ferrari AC, Robertson J. Resonant Raman spectroscopy of disordered, amorphous, and diamondlike carbon. Phys Rev B 2001;64(7):075414-27.
- [14] Tuinstra F, Koenig JL. Raman spectrum of graphite. J Chem Phys 1970;53(3):1126-1130.
- [15] Thomsen C, Reich S. Double Resonant Raman Scattering in Graphite. Phys Rev Lett 2000;85(24):5214-5217.
- [16] Cancado LG, Reina A, Kong J, Dresselhaus MS. Geometrical approach for the study of G' band in the Raman spectrum of monolayer graphene, bilayer graphene, and bulk graphite. Phys Rev B 2008;77(24):245408-245417.

- [17] Chrzanowski J, Irwin JC. Raman scattering from cupric oxide. Solid State Commu 1989;70(1):11-14.
- [18] Kourouklis GA, Jayaraman A, Batlogg B, Cava RJ, Stavola M, Krol DM, Rietman EA, Schneemeyer LF. Raman scattering in MBa<sub>2</sub>Cu<sub>3</sub>O<sub>7</sub> with M=Y, Eu, and Gd: effect of 18O substitution and oxygen vacancies on the Cu-O vibrational modes. Phys Rev B 1987;36(16): 8320-4.
- [19] Kuzmenko AB, Van der Marel D, Van Bentum PJM, Tishchenko EA, Presura C, Bush AA. Infrared spectroscopic study of CuO: Signatures of strong spin-phonon interaction and structural distortion. Phys Rev B 2001;63(9): 094303-15.
- [20] Zheng XG, Sakurai Y, Okayama Y, Yang TQ, Zhang LY, Yao X, Nonaka K, Xu CN. Dielectric measurement to probe electron ordering and electron-spin interaction. J Appl Phys 2002;92(5): 2703-8.
- [21] Punia R, Kundu RS, Meenakshi D, Murugavel S, Kishore N. Temperature and frequency dependent conductivity of bismuth zinc vanadate semiconducting glassy system. J Appl Phys 2012;112(8): 083701-5.
- [22] Banerjee S, Chakravorty D. Alternating current conductivity and dielectric dispersion in copper-silica nanocomposites synthesized by electrodeposition. J Appl Phys 1998;84(2):799-805.
- [23] Jiji K, Samuel MS, Anoop C, George KC. Correlated barrier hopping of CuO nanoparticles. J Semicond 2015;36(12):122003.
- [24] Zhou W, Zhu J, Cheng C, Liu J, Yang H, Cong C, Guan C, Jia X, Fan HJ, Yan Q, Li T, Yu CM. A general strategy toward graphene@metal oxide core-shell nanostructures for high-performance lithium storage. Energy Environ Sci 2011;4(12):4954-61.
- [25] Geng W, Zhao X, Zan W, Liu H, Yao Xi. Effects of the electric field on the properties of ZnO-graphene composites: a density functional theory study. Phys Chem Chem Phys 2014;16(8):3542-8.
- [26] Geng W, Zhao Xi, Liu H, Yao Xi. Influence of interface structure on the properties of ZnO/graphene composites: A theoretical study by density functional theory calculations. J Phys Chem C 2013;117(2):10536-44.
- [27] Kim H, Baek JT, Park HH. TA study of the electrical properties of graphene-incorporated direct-patternable ZnO thin films. Thin Solid Films 2013;529:234-7.
- [28] Lee JM, Pyun YB, Yi J, Choung JW, Park WI. ZnO Nanorod-graphene hybrid architectures for multifunctional conductors. J Phys Chem 2009;113(44):19134-8.

- [29] Shin KS, Jo H, Shin HJ, Choi WM, Choi JY, Kim SW. High quality graphene-semiconducting oxide heterostructure for inverted organic photovoltaics. J Mater Chem 2012;22(26):13032-8.
- [30] Zhang Q, Tian C, Wu A, Tan T, Sun L, Wang L, Fu H. A facile one-pot route for the controllable growth of small sized and well-dispersed ZnO particles on GO-derived graphene. J Mater Chem 2012;22(23):11778-84.
- [31] Hwang SW, Shin DH, Kim CO, Hong SH, Kim MC, Kim K, Lim KY, Kim S, Choi SH, Ahn KJ, Kim G, Sim SH, Hong BH. Plasmon-enhanced ultraviolet photoluminescence from hybrid structures of graphene/ZnO films. Phys Rev Lett 2010;105(12):127403-4.
- [32] Tian M, Ma Q, Li X, Zhang L, Nishi T, Ning N. High performance dielectric composites by latex compounding of graphene oxide-encapsulated carbon nanosphere hybrids with XNBR. J Mater Chem A 2014;2(29):11144-54.
- [33] Wu ZS, Zhou G, Yin LC, Ren W, Li F, Cheng HM. Graphene/metal oxide composite electrode materials for energy storage. Nano Energy 2012;1(1):107-131.
- [34] Yang LW, Wu XL, Huang GS, Qiu T, Yang YM. In situ synthesis of Mn-doped ZnO multileg nanostructures and Mn-related Raman vibration. J Appl Phys 2005;97(1):014308-4.
- [35] Yang LW, Han HL, Zhang YY, Zhong JX. Self-organized comb-like ZnO microstructures: Morphologies and defect induced optical emission. Opt Mater 2009;31(11):1640-4.
- [36] Fonoberov VA, Balandin AA. Interface and confined optical phonons in wurtzite nanocrystals. Phys Rev B 2004;70(23):233205-4.
- [37] Fonoberov VA, Balandin AA. Polar optical phonons in wurtzite spheroidal quantum dots: theory and application to ZnO and ZnO/MgZnO nanostructures. J Phys Cond Matter 2005;17:1085-97.
- [38] Han XH, Wang GZ, Jie JS, Choy WCH, Luo Y, Yuk TI, Hou JG. Controllable synthesis and optical properties of novel ZnO cone arrays via vapor transport at low temperature. J Phys Chem B 2005;109(7):2733-8.
- [39] Wei D, Liu Y, Zhang H, Huang L, Wu B, Chen J, Yu G. Scalable synthesis of few-layer graphene ribbons with controlled morphologies by a template method and their applications in nanoelectromechanical switches. J Am Chem Soc 2009;131(31):11147-11154.
- [40] Velayutham TS, Abd Majid WH, Gan WC, Khorsand Zak A, Gan SN. Theoretical and experimental approach on dielectric properties of ZnO nanoparticles and polyurethane/ZnO nanocomposites. J Appl Phys 2012;112(5):054106-10.

- [41] Singh G, Choudhary A, Haranath D, Joshi AG, Singh N, Singh S, Pasricha R. ZnO decorated luminescent graphene as a potential gas sensor at room temperature. Carbon 2012;50(2):385-394.
- [42] Kim P, Jones SC, Hotchkiss PJ, Haddock JN, Kippelen B, Marder SR, Perry JW. Phosphonic acid-modified barium titanate polymer nanocomposites with high permittivity and dielectric strength. Adv Mater 2007;19(7):1001-1005.
- [43] Gomez-Navarro C, Meyer JC, Sundaram RS, Chuvilin A, Kurasch S, Burghard M, Kern K, Kaiser U. Atomic structure of reduced graphene oxide. Nano Lett 2010;10:1144-1148.
- [44] Lankhorst MHR, Bouwmeester HJM, Verweij H. Thermodynamics and transport of ionic and electronic defects in crystalline oxides. J Am Ceram Soc 1997;80(9):2175-98.
- [45] Samuel MS, Chandran A, Koshy J, George KC. Correlated barrier hopping in ZnO nanorods. J Appl Phys 2011;109(11):113702-5.
- [46] Fattoum A, Gmati F, Bohli N, Arous M, Mohamed AB. Effects of the matrix molecular weight on conductivity and dielectric relaxation in plasticized polyaniline/polymethyl methacrylathe blends. J Phys D Appl Phys 2008;41:095407-9.
- [47] Soares BG, Leyva ME, Barra GMO, Khastgir D. Dielectric behavior of polyaniline synthesized by different techniques. Eur Polymer J 2006;42(3):676-686.
- [48] Liu LN, Wang CC, Lei CM, Li T, Wang GJ, Sun XH, Wang J, Huang SG, Li YD, H. Wang H. Relaxor- and phase-transition-like behaviors in ZnO single crystals at high temperatures. Appl Phys Lett 2013;102(11):112907-5.
- [49] Soulintzis A, Kontos G, Karahalious P, Psarras GC, Georga SN, Karontiras CA. Dielectric relaxation processes in epoxy resin-ZnO composites. J Poly Sci Part B: Polymer Phys 2009;47(4):445454.
- [50] Sendilkumar A, James Raju KC, Babu PD, Srinath S. Positive temperature coefficient of resistance of tetragonal Ti<sup>4+</sup> doped nano SrFeO<sub>3-δ</sub>. J Alloy Compd 2013;561(5):174-179.
- [51] Reeber, RR. Lattice parameters of ZnO from 4.2 to 296 °K, J Appl Phys 1970;41:5063-6.
- [52] Xu Y, Bai H, Lu G, Li C, Shi G. Flexible graphene films via the filtration of water-soluble noncovalent functionalized graphene sheets. J Am Chem Soc 2008;130(18):5856-5857.
- [53] Li D, Mueller MB, Gilje S, Kaner RB, Wallace GG. Processable aqueous dispersions of graphene nanosheets. Nature Nanotechnol 2008;3(2):101-5.

- [54] Dreyer DR, Jia HP, Bielawski CW. Graphene oxide: A convenient carbocatalyst for facilitating oxidation and hydration reactions. Angew Chem 2010;122(38):6965-6968.
- [55] Kim DJ. Lattice parameters, ionic conductivities, and solubility limits in fluorite-structure  $MO_2$  oxide  $[M = Hf^{4+}, Zr^{4+}, Ce^{4+}, Th^{4+}, U^{4+}]$  solid solutions. J Am Ceram Soc 1989;72(8):1415-1421.
- [56] Pietsch U, Unger K. The influence of free carriers on the equilibrium lattice parameter of semiconductor materials. Physica status solidi (a) 1983;80(1):165-172.
- [57] Gupta MK, Kumar B. High Tc ferroelectricity in V-doped ZnO nanorods. J Mater Chem 2011;21(38):14559-14562.
- [58] Onodera A, Tamaki N, Jini K, Yamashita H. Ferroelectric properties in piezoelectric semiconductor Zn<sub>1-x</sub> M<sub>x</sub> O (M= Li, Mg). Jpn J Appl Phys 1997;36(9B):6008-6011.
- [59] Gupta MK, Sinha N, Singh BK, Kumar B. Synthesis of K-doped p-type ZnO nanorods along (100) for ferroelectric and dielectric applications. Mater Lett 2010;64(16):1825-1828.
- [60] He JZ, Wang XX, Zhang YL, Cao MS. Small magnetic nanoparticles decorating reduced graphene oxides to tune electromagnetic attenuation capacity. J Mater Chem C 2016;DOI: 10.1039/C6TC02020H.
- [61] Scott JF. Ferroelectrics go bananas. J Phys Condens Matt 2008;20(2):021001.
- [62] Meikang H, Xiaowei Y, Luo K, Mian L, Wenyan D, Litong Z, Laifei C. Graphene-wrapped ZnO hollow spheres with enhanced electromagnetic wave absorption properties. J Mater Chem A 2014;2(39):16403-9.
- [63] Lu H, Lipatov A, Ryu S, Kim DJ, Lee H, Zhuravlev MY, Eom CB, Tsymbal EY, Sinitskii A, Gruverman A. Ferroelectric tunnel junctions with graphene electrodes. Nat Commun 2014;5:5518-7.
- [64] Hong X, Posadas A, Zou K, Ahn C, Zhu J. High-mobility few-layer graphene field effect transistors fabricated on epitaxial ferroelectric gate oxides. Phys Rev Lett 2009;102(13):136808-4.
- [65] Karim MR, Hatakeyama K, Matsui T, Takehira H, Taniguchi T, Koinuma M, Matsumoto Y, Akutagawa T, Nakamura T, Noro S, Yamada T, Kitagawa H, Hayami S. Graphene oxide nanosheet with proton conductivity. J Am Chem Soc 2013;135(22):8097-8100.
- [66] Jonscher AK. The 'universal' dielectric response. Nature 1977;267(5613):673-679.
- [67] Pei S, Cheng HM. The reduction of graphene oxide. Carbon 2012;50(9):3210-28.

- [68] Hutson AR. Piezoelectricity and conductivity in ZnO and CdS. Phys Rev Lett 1960;4(10):505-7.
- [69] Jung JH, Jeon JH, Sridhar V, Oh IK. Electro-active graphene-nafion actuators. Carbon 2011;49(4):1279-89.
- [70] Zarrin H, Higgins D, Jun Y, Chen Z, Fowler M. Functionalized graphene oxide nanocomposite membrane for low humidity and high temperature proton exchange membrane fuel cells. J Phys Chem C 2011;115(42):20774-81.
- [71] Lin YH, Li M, Nan CW, Le J. Grain and grain boundary effects in high- permittivity dielectric NiO-based ceramics. Appl Phys Lett 2006;89(1):032907-3.
- [72] Jose J, Khadar MA. Role of grain boundaries on the electrical conductivity of nanophase zinc oxide. Mater Sci Eng A 2001;304-306:810-3.
- [73] Yuan J, Song WL, Fang XY, Shi XL, Hou ZL, Cao MS. Tetra-needle zinc oxide/silica composites: High-temperature dielectric properties at X-band. Solid State Commun 2013;154:64-8.
- [74] Wang JJ, Fang XY, Feng GY, Song WL, Hou ZL, Jin HB, Yuan J, Cao MS. Scattering mechanisms and anomalous conductivity of heavily N-doped 3C-SiC in ultraviolet region. Phys Lett A 2010;374(22):2286-89.
- [75] Laube M, Schmid F, Pensl G, Wagner G, Linnarsson M, Maier M. Electrical activation of high concentrations of N<sup>+</sup> and P<sup>+</sup> ions implanted into 4H-SiC. J Appl Phys 2002;92(1):549-54.
- [76] Lunkenheimer P, Bobnar V, Pronin AV, Ritus AI, Volkov AA, Loidl A. Origin of apparent colossal dielectric constants. Phys Rev B 2002;66:052105-4.
- [77] Luo B, Wang X, Tian E, Gong H, Zhao Q, Shen Z, Xu Y, Xiao X, Li L. Dielectric enhancement in graphene/barium titanate nanocomposites. ACS Appl Mater Interfaces 2016;8(5):3340-8.
- [78] Huang X, Jiang P, Xie L. Ferroelectric polymer/silver nanocomposites with high dielectric constant and high thermal conductivity. Appl Phys Lett 2009;95:242901.
- [79] Jonscher AK, Dielectric Relaxation in Solids (Chelsea Dielectrics, London, 1983)
- [80] Havriliak S, Negami S. A complex plane analysis of α-dispersions in some polymer systems. J Polymer Sci Part C: Polymer Symposia 1966;14(1):99-117.
- [81] Schonhals A, Kremer F, Hofmann A, Fischer EW, and Schlosse E. Anomalies in the scaling of the dielectric α-relaxation. Phy Rev Lett 1993;70(22):3459-62.

- [82] Rahimabady M, Mirshekarloo MS, Yao K, Lu L. Dielectric behaviors and high energy storage density of nanocomposites with core-shell BaTiO<sub>3</sub>@TiO<sub>2</sub> in poly(vinylidene fluoride-hexafluoropropylene). Phys Chem Chem Phys 2013;15:16242-48.
- [83] Cole SC, Cole RH. Dispersion and absorption in dielectrics. J Chem Phys 1941;9:341-51
- [84] Davidson DW, Cole RH. Dielectric relaxation in glycerol, propylene glycol, and n-propanol. J Chem Phys 1951;19(12):1484-90
- [85] Tang Z, Zhang L, Feng W, Guo B, Liu F, Jia D. Rational design of graphene surface chemistry for high-performance rubber/graphene composites. Macromolecules 2014;47(24):8663-73
- [86] Vo TV, Anastasiadis SH, Giannelis EP. Dielectric study of poly(styrene-co-butadiene) composites with carbon black, silica, and nanoclay. Macromolecules 2011;44(15):6162-71
- [87] Dang Z, Wang L, Yin Y, Zhang Q, Lei Q. Giant dielectric permittivities in functionalized carbon-nanotube/electroactive-polymer nanocomposites. Adv Mater 2007;19(6):852-7
- [88] He F, Lau S, Chan HL, Fan J. High dielectric permittivity and low percolation threshold in nanocomposites based on poly(vinylidene fluoride) and exfoliated graphite nanoplates. Adv Mater 2009;21(6):710-5
- [89] Weber U, Greuel G, Boettger U, Weber S, Hennings D, Waser R. Dielectric Properties of Ba (Zr, Ti) O<sub>3</sub>-Based Ferroelectrics for Capacitor Applications. J Am Ceram Soc 2001;84(4):759-66.
- [90] Kim BG, Cho SM, Kim TY, Jang HM. Giant dielectric permittivity observed in Pb-based perovskite ferroelectrics. Phys Rev Lett 2001;86(15):3404-6.
- [91] Cross LE. Relaxor ferroelectrics. Ferroelectrics 1987;76(1):241-67.
- [92] Homes CC, Vogt T, Shapiro SM, Wakimoto S, Ramirez AP. Optical response of high-dielectric-constant perovskite-related oxide. Science 2001;293(5530):673-6.
- [93] Wu J, Nan CW, Lin Y, Deng Y. Giant dielectric permittivity observed in Li and Ti doped NiO. Phys Rev Lett 2002;89(21):217601-4.
- [94] Lin Y, Jiang L, Zhao R, Nan CW. High-permittivity core/shell stuctured NiO-based ceramics and their dielectric response mechanism. Phys Rev B 2005;72(1):014103-6.
- [95] Maensiri S, Thongbai P, Yamwong T. Giant dielectric response in (Li, Ti)-doped NiO ceramics synthesized by the polymerized complex method. Acta Mater 2007;55(8):2851-61.
- [96] Lin Y, Wang J, Jiang L, Chen Y, Nan CW. High permittivity Li and Al doped NiO ceramics. Appl Phys Lett 2004;85(23):5664-6.

- [97] Jana PK, Sarkar S, Chaudhuri BK. Low loss giant dielectric and electrical transport behavior of KxTiyNi1-x-yO system. Appl Phys Lett 2006;88(18):182901-3.
- [98] Thongbai P, Yamwong T, Maensiri S. The sintering temperature effects on the electrical and dielectric properties of Li {sub 0.05} Ti {sub 0.02} Ni {sub 0.93} O ceramics prepared by a direct thermal decomposition method. J Appl Phys 2008;104(7):074109-7.
- [99] Hsiao YJ, Chang YS, Fang TH, Chai YL, Chung CY, Chang YH. High dielectric permittivity of Li and Ta codoped NiO ceramics. J Phys D 2007;40(3):863-8.
- [100] Jana PK, Sarkar S, Sakata H, Watanabe T, Chaudhuri BK. Microstructure and dielectric properties of  $Na_xTi_yNi_{1-x-y}O$  (x=0.05–0.30, y = 0.02). J Phys D 2008;41(6):065403.
- [101] Shang J, Zhang Y, Yu L, Luan X, Shen B, Zhang Z, Lv F, Chu PK. Fabrication and enhanced dielectric properties of graphene–polyvinylidene fluoride functional hybrid films with a polyaniline interlayer. J Mater Chem A 2013;1(3):884-90.
- [102] Chu L, Xue Q, Sun J, Xia F, Xing W, Xia D, Dong M. Porous graphene sandwich/poly (vinylidene fluoride) composites with high dielectric properties. Compos Sci Technol 2013;86:70-5.
- [103] Wang D, Zhou T, Zha JW, Zhao J, Shi CY, Dang ZM. Functionalized graphene–BaTiO 3/ferroelectric polymer nanodielectric composites with high permittivity, low dielectric loss, and low percolation threshold. J Mater Chem A 2013;1(20):6162-8.
- [104] Sun J, Xue Q, Guo Q, Tao Y, Xing W. Excellent dielectric properties of polyvinylidene fluoride composites based on sandwich structured MnO<sub>2</sub>/graphene nanosheets/MnO<sub>2</sub>. Composites Part A: Applied Science and Manufacturing 2014;67:252-8.
- [105] Kohlmeyer RR, Javadi A, Pradhan B, Pilla S, Setyowati K, Chen J, Gong S. J Phys Chem C 2009;113(41):17626–9.
- [106] Yang C, Lin Y, Nan CW. Modified carbon nanotube composites with high dielectric constant, low dielectric loss and large energy density. Carbon 2009;47(4):1096-101.
- [107] Li M, Huang X, Wu C, Xu H, Jiang P, Tanaka T. Fabrication of two-dimensional hybrid sheets by decorating insulating PANI on reduced graphene oxide for polymer nanocomposites with low dielectric loss and high dielectric constant. J Mater Chem 2012;22(44):23477-84.
- [108] Akhtar AJ, Gupta A, Shaw BK, Saha SK. Unusual dielectric response in cobalt doped reduced graphene oxide. Appl phys Lett 2013;103(24):242902-5.

- [109] Baskey M, Maiti R, Saha SK, Chakravorty D. Superior magnetic, dielectric, and magnetodielectric effects in graphene/ZnCo<sub>2</sub>O<sub>4</sub> nanocomposites. J Appl Phys 2014;115(9):094306-7.
- [110] Fernandez-Garcia L, Suarez M, Menendez JL, Pecharroman C, Menendez R, Santamaría R. Dielectric behavior of ceramic-graphene composites around the percolation threshold. Nanoscale Res Lett 2015;10(1):216-7.
- [111] Yu PC, Lampert CM. In-situ spectroscopic studies of electrochromic hydrated nickel oxide films. Solar Energy Materials 1989;19(1-2):1-6.
- [112] Biju V, Khadar MA. Fourier transform infrared spectroscopy study of nanostructured nickel oxide. Spectrochimica Acta Part A: Molecular and Biomolecular Spectroscopy 2003;59(1):121-34.
- [113] Dietz RE, Parisot GI, Meixner AE. Infrared absorption and Raman scattering by two-magnon processes in NiO. Phys Rev B 1971;4(7):2302-2310.
- [114] Dang ZM, Nan CW, Xie D, Zhang YH, Tjong SC. Dielectric behavior and dependence of percolation threshold on the conductivity of fillers in polymer-semiconductor composites. Appl Phys Lett 2004;85(1):97-99.
- [115] Stankovich S, Dikin DA, Dommett GH, Kohlhaas KM, Zimney EJ, Stach EA, Piner RD, Nguyen ST, Ruoff RS. Graphene-based composite materials. Nature 2006;442(7100):282-6.
- [116] Mack JJ, Viculis LM, Ali A, Luoh R, Yang G, Hahn HT, Ko FK, Kaner RB. Graphite nanoplatelet reinforcement of electrospun polyacrylonitrile nanofibers. Adv Mater 2005;17(1):77-80.
- [117] Chen G, Weng W, Wu D, Wu C, Lu J, Wang P, Chen X. Preparation and characterization of graphite nanosheets from ultrasonic powdering technique. Carbon 2004;42(4):753-9.
- [118] Zheng G, Wu J, Wang W, Pan C. Characterizations of expanded graphite/polymer composites prepared by in situ polymerization. Carbon 2004;42(14):2839-47.
- [119] Kaczmarek H, Podgórski A. Photochemical and thermal behaviours of poly (vinyl alcohol)/graphite oxide composites. Polym Degrad Stab 2007;92(6):939-46.
- [120] Tan Y, Zhang J, Wu Y, Wang C, Koval V, Shi B, Ye H, McKinnon R, Viola G, Yan H. Unfolding grain size effects in barium titanate ferroelectric ceramics. Sci Rep 2015;5:9953.
- [121] C. W. Nan. Physics of inhomogeneous inorganic materials. Prog Mater Sci 1993;37(1):1-116.

- [122] Dang ZM, Lin YH, Nan CW. Novel ferroelectric polymer composites with high dielectric constants. Adv Mater 2003;15(19):1625-9.
- [123] Li YJ, Xu M, Feng JQ, Dang ZM. Dielectric behavior of a metal-polymer composite with low percolation threshold. Appl Phys Lett 2006;89(7):072902-3.
- [124] Balberg I. A comprehensive picture of the electrical phenomena in carbon black—polymer composites. Carbon 2002;40(2):139-43.
- [125] Song Y, Noh TW, Lee SI, Gaines JR. Experimental study of the three-dimensional ac conductivity and dielectric constant of a conductor-insulator composite near the percolation threshold. Phys Rev B 1986;33(2):904-8.

# **Chapter 5 Conclusions and Future Aspects**

This thesis work provided a comprehensive treatment on various dielectric behavioral aspects of metal oxide decorated r-GO nanocomposites namely CuO/r-GO, ZnO/r-GO, MgO/r-GO and NiO/r-GO nanocomposites synthesized by molecular level mixing technique. In this work, experimental results were fitted with suitable theoretical models that enabled the intricate examination and understanding of physical mechanisms that controlled the dielectric behavior of the above mentioned metal oxide decorated r-GO nanocomposites. All the metal oxide decorated r-GO nanocomposites synthesized in this thesis work exhibited enhanced dielectric constant values in comparison with the respective bare metal oxides.

In the case of CuO decked FLG [1], CuO nanoparticles (few nm in size) were uniformly decorated on the FLG sheets. Dielectric behaviour of the CuO decked FLG was found to be better than CuO. The possible mechanism involved in enhancing AC conductivity at high frequency was found to be arising from electron hopping which is confirmed by applying Quantum Mechanical Tunnelling (QMT).model on the experimental data. It was also found that the grain boundary contribution for conductivity in case of CuO decked graphene was found to be lower when compared with CuO.

In the case of ZnO decorated r-GO composites [2], ZnO nanoparticles were uniformly decorated on r-GO sheets similar to the case of CuO decked FLG. The enhanced dielectric permittivity of ZnO decorated r-GO composites in comparison to ZnO was attributed to the presence of functional groups and defects and to the heterogeneity of the composites, through which strong interfacial polarization (Maxwell–Wagner polarization) was observed. This was further confirmed by studying the temperature dependent dielectric behavior of ZnO decorated r-GO composites using the electric modulus formalism.

In order to further fine tune and understand any variation in polarization behavior of ZnO decorated r-GO composites [3], minuscule variations in synthesis conditions were introduced and a new set of ZnO decorated r-GO nanocomposites were synthesized. In this context it was shown that the presence of an appropriate number of polar functional groups (PFG) along with defects and a slightly distorted ZnO lattice (owing to changes in synthesis conditions) help in tuning the polarization behavior of ZnO decorated r-GO nanocomposites. In the new set of ZnO decorated r-GO composites, dielectric permittivity as high as 400 (which is 40 times greater than that of ZnO) could be achieved. The enhanced dielectric permittivity value was again found to be due to the strong interfacial polarization (Maxwell-

### **Conclusions and Future Scope**

Wagner polarization) as confirmed by electric modulus formalism studies. Further, it was found through a careful Rietveld refinement of X-ray diffraction data that ZnO in the ZnO decorated r-GO nanocomposites experienced a 'squeezing effect' which brought in structural changes. Functional groups attached to r-GO facilitated the 'squeezing effect' and thereby the structural changes, which were in-turn responsible for the unique polarization behavior of ZnO decorated r-GO composites. With increase in the r-GO content in these nanocomposites, maximum polarization increased owing to easy dipolar alignment, reorientation and stable polarization states. The observed polarization behavior was attributed to the lattice parameter disorder in ZnO combined with the presence of appropriate number of PFG in the nanocomposites. Moreover, a slight increase in r-GO content in the nanocomposites was found to increase the remnant polarization by one order of magnitude (i.e., from 0.062  $\mu$ C/cm<sup>2</sup> to 0.232  $\mu$ C/cm<sup>2</sup>) under the influence of an external electric field (~1.6 kV/cm). In all the nanocomposites ionic conductivity was measured in the order of  $10^{-2} \Omega^{-1} \text{cm}^{-1}$  and the calculated activation energies were consistent and supported the polarization behavior in the ZnO decorated r-GO nanocomposites. It was also shown that increasing r-GO concentration in the nanocomposites lead to the increasing the percentage of PFG due to which conductivity decreased while it followed Arrhenius behavior.

In the case of MgO decorated r-GO nanocomposites (with varying amounts of r-GO) [4], it was observed that dielectric permittivity values increased with r-GO content and temperature. At 1 kHz and room temperature one of the MgO decorated r-GO nanocomposites (with the maximum considered content of r-GO) exhibited a maximum dielectric permittivity value of 18, which increased to 612, at 473 K. The enhancement was attributed to Maxwell-Wagner or interfacial polarization. On the other hand, MgO decorated r-GO nanocomposites exhibited non-Debye relaxation, which was confirmed by applying Havriliak-Negami (HN) relaxation function on the experimental dielectric data. The enhancement in dielectric permittivity values has been attributed to the strong interfacial polarization as confirmed by the HN relaxation function fitting. Further, the excellent fitting of the dielectric dispersion curves with HN relaxation function clearly indicated that at lower frequencies (and at 473 K), the interfacial polarization is much stronger in comparison with the same at room temperature.

In the case of NiO decorated r-GO nanocomposites [5], dielectric permittivity values followed the typical percolation theory. The dielectric permittivity values increased with increasing r-GO wt % in the nanocomposites up to the percolation threshold (2.4 wt % of r-GO), where it reached the maximum value of 3688 at 1 kHz. It was also observed that the

### **Conclusions and Future Scope**

dielectric permittivity values increased with decreasing NiO grain size, also up to percolation threshold value. The percolation threshold was found to be consistent with universal threshold values. Further, Cole-Cole plot analysis revealed that the grain boundaries/interfaces in the nanocomposites are more active than NiO grains (with increasing r-GO wt % and temperature) due to the increased conductive networks in the nanocomposites.

For convenience, different dielectric characteristics of all the nanocomposites studied in this work are tabulated in **Table 5.1**.

Sample	Dielectric constant	Type of	Polarization
	At 1 k Hz	relaxation	
CuO/rGO	CuO-0.1G = 318	Debye	Orientational and
	CuO-0.2G = 667		interfacial
ZnO/rGO	ZnO-0.1G = 114		Orientational
	ZnO-0.2G = 153	Debye	
	ZnO-0.3G = 400		
MgO/rGO	MgO-0.05G = 358		Strong
	MgO-0.1G = 563		interfacial
	MgO-0.15G = 612	Non-Debye	

Debye

Follows percolation theory

NiO-2.4 wt % G = 3688

NiO-2.8 wt % G = 1548

NiO/rGO

**Table 5.1.** Dielectric characteristics of the nanocomposites studies in this work.

The immediate future scope of this thesis work is as follows: this work, especially molecular level mixing can be extended to other metal oxides decorated graphene nanocomposites in which metal oxides such as FeO, Fe<sub>2</sub>O<sub>3</sub>, MnO, CoO and Al<sub>2</sub>O<sub>3</sub> can be the constituents while varieties of graphenaceous constituents can also be used. These composites can be potential energy storage materials. As mentioned in section 2.2 chlorination of r-GO has enhanced the dielectric constant value [6]. Therefore the above-said graphenaceous constituents can be r-GO that has undergone addition of polar molecules owing to chemical treatments with chlorine, ammonia, sulfur dioxide, hydrogen sulfide etc. Due this addition, and inclusion of the treated r-GO in the composites, the composites' ability to storage energy is expected to be enhanced. Additionally, there is scope to examine and understand the optical properties especially band gap studies of these graphene/metal oxide composites. One of the promising applications of the graphene-oxide nanocomposites is chemical sensing which is useful for monitoring the toxicity, inflammability, and explosive nature of chemicals. The metal-oxides like ZnO, TiO<sub>2</sub> and CuO when combined with r-GO can be excellent materials for detecting trace amounts of hazardous gases and could work as active materials in chemical sensors.

### **Conclusions and Future Scope**

#### References

- [1] Jammula RK, Tumuluri A, Rotte NK, James Raju KC, Srikanth VVSS. Cupric oxide decked few-layered graphene: synthesis and dielectric behaviour. Carbon 2014;78:374-83.
- [2] Jammula RK, Pittala S, Srinath S, Srikanth VVSS. Strong interfacial polarization in ZnO decorated reduced-graphene oxide synthesized by molecular level mixing. Phys Chem Chem Phys 2015;17:17237 (DOI: 10.1039/c5cp02196k).
- [3] Jammula RK, Srikanth VVSS, Hazra BK, Srinath S. ZnO nanoparticles' decorated reduced-graphene oxide: Easy Synthesis, unique polarization behavior, and ionic conductivity. Mater Des 2016;110:311-6.
- [4] Jammula RK, Srikanth VVSS. Explication of dielectric behavior of MgO decorated reduced graphene oxide. (to be published, 2017)
- [5] Jammula RK, Srikanth VVSS. NiO decked reduced-graphene oxide composite: A giant dielectric permittivity and its percolation study. (to be published, 2017)
- [6] Kim JY, Lee WH, Suk JW, Potts JR, Chou H, Kholmanov IN, Piner RD, Lee J, Akinwande D, Ruoff RS. Chlorination of reduced graphene oxide enhances the dielectric constant of reduced graphene oxide/polymer composites. Adv Mater 2013;25(16):2308-13.